

UNDERSTANDING CREEP DEFORMATION BEHAVIOR OF 316LN STAINLESS STEEL AND ITS WELD JOINT USING IMPRESSION CREEP TECHNIQUE

By

NAVEENA

Enrollment No.: ENGG02200804029

Indira Gandhi Centre for Atomic Research, Kalpakkam

*A thesis submitted to the
Board of Studies in Engineering Sciences*

*In partial fulfillment of requirements
For the Degree of*

DOCTOR OF PHILOSOPHY

of

HOMI BHABHA NATIONAL INSTITUTE



November, 2013

HOMI BHABHA NATIONAL INSTITUTE

Recommendations of the Viva Voce Board

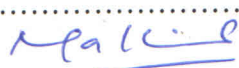
As members of the Viva Voce Board, we certify that we have read the dissertation prepared by Shri. Naveena entitled "Understanding Creep Deformation Behavior of 316LN Stainless Steel and Its Weld Joint Using Impression Creep Technique" and recommend that it may be accepted as fulfilling the dissertation requirement for the award of Degree of Doctor of Philosophy.

Chairman: Prof. A. K. Bhaduri



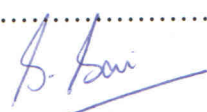
Date: 10/10/2014

Guide/Convener: Prof. M.D. Mathew



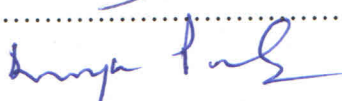
Date: 10/10/14

Member 1: Prof. Saroja Saibaba



Date: 10/10/2014

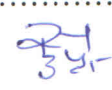
Member 2: Prof. B. K. Panigrahi



Date: 10/10/14

External Examiner: Prof. Subodh Kumar

Department of Materials Engineering
Indian Institute of Science, Bangalore



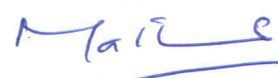
Date: 10/10/14

Final approval and acceptance of this dissertation is contingent upon the candidate's submission of the final copies of the dissertation to HBNI.

I/We hereby certify that I/we have read this thesis prepared under my/our direction and recommend that it may be accepted as fulfilling the dissertation requirement.

Date: 10.10.2014

Place: IGCAR, Kalpakkam



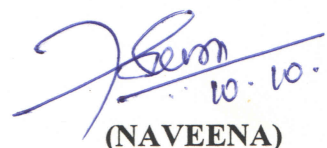
Prof. M.D. Mathew

(Guide)

STATEMENT BY AUTHOR


This dissertation has been submitted in partial fulfillment of requirements for an advanced degree at Homi Bhabha National Institute (HBNI) and is deposited in the Library to be made available to borrowers under rules of the HBNI.

Brief quotations from this dissertation are allowable without special permission, provided that accurate acknowledgement of source is made. Requests for permission for extended quotation from or reproduction of this manuscript in whole or in part may be granted by the Competent Authority of HBNI when in his or her judgment the proposed use of the material is in the interests of scholarship. In all other instances, however, permission must be obtained from the author.


10.10.2014.
(NAVEENA)

DECLARATION

I, hereby declare that the investigations presented in the thesis have been carried out by me. The work is original and has not been submitted earlier as a whole or in part for a degree/diploma at this or any other institution/University.


10.10.2014
(NAVEENA)

List of Publications arising from the Thesis

I. Peer Reviewed International Journals

1. **Naveena**, V. D. Vijayanand, V. Ganesan, K. Laha and M. D. Mathew, "Evaluation of The Effect of Nitrogen on Creep Properties of 316LN Stainless Steel from Impression Creep Tests", *Materials Science and Engineering A* 552 (2012) 112-118.
2. M.D. Mathew, **Naveena**, and D. Vijayanand, "Impression Creep Behavior of 316LN Stainless Steel", *Journal of Materials Engineering and Performance*, 22(2) (2013) 492-497.
3. **Naveena**, V.D. Vijayanand, V. Ganesan, K. Laha and M.D. Mathew, "Application of Impression Creep Technique for Development of Creep Resistant Austenitic Stainless Steel", *Procedia Engineering*, 55 (2013) 585-590.
4. **Naveena**, V.D. Vijayanand, K. Laha and M.D. Mathew, "Evaluation of Creep Deformation Behavior of Different Microstructural Zones of 316LN SS Weld Joint using Impression Creep Testing Technique", *Materials Science and Technology*, 30 (2014) 1223-1228.
5. **Naveena**, P. Parameswaran, K. Laha and M.D. Mathew, "Study on creep deformation mechanism of 316LN stainless steel from impression creep tests", *Materials at High Temperatures*, 31(2) (2014) 180-184.
6. **Naveena**, J. Ganesh Kumar and M.D. Mathew, "Finite element analysis of plastic deformation during impression creep", *Journal of Materials Engineering and Performance*, (2014) in print.
7. **Naveena**, Vani Shankar, P. Parameswaran and M.D. Mathew, "Impression creep deformation behavior of 316LN stainless steel", *Materials at High Temperatures*, (under review).
8. M.D. Mathew, **Naveena** and J. Ganesh Kumar, "Evaluation of tensile, creep and fracture toughness of materials using innovative small specimen testing methods" *Materials at High Temperatures* (under review)

II. Conference Proceedings

1. **Naveena** and M.D. Mathew, "Effect of Nitrogen on Creep Deformation Behavior of Type 316 LN Stainless Steel: Studies Using Impression Creep Technique",

- Proc. 12th International Conference on Creep and Fracture of Engineering Materials and Structures (CREEP 2012), Kyoto, **Japan**, May 25-31, 2012.
2. **Naveena** and M.D. Mathew, "Equivalence Between Impression Creep and Uniaxial Creep in 316LN SS", Proc. 49th National Metallurgists' Day (NMD) and the 65th Annual Technical Meeting (ATM) of the Indian Institute of Metals (IIM), Hyderabad, **India**, November 13-16, 2011.
 3. **Naveena**, V. D. Vijayanand, K. Laha and M. D. Mathew, "Impression Creep: An Innovative Testing Technique for Characterizing Creep Behavior of Weldments", Proc. the 5th National Symposium for Materials Research Scholars (MR-13), IIT Bombay, **India**, May 8-10, 2013.
 4. M.D. Mathew and **Naveena** "Understanding Creep Deformation Behavior of 316LN Stainless Steel from Impression Creep Tests", Proc. 16th International Conference on Strength of Materials, ICSMA-16, Bangalore, **India**, August 19-24, 2012.
 5. M.D. Mathew, K. Laha, J. Ganesh Kumar and **Naveena**, "Innovative Mechanical Testing Techniques for Evaluation of Creep Properties of Materials", Proc. International Conference & Exhibition on Pressure Vessels and Piping - OPE-2013, Mamallapuram, Tamil Nadu, **India**, February 13-16, 2013.

III. Report

1. Evaluation of Creep Deformation Behavior of 316LN Stainless Steel and Its Weld Joint using Impression Creep Technique, IGC Newsletter, Vol. 101 (2014) 22-26.

IV. Awards and Recognitions

1. "Young Researcher's Award" from **The Indian Institute of Metals**, Kalpakkam Chapter, for the year 2012, for the paper "Evaluation of The Effect of Nitrogen on Creep Properties of 316LN Stainless Steel from Impression Creep Tests" by **Naveena**, V. D. Vijayanand, V. Ganesan, K. Laha and M. D. Mathew, Materials Science and Engineering A 552 (2012) 112-118.
2. "Best Poster Paper award" in the 6th International Conference on Creep, Fatigue and Creep-Fatigue Interaction held during January 22-25, 2012 at Mamallapuram, Tamil Nadu, India, for the paper "Application of Impression Creep Technique for

Development of Creep Resistant Austenitic Stainless Steel” by **Naveena**, V. D. Vijayanand, V. Ganesan, K. Laha and M. D. Mathew.

3. Awarded "International Travel Support Fellowship" from Science and Engineering Research Board, **Department of Science and Technology** (DST), Govt. of India, to attend and present the research paper in the 12th International Conference on Creep and Fracture of Engineering Materials and Structures (CREEP 2012) held during May 25-31, 2012, in Kyoto, Japan.


10.10.2014.
(NAVEENA)

**I DEDICATE THIS WORK TO MY PARENTS
AND MY FAMILY**

ACKNOWLEDGEMENTS

First and foremost, I offer my sincere gratitude to my research supervisor, **Prof. M.D. Mathew**, Head, Mechanical Metallurgy Division, for his intellectual guidance and enthusiasm throughout my research work. I thank him for his keen interest, constructive suggestions and motivation throughout the course of investigation. I am deeply obliged to his constant support and help.

I am grateful to **Prof. A. K. Bhaduri**, Doctoral Committee Chairman, and Associate Director, Materials Development and Technology Group and, Doctoral committee members **Prof. Saroja Saibaba**, Head, Microscopy and Thermophysical Properties Division, Physical Metallurgy Group and **Prof. B. K. Panigrahi**, Head, Ion Beam and Computer Simulation Section, Materials Science Group, for their constructive suggestions and persistent support during the progress evaluation of my research work.

I express my sincere gratitude to **Dr. T. Jayakumar**, Dean, HBNI-IGCAR Campus and Director, Metallurgy and Materials group, for his support and encouragement. I thank **Dr. P.R. Vasudeva Rao**, Director, IGCAR, and **Shri. S.C. Chetal** and **Dr. Baldev Raj**, former Directors, IGCAR, for their kind support and permission to use all the facilities to carry out my research studies at Indira Gandhi Centre for Atomic Research.

I sincerely thank **Dr. M. Saibaba**, Associate Director, Resource Management Group, IGCAR, for providing comfortable accommodation and his kind support.

My sincere thanks are due to all my colleagues in Mechanical Metallurgy Division, Dr.K. Laha, Dr. R. Sandhya, Dr. B.K. Choudhary, Smt. K.S. Chandravathi, Shri. S. Ravi, Shri. M. Nandagopal, Ms. S. Latha, Shri. J. Ganesh Kumar, Shri. V.D. Vijayanand , Shri. T. Sakthivel, Shri. V.Ganesan, Shri. N.S. Thampi, Shri. S. Sakthi, Smt. J. Vanaja, Ms. S. Paneer Selvi, Dr. A. Nagesha, Shri. Sunil Goyal, Shri. G Varaprasad Reddy, Shri. R.

Prasad Rao Palaparti, Shri. Aritra Sarkar, Shri. K. Mariappan, Shri. D. Chellamuthu, Shri. M. Gandhi, Shri. M. Govindasamy, Shri. M. Srinivasa Rao, Smt. M. Esakkiammal, for their cooperation in many ways during this period. My special thanks are due to **Shri. V.D. Vijayanand** and **Shri. Ganesh Kumar** for their help in carrying out the experiments and finite element analysis, **Shri N. S. Thampi** for his technical support during the experimentation, and **Dr. Vani Shankar**, for EBSD analysis. I thank our collaborator **Dr. P. Parameswaran**, Physical Metallurgy Group, for TEM analysis. I also thank many in Materials Science Group for their kind help related to vacuum systems and TEM sample preparations. I would also like to thank **Shri. Vishweswaran**, RML, for useful discussions regarding finite element analysis. I also thank colleagues of Central Workshop Division for providing the facilities for specimen preparations.

I owe a debt of gratitude to my father and mother, my brother and sister, my family members, my uncles and aunts, grandmothers and grandfathers. They are my indispensable impetus to move forward. Nevertheless, I thank all my friends here for being with me for all the good. I also place on record my sincere gratitude to one and all who directly or indirectly have lent their helping hands in this venture.


10.10.14
(NAVEENA)

CONTENTS

SYNOPSIS	i
LIST OF FIGURES	xii
LIST OF TABLES	xxii

CHAPTER 1 Motivation, Objective and Scope of the Thesis **Page No.**

1.1	Introduction and Motivation	1
1.2	Creep and Its Standard Evaluation Procedures - An Overview	3
1.2.1	Creep Phenomenon	3
1.2.2	Creep Testing	3
1.2.3	Creep Curve	5
1.3	Structural Materials for Fast Breeder Reactors (FBRs)	6
1.4	Impression Creep- An Innovative Testing Technique for Characterizing Creep Behavior of Materials	8
1.4.1	Evolution of the Impression Creep Technique	8
1.4.2	Basic Aspects of the Impression Creep Test Technique	9
1.4.3	Advantages and Applications of the Impression Creep Technique	11
1.4.4	Limitations of the Impression Creep Technique	13
1.5	Objective and Scope of the Thesis	13
	References	15

CHAPTER 2 Literature Review

2.1	Introduction	16
2.2	Impression Creep Test Technique: The Genesis	16
2.2.1	Indentation Hardness	16
2.2.2	Relationship of Indentation Hardness with Other Material Properties	17
2.2.3	Indentation Test Method to Study Creep Behavior of Materials	18
2.3	Impression Creep Studies on Different Materials	19
2.3.1	Metals and Alloys	20
2.3.2	Weldments	27
2.3.3	Composites, Ceramics and Glasses	31
2.3.4	Polymers	34

2.4 Correlation between Impression Creep and Uniaxial Creep	35
2.5 Indenter Geometry and Dimensions	37
2.6 Plastic Zone in Impression Creep	38
2.7 Finite Element Analysis	40
References	42

CHAPTER 3 Experimental Details: Impression Creep Testing System, Materials and Characterization Techniques

3.1	Introduction	47
3.2	Impression Creep Testing System	47
	3.2.1 Vacuum Chamber	50
	3.2.2 Furnace	50
	3.2.3 Indenter- Specimen Cage	51
	3.2.4 Indenters	52
	3.2.5 Displacement Measurement System	53
	3.2.6 Loading Mechanism	53
	3.2.7 Vacuum System	54
	3.2.8 Control System	54
	3.2.9 Cooling System	55
	3.2.10 Data Acquisition System	55
3.3	Materials and Specimens	56
	3.3.1 316LN SS	56
	3.3.1.1 Specimen Preparation	57
	3.3.2 316LN SS Weld Joint	57
	3.3.2.1 Specimen Preparation	59
3.4	Materials Characterization– Before and After Impression Creep Tests	59
	3.4.1 Initial Microstructures of the 316LN SS and Its Weld Joints	59
	3.4.2 Characterization of the Plastic Zone in Impression Creep	60
	3.4.2.1 Microstructural Characterization	60
	3.4.2.1.1 Optical Microscopy	60
	3.4.2.1.2 Scanning Electron Microscopy	61
	3.4.2.1.3 Electron Back-Scattered Diffraction Analysis	61

3.4.2.1.4 Transmission Electron Microscopy	62
3.4.2.2 Microhardness	63
3.4.2.3 Optical Profilometry	64

CHAPTER 4 Impression Creep Behavior of 316LN Stainless Steel

4.1	Introduction	65
4.2	Equivalence between Impression Creep and Uniaxial Creep in 316LN SS	66
4.2.1	Analysis of Impression Creep Test Parameters	66
4.2.1.1	Punching Stress	66
4.2.1.2	Impression Velocity	66
4.2.2	Correlation between Impression Creep and Uniaxial Creep Test Parameters	67
4.2.3	Impression Creep Tests	68
4.2.4	Microstructure of the Alloy Prior to Impression Creep Testing	69
4.2.5	Impression Creep Curves	70
4.2.6	Stress Dependence of the Steady State Impression Velocity	72
4.2.7	Comparison of Impression and Uniaxial Creep Data	73
4.2.8	Evaluation of the Apparent Activation Energy for Creep Deformation from Impression Creep Technique	74
4.2.8.1	Impression Creep Tests	74
4.2.8.2	Impression Creep Curves	75
4.2.8.3	Analysis of Activation Energy for Creep in 316LN SS	76
4.3	Evaluation of the Effect of Nitrogen on Creep Behavior of 316LN SS	81
4.3.1	Initial Microstructure of the Alloys	82
4.3.2	Impression Creep Curves	83
4.3.3	Effect of Punching Stress on Impression Velocity	85
4.3.4	Influence of Nitrogen Content on Impression Velocity	87
4.4	Analysis of the Plastic Zone in Impression Creep Test	88
4.4.1	Microstructural Characterization	89
4.4.2	Microhardness Studies	100
4.4.3	Surface Profilometry Studies	110
4.4.3.1	Material Pile-up	110
4.4.3.2	Spacing between the Adjacent Indentations	112

4.5 Conclusions	113
References	114

CHAPTER 5 Application of Impression Creep Technique to Study Creep Behavior of Different Microstructural Zones of 316LN SS Weld Joint

5.1	Introduction	117
5.2	316LN SS Weld Joint	118
5.3	Identifying the Test Locations in Different Zones of the Weld Joint	119
5.4	Microstructure of Different Zones of the Weld Joint before Impression Creep Testing	120
5.5	Microhardness of Different Zones of the Weld Joint before Impression Creep Testing	122
5.6	Impression Creep Tests	123
5.7	Impression Creep Behavior of Different Microstructural Zones	123
5.8	Comparison of Impression and Uniaxial Creep Data	128
5.9	Microstructural Evolution in Different Zones	129
5.10	Conclusions	137
	References	138

CHAPTER 6 Finite Element Analysis of Impression Creep Deformation Behavior of 316LN SS

6.1	Introduction	139
6.2	Finite Element Analysis of Impression Creep Deformation	139
6.2.1	Axisymmetric Model of Impression Creep Test	140
6.2.2	Finite Element Model Description	141
6.2.2.1	FE Model and Meshing	141
6.2.2.2	Material Properties	143
6.2.2.2.1	Elastic Property	143
6.2.2.2.2	Plastic Property	143
6.2.2.2.3	Creep Property	143

6.2.2.3 Analysis Steps, Boundary Conditions, Loading and Simulations	144
6.3 FEA Results and Discussion	145
6.3.1 Optimization of the Mesh Size	145
6.3.2 Validation of FE Model through Contact Stress Analysis	148
6.3.3 Von Mises Stress Distribution in the Specimen beneath the Indentation	151
6.3.3.1 Evolution of the Von Mises Stress during Loading	152
6.3.3.2 Evolution of the Von Mises Stress during Creep	156
6.3.4 Material Pile-up Mechanism in Impression Creep	161
6.4 Conclusions	171
References	173

CHAPTER 7 Summary and Future Directions

7.1 Summary of the Thesis	175
7.2 Future Directions	179

SYNOPSIS

The development of high temperature engineering alloys for various components of fast breeder reactor (FBRs) is a unique challenge as these materials have to possess a combination of properties such as superior creep strength, low cycle fatigue properties, creep-fatigue interaction properties, corrosion resistance, adequate weldability, compatibility with liquid sodium and microstructural stability. Requirement of these stringent material properties arises from the fact that these components have to withstand hostile environments in the reactor, during its service, such as intense neutron flux of about 10^{15} n/cm²s⁻¹, liquid sodium coolant and high temperature of operation. Nitrogen-alloyed low carbon grade type 316L(N) stainless steel (SS) is an advanced version of austenitic stainless steel. 316L(N) SS containing 0.02-0.03 wt.% carbon and 0.06-0.08 wt.% nitrogen has been employed as a primary structural material for out-of-core components such as main vessel, inner vessel and sodium pipe lines in India's Prototype Fast Breeder Reactor (PFBR). The desired properties for these structural materials are derived through a systematic, microstructurally based programme of alloy development which primarily involves optimization of chemical compositions in the alloy. Therefore, the alloy development programme becomes sufficiently broad to encompass all the above mentioned properties and characteristics. Further, during the initial stages of alloy development, which are aimed to optimize chemical composition, only limited quantity of the material are available. Therefore, it is important to make effective use of limited volume of material available for testing.

Components are made by welding. Welds are the weak links of the components. The life of structural components operating at temperatures greater than 670 K is often limited by the creep damage of structural materials and their weld joints. Further, these components are designed to operate for a long time of about 40 years. Therefore,

detailed understanding of the creep deformation behavior of both parent materials and their weld joints becomes one of the major objectives of the alloy development programme which necessitates a large number of creep tests to be carried out at various stress levels and temperatures in order to understand the properties of the material and generate a large data base for design and validation.

Conventional uniaxial creep testing is the most commonly used test method for characterization of creep properties of materials. Creep testing requires a considerable volume of material for specimen preparation and necessitates many such specimens to carryout creep tests at different temperatures and stress levels in order to generate a reasonable data base. In addition, each creep test takes long duration. Hence, the test methodology is both time and material consuming. In view of this, to assist in the design and development of new engineering alloys, it is vital to establish a robust and reliable mechanical testing method that can accurately determine mechanical properties at both ambient and high temperatures using small sized specimens. Impression creep testing [1] is one such innovative miniature testing technique that can be used to study the creep deformation behaviour of materials.

In the present investigation, a unique impression creep testing facility has been established at Indira Gandhi Centre for Atomic Research (IGCAR). A systematic study of creep deformation behavior of 316LN SS and its weld joint using this technique has been carried out. Effect of nitrogen content on creep behavior of 316LN SS has been studied using this technique. Impression creep technique has been employed to characterize creep behavior of the heat-affected zone, the weld metal and the base metal of 316LN SS weld joint. Emphasis has been given to study and understand the material mechanics involved in impression creep process by experimental investigations and finite element simulation studies. The thesis demonstrates the applicability of

impression creep technique for the alloy development activity and its suitability to characterize creep deformation behavior of narrow microstructural regions, namely, the heat-affected zone, the base metal and the weld metal in weld joints.

Organization of the Chapters in the Thesis

The thesis comprises of 7 chapters. An outline of the individual chapter is presented below.

Chapter 1

Motivation, Objective and Scope of the Thesis

This chapter outlines the motivation for the present research work at Indira Gandhi Centre for Atomic Research, Kalpakkam, India. The chapter discusses various structural materials used in FBR components, emphasizing the need to continuously improve the mechanical properties of these materials, challenges involved from the materials development perspective and the importance of small specimen testing techniques for mechanical properties evaluation. The chapter gives an overview of the creep phenomenon, its standard evaluation procedures and general characteristics of creep curve. Chapter gives an introduction to the impression creep technique and illustrates the test methodology, and discusses its potential advantages, applications in other research and development areas, and its limitations. This chapter also discusses scope of the thesis.

Chapter 2

Literature Review

Chapter 2 contains exhaustive survey on the impression creep testing technique employed by several researchers worldwide for characterizing creep behavior of a wide range of materials. The fundamental aspects relevant to the present thesis interest are covered in this chapter. The chapter critically examines the correlation between the

impression creep test and the conventional uniaxial creep test parameters in various materials.

Chapter 3

Experimental Details: Impression Creep Testing System, Materials and Characterization Methods

This chapter describes development of the impression creep testing system at IGCAR and the system details. The chapter includes details of the materials and their chemical compositions used in the present investigation i.e., 316LN SS containing different nitrogen content and 316LN SS weld joint. The specimen preparation techniques employed in the present investigation for the impression creep test specimens are detailed. The method devised for identifying the exact location for impression creep test in the heat-affected zone of weld joint is explained. The dimension of the specimen used in the investigation was 20 mm x 20 mm x 10 mm. In the present study, cylindrical indenters with flat-end, made of tungsten carbide, were used. The diameter of the indenter was 1 mm. Chapter also discusses the characterization techniques employed and experimental procedure to analyze microstructural properties of the material investigated and to study the deformation associated with impression creep in the specimen. The characterization techniques include optical microscope, scanning electron microscope, transmission electron microscope, microhardness, optical profilometer employed. The specimen preparation techniques for these investigations are discussed.

Chapter 4

Impression Creep Behavior of 316LN Stainless Steel

Chapter 4 describes the extensive studies carried out on the creep behavior of 316LN SS using the impression creep testing system. These studies and results are briefed below.

Equivalence between Impression Creep and Uniaxial Creep in 316LN SS

With a aim to establish the technique, a systematic study of creep behavior of 316LN SS using this technique has been undertaken. To this end, impression creep experiments were carried out on 316LN SS containing 0.14 wt. % nitrogen, under different stress levels ranging from 472 to 760 MPa, at various temperatures in the range of 898 to 973 K. All the experiments were conducted in the vacuum of 10^{-6} mbar. The depth of penetration of the indenter was plotted as a function of test time at a constant temperature of 923 K for different stress levels and at a constant punching stress of 675 MPa for different temperatures. Impression creep curves exhibited two characteristic creep stages, namely, a primary creep stage after an initial loading strain and a secondary creep stage. However, the tertiary creep stage that appears in conventional creep curves was found to be absent here. Chapter discusses the analysis of impression creep parameters and its correlation with the conventional uniaxial creep parameters. Equivalence between the punching stress and steady state impression velocity with uniaxial stress and steady state creep rate respectively has been established based on the laws of mechanics for time dependent plasticity. The Norton power law relationship between the steady state impression velocity and punching stress was found to be obeyed. Temperature dependence of steady state impression velocity obeyed Arrhenius-type rate equation. The stress exponent value of 6.4 [2] determined from impression creep technique was found to be in close agreement with

the stress exponent value of 6.9 determined from conventional uniaxial creep tests [3]. The activation energy for creep was 504 kJmol^{-1} . The results in this investigation are in close agreement with the activation energy value determined by Morris et al. [4] for type 316 SS ($480\text{-}500 \text{ kJmol}^{-1}$), Mathew et al. [5] for 316LN SS (585 kJmol^{-1}) in the temperature range of 873-923 K and Park et al. [6] for type 316 SS (395 kJmol^{-1}).

Evaluation of the Effect of Nitrogen on Creep Behaviour of 316LN SS

One of the potential applications of impression creep technique is in alloy development. The influence of nitrogen on the creep behavior of 316LN SS was studied from this technique [7]. Impression creep tests were conducted on the 316LN SS containing 0.07, 0.11, 0.14 and 0.22 wt. % nitrogen at 923 K, under punching stress levels of 472, 591, 675 and 760 MPa. Steady state impression velocity was found to increase with increasing punching stress. A power law relationship between steady state impression velocity and punching stress was found to be obeyed in all the four heats. The power law exponent (n) varied between 3.3 and 8.2 depending upon the nitrogen content in the heat. Similar observations were found in the case of conventional uniaxial creep tests carried out on these materials [8]. It was observed that the steady state impression velocity decreased with increasing nitrogen content at all the four stress levels. This result is in good agreement with the results obtained from conventional uniaxial creep tests which showed a decrease in steady state creep rate with increasing nitrogen content [8]. The beneficial effect of nitrogen on the creep behavior of 316LN SS is discussed in the chapter.

Characteristics of the Plastic Deformation Zone in Impression Creep

Detailed investigations on the characteristics of the plastic zone in the impression creep have been carried out. The study of shape and size of the plastic zone, the extent of deformation and the microstructural evolution in the vicinity of the impression were

carried out by optical microscopy, scanning electron microscopy, EBSD analysis, TEM analysis, microhardness and surface profilometry. These results are discussed in this chapter.

Chapter 5

Application of Impression Creep Technique to Study Creep Behavior of Different Microstructural Zones of 316LN SS Weld Joint

Chapter 5 discusses the investigation carried out on the creep deformation behavior of narrow microstructural regions, namely, the heat affected zone, the weld metal, and the base metal of a high nitrogen grade of 316LN SS weld joint using impression creep technique. Characterizing creep behavior of narrow microstructural zones of weld joints is another domain where impression creep testing owes its credentials over the conventional creep testing. 316LN SS weld pad was prepared by employing manual metal arc welding process. Thickness of the weld pad was about 23 mm. Rectangular blocks of 15 mm thick cross weld joints were cut from the weld pad and the cross-sectional surface of the rectangular blocks were polished up to 1 μm finish using standard metallographic techniques. The analysis of substantial variation in microstructure and morphology of the weld metal, the heat-affected zone and the base metal regions in the weld joint was carried out before creep testing. Impression creep tests were carried out at 923 K on three distinct microstructural regions, namely, the weld metal, the heat-affected zone and the base metal of a 316LN SS weld joint, under the punching stress levels of 675 MPa and 760 MPa. The impression creep curves of all the three different microstructural zones showed a trend characterized by an initial loading strain followed by a primary creep stage and a distinct steady state creep stage. The tertiary creep stage which we generally observe in uniaxial creep curves was not exhibited. The weld metal, the base metal and the heat-affected zone exhibited distinct

creep behavior. Weld metal region showed a higher steady state impression velocity than the base metal and the heat-affected zone which indicates its lower creep strength. The heat-affected zones were found to have the lowest steady state impression velocity. The difference in creep behavior of each zone was correlated with the difference in microstructure and morphology of different zone of the weld joint. The creep behavior of the weld metal, the base metal and the heat-affected zone, characterized from impression creep tests in our investigation, was found to be consistent with the creep behavior of the weld metal, the base metal and the heat-affected zone of AISI 316 steel weld joints characterized from uniaxial creep tests by Etienne et al. [9] In order to corroborate the validity of the impression creep technique, a comparison was made between the data obtained from impression creep tests and from independent uniaxial creep tests on the weld metal and the base metal. A good correlation was established between impression creep and uniaxial creep results. Microstructural evolution in the plastic zone in the vicinity of the impression in each zone was analyzed.

Chapter 6

Finite Element Analysis of Impression Creep Deformation in 316LN Stainless Steel

Chapter 6 details the Finite Element Analysis (FEA) of impression creep deformation in 316LN SS. An axisymmetric Finite Element Model of indenter-specimen system has been developed using commercial ABAQUS finite element analysis software. The specimen was modeled as elastic-plastic-creep deformable body. The Norton power-law constitutive equation was used as a flow rule for the creep deformation of each element in the model. Impression creep tests were simulated to understand the stress-strain field and material flow behavior during impression creep process. Detailed analyses of the Von Mises stress distribution under the punch and its variation during

creep deformation has been carried out. Chapter discusses the size and shape of the resulting plastic zone. Chapter also discusses the mechanics involved in impression creep process concerning the material flow behavior in response to the indentation and mechanism of material pile-up on the specimen surface.

Chapter 7

Summary, Conclusions and Future Directions

Chapter 7 discusses the salient conclusions and the summary of the results of impression creep studies on 316LN SS and its weld joint. Chapter also summarizes the extensive studies carried out on understanding the plastic zone, the mechanics involved in impression creep process, the material pile-up behavior analyzed using various characterization techniques and numerical simulation. This chapter also includes the scope for future work. A brief summary of the work is given below.

- Impression creep testing facility has been established at Indira Gandhi Centre for Atomic Research. Impression creep technique was successfully employed to characterize the creep behavior of 316LN SS and its weld joint.
- Equivalence between impression creep test results and uniaxial creep test results for 316LN SS and its weld joint have been established.
- Stress dependence of creep deformation in 316LN stainless steel was investigated. A power law relationship was found to obey between the steady state impression velocity and the punching stress in all the four heats. The temperature dependence of creep deformation in 316LN stainless steel was investigated and the activation energy for creep was determined using impression creep technique.
- The effect of nitrogen on the creep deformation behavior of 316LN SS was investigated by employing impression creep technique as a faster and non-

invasive method. The steady state impression velocity was found to decrease with increase in nitrogen content. Impression creep testing technique was found to be sensitive to capture the small variation in creep rate due to the small change in composition.

- Impression creep technique was employed to characterize creep behavior of distinct microstructural regions such as the weld metal, the heat-affected zone and the base metal in a high nitrogen grade of 316LN SS weld joint.
- Finite Element Analysis of impression creep deformation was carried out to understand the elastic-plastic-creep deformation which occurs in the specimen in response to the indentation process.
- A good correspondence between the impression creep test and the conventional creep test results on engineering alloys demonstrates that impression creep could be used to characterize the creep behavior of materials. It can be concluded that the impression creep technique is capable of yielding much of the information that can be obtained from conventional uniaxial creep testing and the technique is very attractive in alloy development where the material available for testing is small and a rapid screening of several heats are essential.

REFERENCES

- [1] J. C. M. Li and S. N. Chu, J. Mater. Sci., 1977, 12, p 2200-2208.
- [2] Naveena and M.D. Mathew, in: K. Maruyama (Ed.), Proceedings of the 12th International Conference on Creep and Fracture of Engineering Materials and Structures, The Japan Institute of Metals, Kyoto, Japan, 2012, No. B18.
- [3] M.D.Mathew, K. Laha and V. Ganesan, Mater. Sci. Eng. A535 (2012) 76-83.
- [4] Morris. D. G. and D. R. Harries, Met. Sci. 12(1978) 525.
- [5] M.D.Mathew, G.Sasikala, Bhanu Sankara Rao and S.L.Mannan, Mater. Sci. Eng. A 148 (1991) 253.
- [6] J. G. Park and D.Y. Lee, Scr. Met. 29 (1993) 595.
- [7] Naveena, V.D. Vijayanand, V. Ganesan, K. Laha and M.D. Mathew, Mater. Sci. Eng. A 552 (2012) 112-118.
- [8] M.D.Mathew, K. Laha and V. Ganesan, Mater. Sci. Eng. A535 (2012) 76-83.
- [9] C. F. Etienne, O. Rossum, and F. Roode: "Creep of welded joints AISI 316" Proc. Int. Conf. on "Engineering Aspects of Creep" 1980, Vol. 2, 113-121.

LIST OF FIGURES

Figure No.	Title	Page No.
1.1	A schematic of the tensile creep test specimen (dimensions are in mm).	4
1.2	An illustration of the tensile creep testing.	4
1.3	Schematic of the tensile creep testing system.	5
1.4	Schematic of tensile creep curve showing three different creep stages.	6
1.5	A schematic of the impression creep test specimen (dimensions are in mm).	10
1.6	Schematic illustration of the impression creep testing.	10
1.7	Schematic of the impression creep curve.	11
2.1	Typical impression creep curves for succinonitrile crystals [21]	19
2.2	Typical impression creep curves for α -Tin single crystals after Chu and Li [22, 23].	20
2.3	Stress dependence of a) steady state impression velocity and b) steady state creep rate (tensile creep tests), showing close agreement in stress exponent values obtained from both the test techniques in Cd metal [24].	22
2.4	Correlation between tensile creep and impression creep test results on Cd metal for a stress conversion factor of 4 ($\alpha = 1/4 = 0.25$); solid lines-tensile creep; data points-impression creep [24].	23
2.5	Correlation between tensile creep and impression creep parameters in magnesium for a stress conversion factor $\alpha = 1/3 \approx 0.33$ [25].	24
2.6	Impression velocity vs. distance from the fusion line for 2.25Cr-1Mo steel to type 316 SS weldment joined with type 310 SS filler material. [32].	27
2.7	Rectangular indenter-specimen assembly employed by Hyde and Co-workers for impression creep testing of HAZ material in a P91 weld tested at 923 K; The width d of the indenter was 1 mm [35, 36].	29
2.8	Impression creep curves a) for HAZ material in a P91 weld tested at 923 K, under different stress levels and b) for three different ex-service 1/2CrMoV	29

steam pipe samples tested at 913 K at 90 MPa [35].

2.9	Impression creep curves for HAZ material of CrMoV weldment tested under different stress levels [37].	30
2.10	a) Impression creep curves for the composite tested at 448 K and 100 MPa in the transverse direction b) the strain rate vs. strain curves corresponding to (a), c) a reverse creep behavior, i.e., strain rate decreasing with strain, tested at 573 K and 120 MPa, and d) the strain rate vs. strain curves corresponding to (c) [41].	32
2.11	Displacement vs time plots obtained for soda-lime-silica glass using cylindrical flat punch a) influence of temperature and b) influence of load [45].	34
2.12	Optical micrograph of the deformation region observed by Butt et al. [70] in Sic particle-MoSi ₂ composite specimen.	39
2.13	Scanning Electron Micrograph showing deformation under the punch in TiAl alloy reported by Dorner et al. [57].	40
3.1	Impression creep testing facility established at IGCAR.	48
3.2	Schematic diagram showing different parts of the impression creep testing machine.	49
3.3	Furnace inside the vacuum chamber.	51
3.4	A view of the specimen cage situated inside the furnace.	52
3.5	Tungsten carbide indenters of different diameters.	52
3.6	The LVDT set up for displacement/depth measurement.	53
3.7	Vacuum system incorporated with the impression creep testing system.	54
3.8	Impression creep machine control unit.	55
3.9	Typical impression creep test specimen employed in the present investigation.	57
3.10	The cross section of the 316LN SS weld joint on which impression creep tests were conducted.	59
3.11	Schematic illustration of sectioning of the tested specimen for cross-sectional	60

microstrutural analysis (for optical, SEM and EBSD).

3.12	Schematic diagram showing a) sectioning of the impression creep tested specimen and b) region from which a rectangular section was cut for TEM specimen.	62
3.13	Schematic diagram illustrating the microhardness measurements made around the impressions on the sectioned surface of the specimen.	64
4.1	Microstructure of solution annealed 316LN SS containing 0.14 wt. % nitrogen.	69
4.2	Plot of impression depth versus time for 316LN SS containing 0.14 wt. % nitrogen at various stress levels.	71
4.3	Image of typical impression on the surface of the specimen.	71
4.4	Variation of impression velocity with time for various stress levels indicating the steady state for 316LN SS containing 0.14 wt. % nitrogen.	72
4.5	Norton power law relationship between steady state impression velocity and punching stress for 316LN SS containing 0.14 wt. % nitrogen.	73
4.6	Correlation between impression creep and conventional uniaxial creep data for 316LN SS at 923 K.	74
4.7	Typical impression creep curves at various temperatures at a constant punching stress of 675 MPa for 316LN SS containing 0.14 wt. % nitrogen.	75
4.8	Temperature dependence of impression velocity in 316LN SS containing 0.14 wt. % nitrogen at 675 MPa.	76
4.9	Arrhenius type relationship between the steady state impression velocity and the temperature.	77
4.10	Temperature dependence of the equivalent steady state creep rate for 316LN SS.	78
4.11	The variation of temperature-compensated steady state impression velocity with the modulus-compensated punching stress (log-log scale) for 316LN SS (the steady state impression velocity normalized to the diameter D of the punch represents the uniaxial steady state strain rate). The constitutive equation given in Eqn.4.10 satisfactorily correlates for the impression creep test data for 316LN SS.	81

4.12	Microstructure of solution annealed 316LN SS containing (a) 0.07, (b) 0.11, (c) 0.14 and (d) 0.22 wt. % nitrogen.	82
4.13	Plot of impression depth versus time for 316LN SS containing 0.07 wt. % nitrogen at various stress levels.	83
4.14	Plot of impression depth versus time for 316LN SS containing 0.11 wt. % nitrogen at various stress levels.	84
4.15	Plot of impression depth versus time for 316LN SS containing 0.22 wt. % nitrogen at various stress levels.	84
4.16	Variation of steady state impression velocity with punching stress for different nitrogen content.	85
4.17	Plot of equivalent steady state creep rates and uniaxial tensile stresses derived from steady state impression velocities and punching stresses using Eqns. (4.5) and (4.6) for various nitrogen levels.	86
4.18	Variation of steady state impression velocity with nitrogen content in 316LN SS for various stress levels.	88
4.19	(a) and (b) Optical micrographs showing the typical deformation in the impression creep tested specimen.	90
4.20	(a) and (b) SEM micrographs showing the material flow pattern near the edge of the indentation in 316LN SS containing 0.14 wt. % nitrogen after the impression creep test.	91
4.21	(a) and (b) Optical micrographs showing the deformation in the impression creep tested specimen in 316LN SS containing 0.14 wt. % nitrogen tested at 948 K, under the punching stress of 675 MPa.	93
4.22	Optical micrographs of impression creep regions in 316LN SS containing 0.14 wt. % nitrogen depicting three distinct regions in the vicinity of the impression. The deformed plastic zone was found to be hemispherical.	94

4.23	Optical micrographs of impression creep regions in 316LN SS containing 0.14 wt. % nitrogen depicting three distinct regions in the vicinity of the impression. The deformed plastic zone was found to be hemispherical.	95
4.24	(a) and (b) Optical micrographs at a higher magnification showing the region 1 just beneath the indentation. No significant change in the shape of grains in this region.	96
4.25	Right corner of the impression showing extensive deformation in region 2 and no significant grain shape change away from the indentation in the radial direction.	96
4.26	Comparison of inverse pole figure (IPF) maps of 316LN SS in the (a) undeformed which is away from the indentation and (b) deformed regions below the indentation.	98
4.27	Optical micrographs showing the deformation under the punch and the line indicating the region from which TEM specimen was taken.	99
4.28	TEM micrograph showing dislocation structure in region 2, which are well dispersed.	99
4.29	Optical micrographs of impression creep regions in 316LN SS containing 0.22 wt. % nitrogen over which microhardness measurements were made: (a) 760MPa, (b) 675 MPa, (c) 591 MPa.	101
4.30	Optical micrograph showing the microhardness profiles measured along different lines around the impressions.	102
4.31	Microhardness profile on the cross sectional surface along the line UV showing that there is no overlapping of the deformed zone of adjacent impressions.	103
4.32	Microhardness in the region far away from the impressions. The average hardness in this region was 206 VHN.	103
4.33	Microhardness profile on the cross sectional surface along the line AB.	104
4.34	Microhardness profile on the cross sectional surface along the line CD and EF	105

4.35	Microhardness profile on the cross sectional surface along the line GH (horizontal line along 1.5 mm distance from indentation corresponding to 760 MPa).	106
4.36	Microhardness profile on the cross sectional surface along the line WX (line along 0.25 mm distance) between the two impressions corresponding to 760 MPa 591 MPa.	107
4.37	Microhardness profile on the cross sectional surface along the line IJ in the loading direction in the vicinity of the impression at 591 MPa.	108
4.38	Microhardness profile on the cross sectional surface along the line KL and MN in the vicinity of the impression at 591 MPa.	108
4.39	Microhardness profile on the cross sectional surface along the line OP in the loading direction in the vicinity of the impression at 675 MPa.	109
4.40	Microhardness profile on the cross sectional surface along the line QR and ST in the vicinity of the impression at 675 MPa.	109
4.41	Profilometry of the specimen surface depicting the material pile-up on the specimen surface in the vicinity of the impressions in 316LN SS containing 0.22 wt. % nitrogen.	111
5.1	Schematic of the weld pad configuration used in the present investigation.	118
5.2	Typical microstructure of the base metal of 316LN SS weld joint exhibiting equiaxed grain structure.	120
5.3	Typical microstructure of the heat-affected zone of 316LN SS weld joint exhibiting coarse grains.	121
5.4	Typical microstructure of the weld metal of 316LN SS weld joint exhibiting duplex structure of austenite and ferrite.	121

5.5	Microhardness profile across the weld joint before creep testing.	123
5.6	Typical depth versus time curves for the weld metal, the base metal and the heat-affected zone of 316LN SS weld joint at 675 MPa.	124
5.7	Typical depth versus time curves for the weld metal, the base metal and the heat-affected zone of 316LN SS weld joint at 760 MPa.	124
5.8	Variation of impression velocity with test time showing the steady state impression velocity in the weld metal, the base metal and the heat-affected zone at 675 MPa.	125
5.9	Variation of impression velocity with test time showing the steady state impression velocity in the weld metal, the base metal and the heat-affected zone at 760 MPa.	125
5.10	Creep curves for the weld metal, the base metal and the heat-affected zone obtained from conventional uniaxial creep tests after Etienne et al. [8].	127
5.11	Comparison of steady state creep rate obtained from conventional uniaxial creep tests and impression creep tests on the weld metal.	128
5.12	Comparison of steady state creep rate obtained from conventional uniaxial creep tests and impression creep tests on the base metal.	129
5.13	Optical micrographs of impression creep regions in the base metal at 675 MPa: (a) three distinct regions in the vicinity of the impression, and (b) right corner of the impression showing extensive deformation in region 2.	131
5.14	Optical micrographs of impression creep regions in the heat-affected zone at 675 MPa: (a) three distinct regions in the vicinity of the impression, and (b) left corner of the impression at a higher magnification showing extensive deformation in region 2.	132
5.15	Optical micrographs of impression creep regions in the weld metal at 675 MPa: (a) left corner of the impression, and (b) right corner of the impression showing three distinct regions and extensive deformation in region 2.	133

5.16	Optical micrographs of impression creep regions in the base metal at 760 MPa: (a) three distinct regions in the vicinity of the impression, and (b) right corner of the impression showing extensive deformation in region 2.	134
5.17	Optical micrographs of impression creep regions in the heat-affected zone at 760 MPa: (a) three distinct regions in the vicinity of the impression, and (b) a higher magnification micrograph showing extensive deformation of grains in region 2.	135
5.18	Optical micrographs of impression creep regions in the weld metal at 760 MPa: (a) three distinct regions in the vicinity of the impression, and (b) right corner of the impression at a higher magnification showing extensive deformation in region 2.	136
6.1	Schematic illustration of an actual 3-Dimensional impression creep model and its simplified axisymmetric model.	140
6.2	An axisymmetric FE model and FE mesh which consists of linear quadrilateral elements with reduced integration of type CAX4R and linear triangular elements of type CAX3.	142
6.3	The two different meshes with extreme mesh sizes, a) 30 μm and b) 7 μm .	146
6.4	The comparison of variation of the Von Mises stress along the axial direction for two different mesh sizes of 30 μm and 7 μm , tested for 316LN SS at a load of 371 N.	147
6.5	The comparison of variation of the Von Mises stress along the radial direction for two different mesh sizes of 30 μm and 7 μm , tested for 316LN SS at load of 371 N.	147
6.6	The comparison of depth profiles for two different mesh sizes of 30 μm and 7 μm , tested for 316LN SS at load of 371 N.	148
6.7	Normalized contact stress distribution σ_y/P_m for cylindrical flat punch after Fischer-Cripps [12].	149
6.8	Normalized contact stress distribution σ_y/P_m for the cylindrical flat punch a) from the present FE model with fillet and b) from the analytical solution (Eqn. 6.5) which considered no fillet.	150

6.9	Comparison of FE results and the analytical results for the contact stress variation for the cylindrical punch. The Eqn 6.5 was used to calculate the analytical contact stresses.	151
6.10	(a)-(j) Contour plots of the Von Mises stress distribution in the specimen with time of loading. The total load applied was 530 N.	154
6.11	Variation of the Von Mises stress along the radial direction with increasing load in the loading step.	155
6.12	Von Mises stress distribution in the specimen after completion of loading; Load= 530 N.	157
6.13	(a)-(h) Contour plots of the Von Mises stress distribution in the specimen around indentation with increasing time of creep.	159
6.14	Graphical representation of the evolution of the Von Mises stress within the specimen during creep deformation; the distribution is along the axis of symmetry.	160
6.15	Optical micrographs showing the deformation in the impression creep tested specimen in 316LN SS containing 0.14 wt. % nitrogen tested at 948 K, under the punching stress of 675 MPa.	161
6.16	Typical indentation with material bulge/material pile-up around the indentation after impression creep test.	161
6.17	(a)-(h) Symbol plots of resultant displacement of nodes during loading. Figures illustrate how the material movement is directed during loading.	164
6.18	Schematic showing the region R1 and R2 in the specimen.	165
6.19	(a)-(c) Symbol plots of displacement of nodes in the axial direction with loading. Figures illustrate start of the material displacement in the upward direction towards specimen surface.	166

6.20	(a)-(n) Symbol plots of resultant displacement of nodes in the specimen in response to the indentation during different time of creep. The applied load was 530 N.	169
6.21	The evolution of material pile-up on the surface of the specimen during creep at a load of 597 N.	169
6.22	The evolution of material pile-up on the surface of the specimen during creep at a load of 530 N.	170
6.23	The evolution of material pile-up on the surface of the specimen during creep at a load of 464 N.	170
6.24	The evolution of material pile-up on the surface of the specimen during creep at a load of 371 N.	171

LIST OF TABLES

Table No.	Title	Page No.
2.1	Correlation factors for comparison of impression creep test results with corresponding uniaxial creep test results for various materials.	37
3.1	Technical specifications of the impression creep testing system.	56
3.2	Chemical composition (in wt. %) of type 316LN SS.	56
3.3	Details of preparation of the weld pad.	58
3.4	Chemical composition (in wt. %) of the 316LN SS weld joint.	58
6.1	Input creep properties for 316LN SS.	144

CHAPTER 1

Motivation, Objective and Scope of the Thesis

1.1 Introduction and Motivation

Austenitic stainless steels are an important class of stainless steels that have been extensively used in fast reactor applications, for high temperature components, primarily because of their excellent high temperature mechanical properties, superior corrosion resistance and adequate weldability. During service, these materials are exposed to challenging environments of intense neutron flux of about 10^{15} n/cm²s⁻¹, elevated temperature of 673-973 K under steady state operating condition, stress due to thermal gradients, mechanical loads and pressure from coolant flow, and liquid sodium coolant. The life of structural components operating at temperatures greater than 670 K is often limited by the creep and fatigue damage of structural materials and their weld joints. These critical issues of the reactor environment, its operating conditions and hence the requirement of stringent mechanical properties to withstand such environment for a long period of time, impose a great challenge for material scientists, metallurgists and engineers to carefully design and develop advanced structural materials with superior mechanical properties for these applications.

Nitrogen-alloyed low carbon grade type 316L(N) stainless steel (SS) is a modified version of 316 austenitic stainless steel. 316L(N) SS containing 0.02-0.03 wt.% carbon and 0.06-0.08 wt.% nitrogen has been employed as the primary structural material for out-of-core components such as main vessel, inner vessel and sodium pipe lines in India's Prototype Fast Breeder Reactor (PFBR). These materials are developed with a view to achieve improved creep strength, low cycle fatigue (LCF) properties,

creep-fatigue interaction properties, weldability, compatibility with liquid sodium and microstructural stability during its long design life of 40 years. These desired properties are obtained through a systematic, microstructurally based programme of alloy development which involves optimization of chemical composition in the alloy. So the alloy development programme becomes sufficiently broad based to encompass all the above mentioned properties and characteristics.

Detailed understanding of the creep deformation behavior of both parent materials and their weld joints becomes one of the major objectives of the alloy development programme which necessitates a large number of creep tests to be carried out at various stress levels and temperatures in order to understand the properties of the material and generate a large data base for design and validation.

Conventional uniaxial creep testing is the most commonly used test method for characterization of creep properties of materials. Creep testing requires a considerable volume of material for specimen preparation and necessitates many such specimens to carryout creep tests at different temperatures and stress levels in order to assess various creep deformation parameters. In addition, each creep test takes long duration. Hence, the test methodology is both time and material consuming. Further, when new materials are being developed, during their development stage, materials are often available only in limited quantities or as small volume. Also, it is important to realize that in any alloy developmental activity, it is essential to make the effective use of limited volume of material available for testing. Furthermore, there is a need to develop improved materials for enhancing safety and reduce the cost of fast reactors. In view of this, it is very important to establish a robust and reliable mechanical testing method that can accurately determine mechanical properties at both ambient and high temperatures from this small volume of materials. This is the motivation for the development of

innovative small specimen testing techniques for characterizing creep behavior of materials.

The following section gives a brief description of the phenomenon of creep and its standard evaluation procedures. Following this, an overview of the structural materials for Fast Breeder Reactors is provided. In the subsequent sections, the evolution of the impression creep testing technique for studying creep deformation behavior of materials is briefed. The basic aspects of the technique, its potential applications, advantages over the conventional creep testing, and its limitations are discussed. The last section of this chapter explains the objective and scope of the thesis.

1.2 Creep and Its Standard Evaluation Procedures - An Overview

1.2.1 Creep Phenomenon

The phenomenon of creep is defined as the time-dependent deformation of material under a constant stress, at high temperature [1]. Creep occurs in a wide range of materials at a wide range of temperatures. But, generally creep becomes of engineering significance at a homologous temperature greater than or equal to 0.4. Homologous temperature is defined as the ratio of the test temperature to the melting point of the material on an absolute temperature scale. i.e., T/T_{mp} , where T is the absolute test temperature and T_{mp} is the absolute melting temperature of the material.

1.2.2 Creep Testing

As mentioned earlier, conventional uniaxial tensile creep testing is the standard test method for characterizing creep behavior of materials. The test specimens used for these studies are of standard geometry and creep tests are carried out generally as per the ASTM standard E139 procedures [2]. A schematic of tensile creep test specimen is shown in Fig. 1.1. Figure 1.2 illustrates the tensile creep testing. A constant tensile

load is applied to the test specimen in its axial direction and the elongation of the specimen is measured using extensometer. The result of the creep test is the change in the strain with elapsed test time. Schematic diagram of a standard uniaxial creep testing machine is shown in Fig. 1.3.

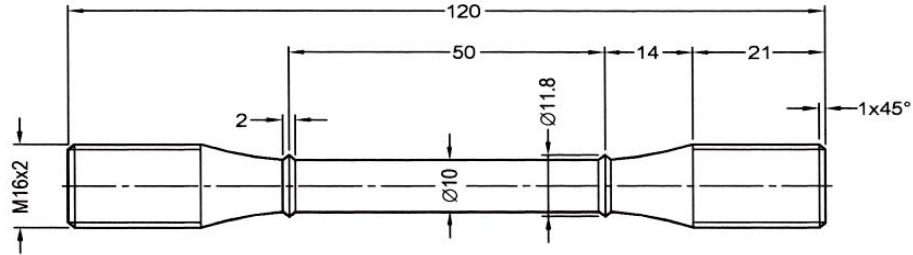


Fig. 1.1 A schematic of the tensile creep test specimen (dimensions are in mm).

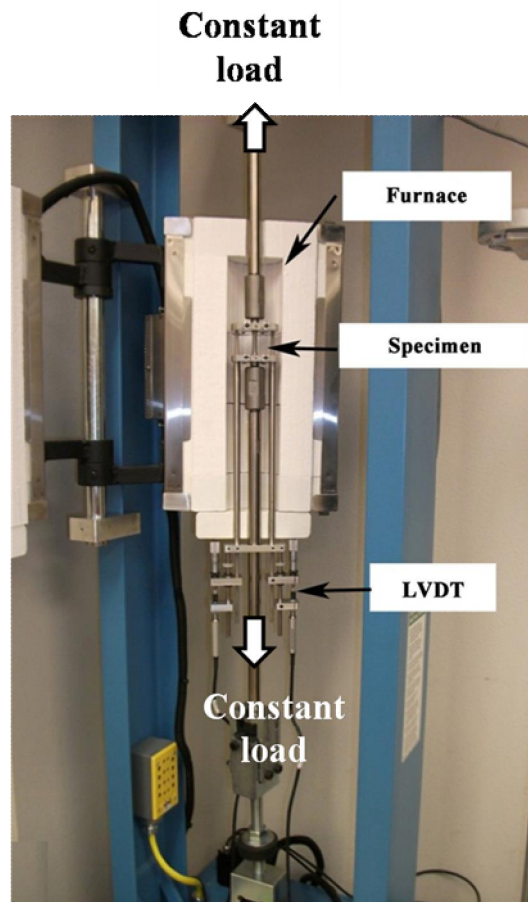


Fig. 1.2 An illustration of the tensile creep testing.

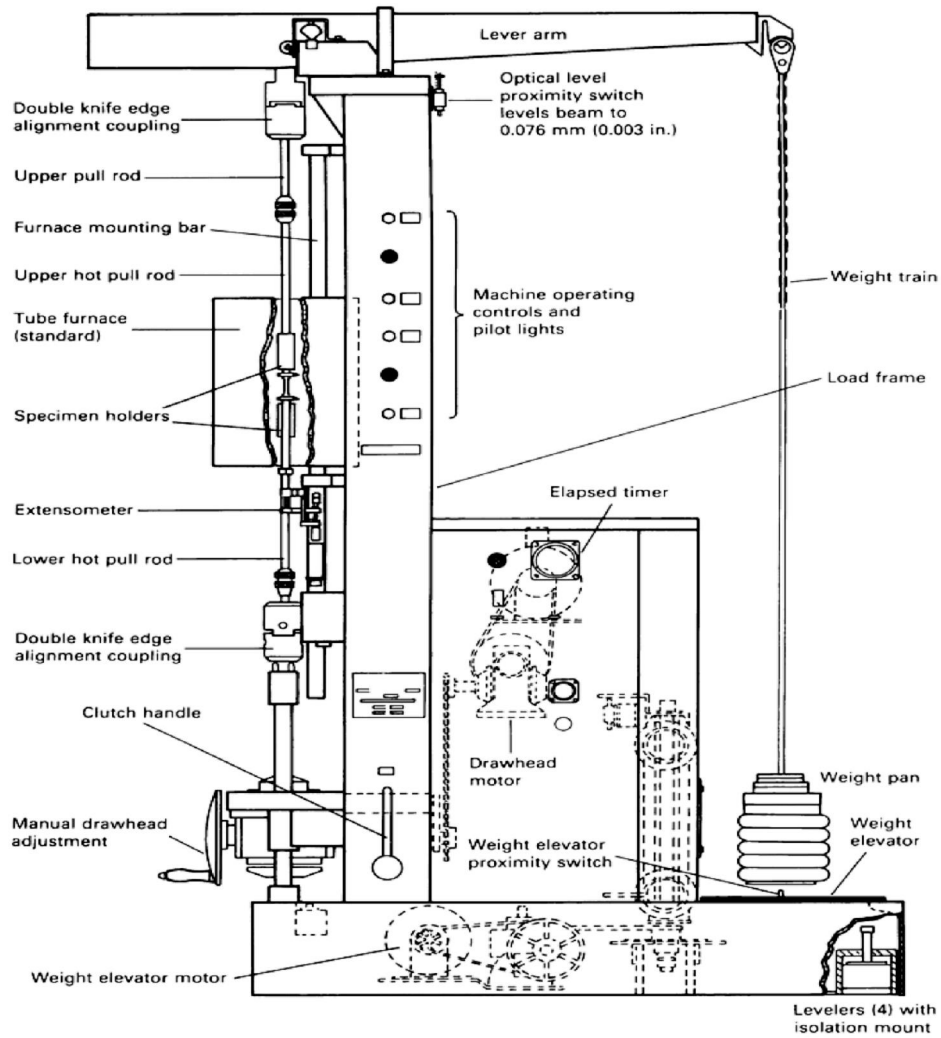


Fig. 1.3 Schematic of the tensile creep testing system.

1.2.3 Creep Curve

Uniaxial tensile creep curve exhibits three distinct creep stages, namely, a primary creep, a secondary creep and a tertiary creep stage. A schematic representation of the creep curve is shown in Fig. 1.4. After the specimen is loaded, the specimen undergoes an instantaneous loading strain (ϵ_0) which then follows the primary creep. The primary creep stage is a period of strain-hardening in which the creep rate decreases with time. In this process, creep resistance of the material increases due to work hardening. The

secondary creep stage which is often referred to as steady-state creep is a period of balance between the two competing processes of strain-hardening and thermal softening. The latter is a recovery process activated by the energy from the dislocation structure. This results in a region where the creep rate increases linearly with test time. The tertiary creep stage is characterized by an increasing creep strain rate culminating in fracture. The initiation of tertiary creep stage is due to a number of factors such as nucleation and coalescence of voids, grain boundary sliding which causes crack at grain boundary triple point junctions, localize necking giving rise to the development of a three-dimensional state of stress and microstructural changes such as coarsening of precipitates, dynamic recrystallization etc.

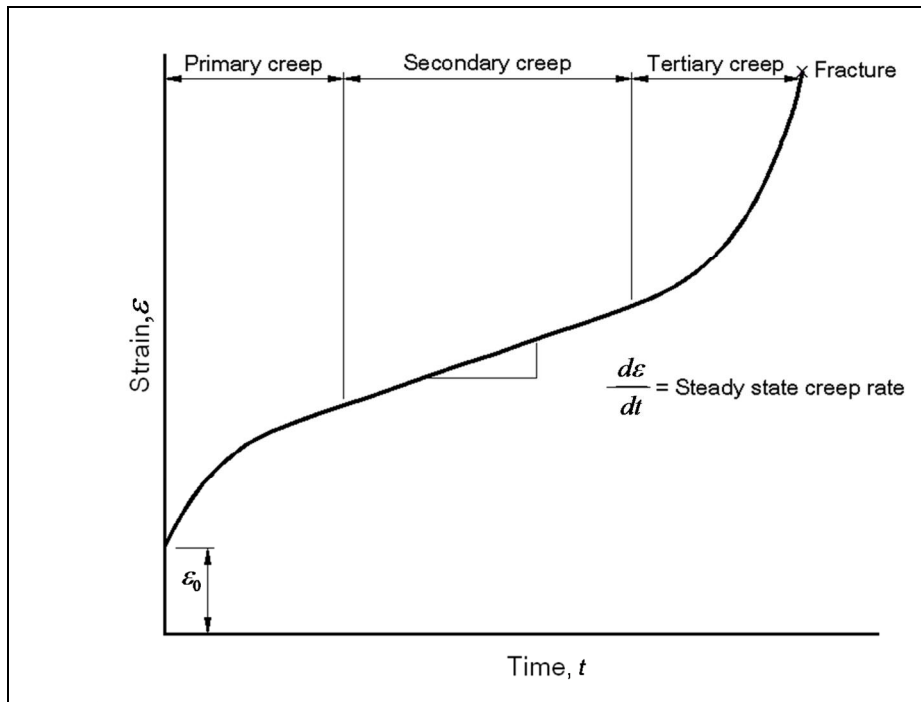


Fig. 1.4 Schematic of tensile creep curve showing three different creep stages.

1.3 Structural Materials for Fast Breeder Reactors (FBRs)

There is a range of materials employed for various components in FBR depending on the type of environment under which these components are operated during its service

[3, 4]. Based on this, the materials for FBRs are broadly classified as core, structural and steam generator materials.

The core of FBR which consists of fuel pins and wrapper tubes, experiences a continuous irradiation of high energy neutrons during its operation. As a result, core component materials undergo radiation damage such as void swelling because of fission gas release from nuclear reactions, irradiation creep and irradiation embrittlement. Hence, in addition to the requirement of superior creep strength and other mechanical properties, resistance to void swelling, irradiation creep, and irradiation embrittlement become additional considerations in the selection of materials for these components. Type 316 SS with 20% cold work has been chosen worldwide as a standard cladding and wrapper material for prototype and commercial FBRs. However, in view of reducing the fuel cycle cost and economic operation of FBRs a higher burn-up level is desired. Therefore, from this point of view of achieving a large burn-up level, an improved version of this material with a higher void swelling resistance is preferred. This has led to the development of titanium modified type 316 SS, known as alloy D9, which has been used in PFBR, and subsequently its improved version D9I which is envisaged to use for future core.

As mentioned earlier, out of core components include main vessel, inner vessel, sodium pipe lines and intermediate heat exchangers. These components are operated at high temperature for a long duration of 40 years and are subjected to cyclic and steady loading conditions. Structural materials for these components should have good creep strength, resistance to low cycle fatigue, creep-fatigue interaction and sodium corrosion. However, irradiation effects are not important for these components. Nitrogen alloyed low carbon austenitic stainless steel types 304 L(N) and 316 L(N) have been selected for structural components of PFBR.

Modified 9Cr-1Mo steel has been chosen as the steam generator structural material for PFBR because of its superior high temperature strength, microstructure stability, compatibility with liquid sodium and steam at high operating temperatures.

1.4 Impression Creep—An Innovative Testing Technique for Characterizing Creep Behavior of Materials

1.4.1 Evolution of the Impression Creep Technique

Assessment of creep properties of materials from indentation test method has been a subject of great interest to several researchers worldwide for more than last fifty years. Although the indentation test method is employed for evaluating the hardness of materials, it is potentially attractive for studying the creep deformation behavior of materials. The application of this particular test methodology to study creep behavior of materials was first attempted in the 1960s. The earliest investigation concerning the study of creep behavior from a simple long time indentation hardness test was carried out by Mulhearn and Tabor [5]. Subsequently, there has been continued attempts by several other researchers to obtain creep properties of materials from this long time indentation hardness test [6,7,8,9,10,11,12,13,14]. In this test, a constant compressive load is applied on the surface of the flat specimen through a suitable indenter such as spherical or pyramidal indenters, for a period which largely exceeds the duration of a standard hardness test. The variation of the indentation size, expressed as diameter in the case of Brinell test, diagonal length in the case of Vickers test, is measured as a function of time. Although some degree of success was achieved in these investigations, the major drawback in this methodology was the continuous decrease in the stress with the time of indentation. This is because of the geometry of the indenter employed in this test methodology. During the test, the contact area increases with time of indentation which results in continuous decrease in stress. Thus, no steady state is

attained. In order to get a constant stress and thereby a steady-state speed of indentation, the indenter shape has to be changed from a pyramidal or spherical shape to a cylindrical indenter with a flat end. It was Larsen-Badse [15] who first suggested the use of indenters of uniform cross section, circular or rectangular. This suggestion was not given due attention for a long time. In the mid 1970s, Chu and Li [16] introduced the impression creep test technique using cylindrical indenters with flat end. In the literature, generally one comes across two nomenclatures, namely, indentation creep and impression creep. The difference lies in the geometry of the indenter employed in the test. Indentation creep refers to creep tests using spherical or pyramidal indenters whereas impression creep refers to tests using a cylindrical indenter with flat end. Since the cross-sectional area of the indenter remains constant, a constant load applied to the punch implies a constant stress.

1.4.2 Basic Aspects of the Impression Creep Test Technique

In an impression creep test, a constant load (L) is applied to the test specimen through a flat-ended cylindrical indenter at high temperature. This results in a compressive load on the specimen. A test specimen and the impression creep testing are schematically illustrated in Figs. 1.5 and 1.6 respectively. During the test, the displacement of the cylindrical flat punch or the depth of penetration (h) is recorded as a function of the elapsed time. Initially, the penetration rate decreases with time and then reaches steady state after a transient period. During the steady state creep, depth of penetration increases linearly with test time. The plot of depth of penetration with elapsed test time yields the impression creep curve. Impression creep curves are similar to the conventional creep curves, but they exhibit only the first two characteristic stages of the creep curve namely, the primary creep and the steady state creep. A schematic of

the impression creep curve is shown in Fig. 1.7. There is no tertiary creep stage in impression creep curve. This is because of the fact that in impression creep test, loading is compressive in nature. As a consequence, creep cracks and necking of specimen which occur during the tertiary creep stage leading to fracture do not take place in impression creep test.

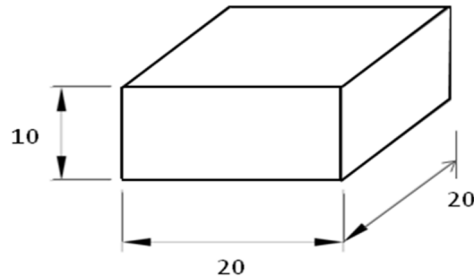


Fig. 1.5 A schematic of the impression creep test specimen (dimensions are in mm).

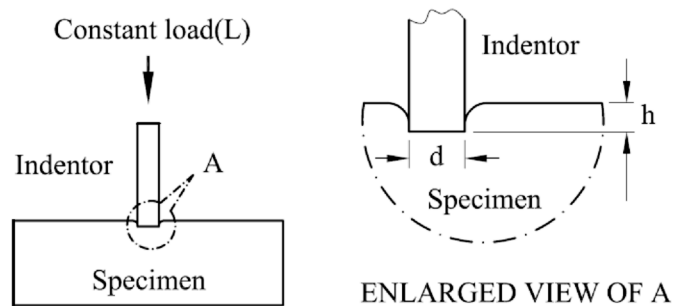


Fig. 1.6 Schematic illustration of the impression creep testing.

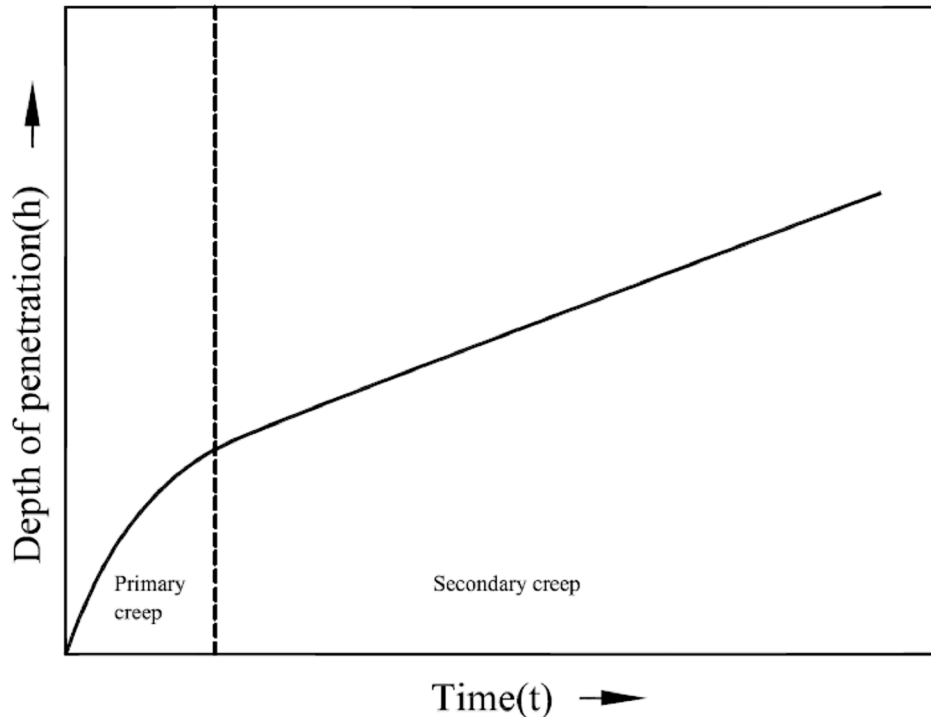


Fig. 1.7 Schematic of the impression creep curve.

1.4.3 Advantages and Applications of the Impression Creep Technique

Impression creep testing technique has several advantages when compared with conventional creep testing. These are,

1. Impression creep technique is material non-invasive and hence requires a small specimen for the tests.
2. The ease of specimen preparation, since only two relatively parallel surfaces are required, one of which is well polished.
3. Due to the localized nature of the indentation stress field, a relatively large number of indentations may be made on a single specimen. Hence, a large amount of creep data can be collected from a single specimen which not only reduces the effort for specimen preparation, but also reduces the specimen to specimen scatter in properties.

4. The test time required is short when compared to conventional creep test. Hence, it enables rapid screening of creep properties of small laboratory heats for optimizing the chemical composition in alloy development programme.
5. Characterization of creep properties of different and narrow microstructural regions in the heat affected zone of weld joints, which is not possible to be determined in conventional creep tests.
6. Since the test requires small specimen, it is attractive for remnant life assessment studies where it is not desirable to remove large amount of material from an operating component.
7. Because of the small indentation left in the specimen, the technique is in a sense nearly non-destructive; the small amount of compressive residual stresses remaining after the tests is not considered to be deleterious.
8. Impression creep technique is useful for studying creep properties of ceramic materials, glass, composite materials where it is not possible to machine conventional creep specimens.
9. Advantages as compared with other small specimen testing techniques: The other small specimen testing techniques such as the miniaturized uniaxial creep test, the small punch creep test, the shear punch creep test, the small ring creep test etc are also used for determining creep properties of materials. However, impression creep technique is considered to be a very strong tool and advantageous over other techniques because of the reasons such as the steady state creep stage can be clearly identified from the impression creep curves even at high stresses and temperatures, while it may be difficult to identify the exact transition between the primary, secondary and tertiary creep stages, in the case of miniaturized uniaxial creep test, small punch creep tests and shear

punch creep tests. Further, it is easy to probe narrow regions in HAZ of weld joints from impression creep tests while it is difficult to extract the specimen from such regions for other miniature specimen creep tests. Although the small ring creep tests are used for obtaining secondary creep behavior, it has limitation to study creep behavior of different narrow regions in weld joints on account of the specimen geometry required for such tests.

1.4.4 Limitations of the Impression Creep Technique

Despite these advantages, impression creep testing technique has few limitations. These are,

1. Rupture life cannot be determined by this technique because there is no fracture of the sample.
2. Since the test time is generally short, typically about a few hundreds of hours, creep behavior due to long time concurrent microstructural changes occurring in engineering alloys at high temperatures cannot be captured.
3. Although the test is relatively easy to perform and requires shorter time, interpretation of the results is difficult on account of the complex multi-axial nature of the stress beneath the indenter and the continuously varying amount of material under the indenter which is experiencing elastic, plastic and creep deformation.

1.5 Objective and Scope of the Thesis

The objective of this thesis work was to establish a unique impression creep testing facility at Indira Gandhi Centre for Atomic Research (IGCAR) and to study the creep deformation behavior of 316LN stainless steels and its weld joints using this technique. This thesis demonstrates the applicability of impression creep technique for the alloy development activity and its suitability to characterize creep deformation behavior of

narrow microstructural regions, namely, the heat-affected zone, the base metal and the weld metal in weld joints. The organization of the thesis is as follows. Chapter 2 details the literature in the area of impression creep testing technique which includes the investigations carried out by several researchers worldwide on a wide range of materials. Chapter 3 is a description of the impression creep testing system established at IGCAR, materials investigated and the characterization tools which are employed for the analysis in this work. Extensive studies on impression creep behavior of 316LN SS containing 0.07, 0.11, 0.14 and 0.22 wt. % nitrogen has been carried out. This is detailed in the Chapter 4. Chapter 4 also discusses detailed experimental investigations on the shape and size of the plastic zone, the extent of deformation and the microstructural evolution in the vicinity of the impression. Impression creep technique has been employed to characterize creep deformation behavior of the narrow heat-affected zone, the base metal and the weld metal of 316LN SS. This is explained in the Chapter 5. An axisymmetric Finite Element Model of indenter-specimen system has been developed using ABAQUS finite element analysis software. Detailed analyses of the stress distribution under the punch and its evolution during indentation, the size and shape of the resulting plastic zone, the mechanics involved in the material flow in response to the indentation and mechanism of material pile-up on the specimen surface have been investigated. This is detailed in the Chapter 6. Chapter 7 summarizes the overall results and gives in brief the suggestions for future work.

References

-
- [1] G.E. Dieter, "Mechanical Metallurgy", McGraw-Hill, London, 1988, p.432.
- [2] ASTM E-139-06, "Standard Test Method for Conducting creep, Creep-rupture, and Stress-rupture Tests of Metallic Materials", ASTM International, West Conshohocken, 2006.
- [3] B. Raj, S. L. Mannan, P.R. Vasudeva Rao and M.D. Mathew, *Sadhana*, 27(2002) 527-558.
- [4] T. Jayakumar, M.D. Mathew, K. Laha and R. Sandhya, *Nucl. Eng. Design.*, 265(2013) 117561180.
- [5] T.O. Mulhearn and D. Tabor, *J. Inst. Met.*, 89 (1960) 7-12.
- [6] P. M. Sargent and M. F. Ashby, *Mater. Sci. Technol.*, 8 (1992) 594-601.
- [7] H. D. Merchant, G. S. Murty, S. N. Bahadur, L. T. Dwivedi and Y. Mehrotra, *J. Mater. Sci.*, 8 (1973) 437-442.
- [8] O. D. Sherby and P. E. Armstrong, *Metall. Mater. Trans. B.*, 2 (1971) 3479-3484.
- [9] R. M. Hooper and C. A. Brookes, *J. Mater. Sci.*, 19 (1984) 4057-4060.
- [10] G. Cseh, N. Q. Chinh, P. Tasnadi and A. Juhasz, *J. Mater. Sci.*, 32 (1997) 5107-5111.
- [11] G. Cseh, N. Q. Chinh and A. Juhasz, *J. Mater. Sci.*, 17 (1998) 1207-1209.
- [12] M. Fujiwara and M. Otsuka, *J. Mater. Sci. Eng. A.*, 319-321 (2001) 929-933.
- [13] U. K. Viswanathan, T. R. G. Kutty, R. Keswani and C. Ganguly, *J. Mater. Sci.*, 31 (1996) 2705-2709.
- [14] B. N. Lucas and W. C. Oliver, *Metall. Mater. Trans. A.*, 30 (1999) 601-610.
- [15] J. Larsen-Badse, ORNL-TM-1862 Report, 1967.
- [16] S. N. Chu and J. C. M. Li, *J. Mater. Sci.*, 12 (1977) 2200-2208.

CHAPTER 2

Literature Review

2.1 Introduction

The present chapter on literature review is concerned with various aspects of the impression creep testing technique such as origin of the concept and advances in understanding the technique to emerge as a successful material non-invasive tool for evaluation of creep properties of materials. The chapter reviews the experience of researchers in using impression creep technique to characterize creep behavior of wide range of materials. The chapter also reviews correlation between impression creep and uniaxial creep test results in different materials, current understanding of the plastic zone and finite element analysis of impression creep.

2.2 Impression Creep Test Technique: The Genesis

The concept of studying creep behavior of materials from impression creep technique has its origin in indentation hardness tests. The following sections explain how the technique has evolved as a useful tool to study creep deformation behavior of materials from a simple indentation hardness test.

2.2.1 Indentation Hardness

Hardness, in a broad sense, is the resistance of the material to deformation. For metals and alloys, the property is the measure of their resistance to permanent or plastic deformation [1]. Hardness test is essentially a means of giving a quantitative value to the material's ability to resist local deformation [2].

The indentation hardness test is one of the hardness measurement techniques which is widely used for evaluating the hardness of metal and alloys. In indentation hardness test, an indenter is pressed on to the surface of the material to be tested under a specific load for a definite time, and the size of the permanent plastic impression is measured. The indentation hardness then expressed as the ratio of the applied constant load to the area of the indentation. The ease with which the indentation hardness test can be performed has made it the most common method of inspection for metals and alloys which provides a very simple and nearly non-destructive means for assessing the resistance of metals and alloys to plastic deformation.

The first indentation hardness test was introduced in 1900 by J. A. Brinell [3]. In this test, a hard steel ball (usually of diameter 1 cm) is pressed on to the surface of the metal of interest under the constant load applied for a period of 30 s [2]. Subsequently, other indentation hardness measurement techniques were also introduced, namely, the Vickers hardness test [4] which uses diamond pyramid indenters and the Rockwell hardness test which employs conical diamond indenter with spherical tip.

2.2.2 Relationship of Indentation Hardness with Other Material Properties

While indentation tests have traditionally been used to evaluate hardness of materials it is also attractive to characterize other mechanical properties such as tensile and creep properties of materials. Its attractiveness for these applications stems from the fact that both hardness and tensile test measure the resistance of metal to plastic flow. The well known relationship of hardness (H , or mean contact pressure P_m) with uniaxial flow stress Y of the material with a proportionality constant C , known as constraint factor, was proposed by Prandtl [5] and Tabor [6] which is given as,

$$P_m = H = CY \quad (2.1)$$

In view of the above correlation, several researchers attempted to extend indentation test method to study time independent (tensile properties) as well as time dependent flow behavior (creep properties) of materials. The indentation test method for studying tensile behavior of materials has now developed further as the automated ball indentation (ABI) technique [7, 8].

2.2.3 Indentation Test Method to Study Creep Behavior of Materials

The indentation test method for characterizing creep behavior of a localized volume of material was started from hot hardness tests. Some of the early attempts to investigate the activation energy for creep and self-diffusion of materials was made by Mulhearn and Tabor [9] and Sherby et al. [10]. Subsequently, there have been many attempts by several other researchers also [10, 11,12,13,14,15,16,17,18]. In hot hardness test, in a similar manner to a hardness test, an indenter (such as spherical or pyramidal indenter) is forced into the surface of a flat specimen at elevated temperature (in the creep regime) by applying a constant load to the indenter, and measure the indentation size for different dwell time. The difficulty associated with hot hardness test is that when the hardness decreases with time, the stress also decreases on account of the geometry of the indenter used in these studies. Therefore no steady state is obtained [19]. This has been explained in Chapter 1. In order to get a constant stress and thereby a steady state speed of indentation, the indenter shape was changed from a pyramidal, spherical or conical shape to a cylindrical indenter with flat end. In the mid 1970s, J.C.M. Li [19] developed this new impression creep technique using a cylindrical punch. In contrast to conventional tensile creep tests, indentation test produces compressive stress and is not suitable to give information on materials' end-of-life behavior. Nevertheless,

indentation tests can be used to study secondary creep deformation behavior of materials.

2.3 Impression Creep Studies on Different Materials

Impression creep test was first reported on succinonitrile crystals by Chu and Li in 1977 [19]. Impression creep curves exhibited a primary and a secondary creep stages as shown in Fig. 2.1. It was also found that the steady state impression velocity is a power function of punching stress in the case of molecular crystals.

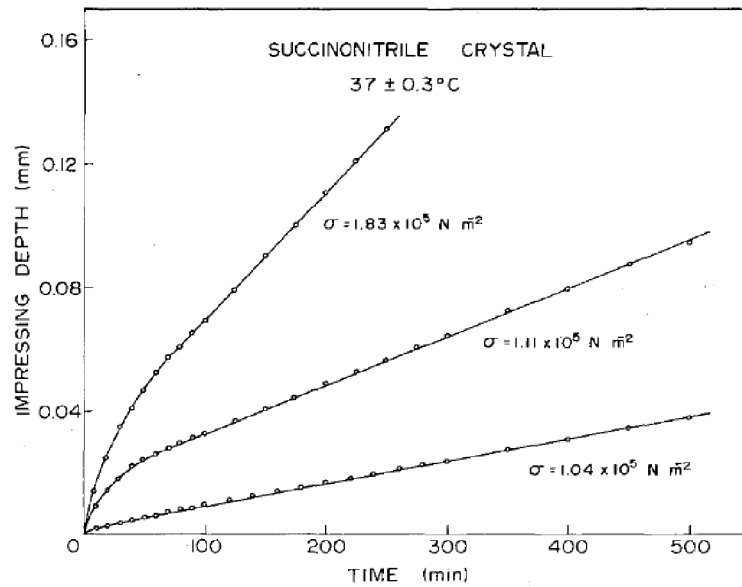


Fig. 2.1 Typical impression creep curves for succinonitrile crystals [19]

Encouraged by this first attempt, Yu and Li [20] conducted impression creep tests on LiF single crystals. Followed by J.C.M. Li, a number of other researchers have employed impression creep technique to characterize creep properties of a variety of materials which include metals and alloys, weldments, composites, ceramics, glasses and polymers. Investigations carried out on these materials are discussed in the following sections.

2.3.1 Metals and Alloys

The first metal on which impression creep experiments were conducted was β -Tin single crystals by Chu and Li [21, 22]. Typical depth versus time curves obtained for this material is shown in Fig. 2.2. The stress and temperature dependence of steady state impression velocity was investigated in the single crystal in three orientations, [001], [100] and [110], in the punching stress range $7.5\text{--}20\text{ MNm}^{-2}$. The stress exponent values varied between 3.6 and 5.0, in agreement with the previously reported results from conventional creep testing. The activation enthalpy for high temperature process was found to be $25\text{--}26\text{ kcalmol}^{-1}$ which was comparable to the activation enthalpy for self diffusion 25.6 kcalmol^{-1} . The equivalent uniaxial steady state creep rate was obtained by dividing the steady state impression velocity by the depth of the plastic zone which was equivalent to the diameter of the punch. The ratio of the punching stress to the uniaxial stress for the same creep rate was 3.5 to 3.9 in the [100] orientation and 2.8 in the [001] orientation.

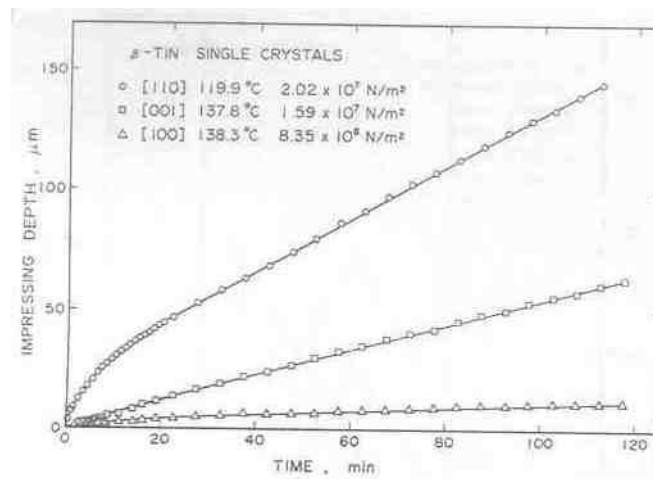


Fig. 2.2 Typical impression creep curves for β -Tin single crystals after Chu and Li [21, 22].

Murty and Sastry [23] studied the impression creep behavior of cadmium metal in the temperature range 300-475 K using specimens of dimension $20 \times 10 \times 8 \text{ mm}^3$. The steady state impression velocity exhibited the same stress and temperature dependence as was observed in conventional tensile creep tests with the same power law exponent values. A comparison of the stress exponent values obtained from impression and uniaxial tensile creep tests is shown in Figs. 2.3(a) and (b). The activation parameters for thermally activated dislocation glide estimated from impression creep tests were in agreement with those parameters estimated from conventional tensile creep tests on same material. They used the punch diameter as the gage length and the steady state impression velocity was divided by the indenter diameter to convert it to the equivalent uniaxial steady state creep rate. The punching stress was divided by a factor 4 to convert it to equivalent uniaxial stress. The creep data obtained from two techniques were found to be comparable at all three temperatures for the above correlation factors of $\alpha = 1/4 = 0.25$ and β is the diameter of the indenter used as shown in Fig 2.4 (the correlation factors α and β are defined in section 2.4).

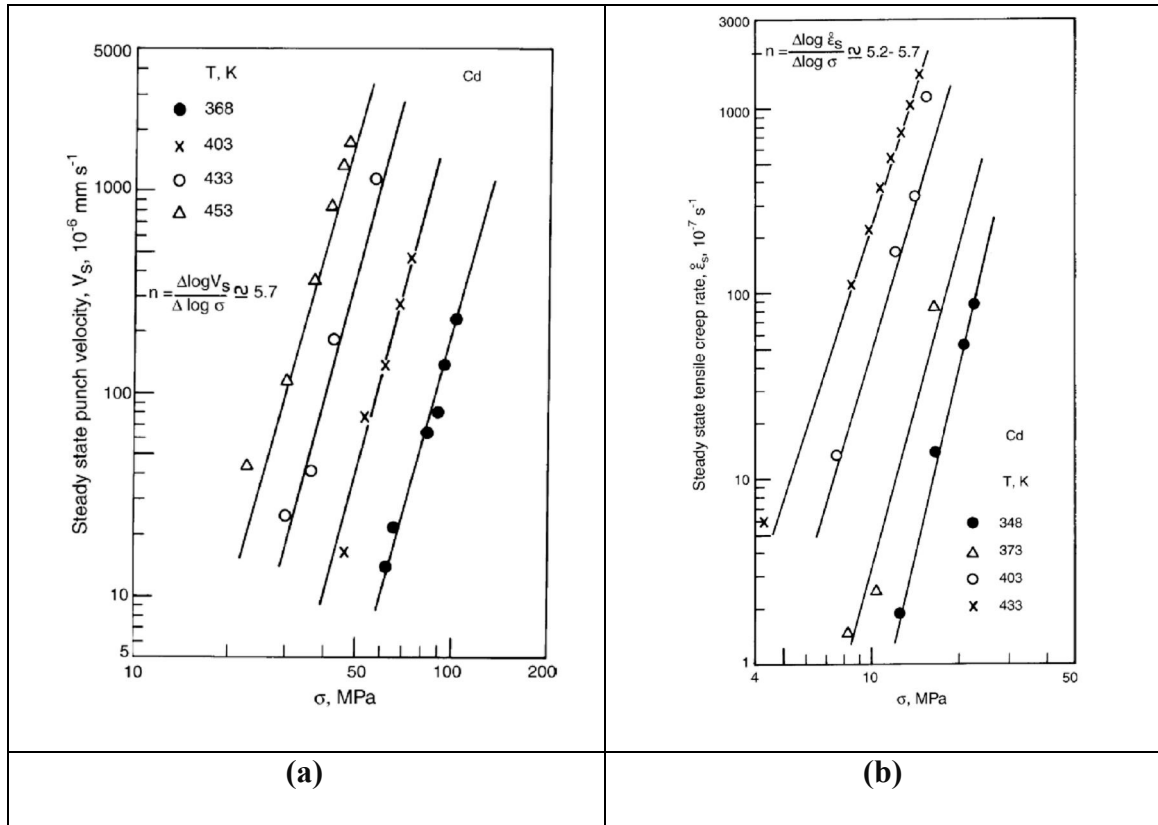


Fig. 2.3 Stress dependence of a) steady state impression velocity and b) steady state creep rate (tensile creep tests), showing close agreement in stress exponent values obtained from both the test techniques in Cd metal [23].

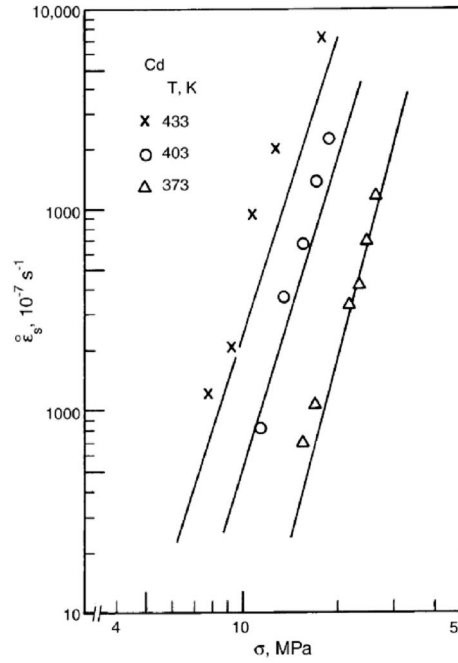


Fig. 2.4 Correlation between tensile creep and impression creep test results on Cd metal for a stress conversion factor of 4 ($\alpha = 1/4 = 0.25$): solid lines-tensile creep; data points-impression creep [23].

Sastry [24] conducted impression creep tests and conventional tensile creep tests on magnesium at 478 K, to study the relationship between the results from two test techniques. The correlation between the conventional tensile creep and impression creep parameters in magnesium for a stress conversion factor of 3 ($\alpha = 1/3 \approx 0.33$) is shown in Fig. 2.5. It was found that the factor equal to 0.33 involved in the conversion of stresses is for an isotropic material like magnesium.

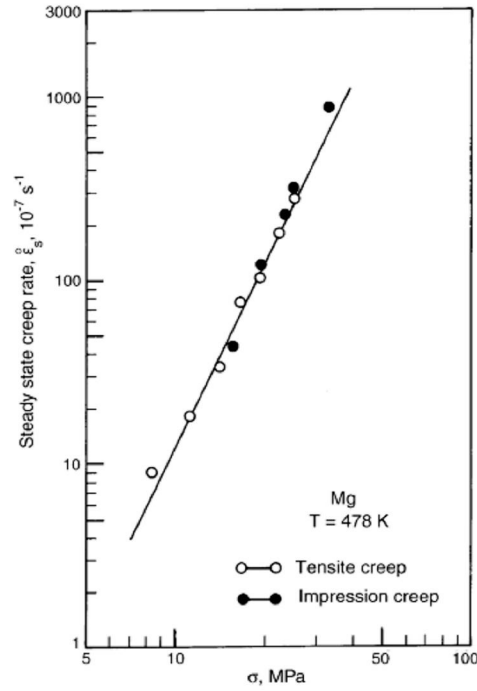


Fig.2.5 Correlation between tensile creep and impression creep parameters in magnesium for a stress conversion factor $\alpha = 1/3 \approx 0.33$ [24].

Murty and Sastry [25] investigated impression creep behavior of single crystal and polycrystalline Zn in the temperature range 300-500 K. They found the same stress and temperature dependencies of steady state creep rates as was observed from uniaxial tensile creep tests. The stress exponent value of 4.6 obtained from impression creep tests was in close agreement with the value of 4.0 obtained from tensile creep tests on the polycrystalline Zn. It was also observed that the stress exponent value of 4.4 obtained for single crystal Zn was close to the stress exponent value for polycrystalline Zn. The activation area and activation enthalpy obtained from impression creep tests for both single crystal and polycrystalline Zn were found to be similar.

Godavarti and Murty [26] employed impression creep technique to investigate the anisotropy in creep behavior of Zn. The power law exponent values of 3.4 ± 0.1 and

4.4±0.2 for two different orientations were in good agreement with the values reported by Murty and Sastry [25] as discussed above. The activation energy in high temperature regime was 82±5 kJ mol⁻¹ and in low temperature regime was 58±8 kJ mol⁻¹. The rate controlling creep mechanism was identical for different orientations. The exhibited anisotropy was supposed to be caused from grain size differences and texture differences in the materials. The study demonstrated the ability of impression creep technique to characterize anisotropic creep behavior in polycrystalline materials like Zn.

Juhasz et al. [27] performed impression creep tests on fine grained Al alloys in the temperature range 723-823 K. A cylindrical flat punch of 1 mm diameter was employed. They used correlation factors $\alpha = 1/3 \approx 0.33$ and $\beta = 1$ to convert the punching stress and the steady state impression velocity to equivalent uniaxial stress and steady state creep rate, respectively. The activation energy and the strain rate sensitivity values determined from impression creep tests were in good agreement with the results obtained from tensile creep tests.

Hyde et al. [28] carried out impression creep tests on 316 stainless steel at 873 K for which conventional uniaxial creep test results were available [29]. Impression creep tests were performed in a different way which is described as follows. A Mayes servo electric machine was used for conducting impression creep tests. The tensile creep specimens of 10 mm diameter and 50 mm gauge length were cut at the middle, on a plane perpendicular to the longitudinal axis to produce into two halves, which were tested simultaneously. These two halves of the specimens were threaded into a collar, which was located on the loading bar. The indenter was positioned at the centre of the bottom half-specimen. The cross head of the machine was raised until the indenter came into contact with the top half-specimen. The specimen-indenter

assembly, the extensometer and thermocouple were situated inside the furnace. Cylindrical indenters with flat end, made of zirconia (zirconium oxide), having indenter diameters 1.5 mm and 3 mm were employed in the tests. The punching stress was as high as 1000 MPa which was selected according to the uniaxial creep stress which was as high as 330 MPa. Impression creep test results were reported to be in close agreement with the uniaxial tensile creep tests results for correlation factors $\alpha = 0.296$ and $\beta = 0.755$ which were obtained using reference stress method. It was shown that when the impression creep data were converted to uniaxial creep data based on the reference stress approach, the two sets of data agreed well with each other. It was noted that since the effective gage length was very small (1.13 mm) in impression creep, the displacement measurements must be conducted very accurately when compared with uniaxial testing for which the gage length was 50 mm. Similarly, the load measurements must be conducted more accurately in impression creep due to the small cross-sectional area.

Kutty et al. [30] studied the impression creep behavior of δ -phase of U650%Zr alloy using impression creep technique in the temperature range of 798–848 K, under different stress levels between 12.97 and 37.05 MPa. The impression creep curves were similar to the conventional creep curves with steady state attained after an initial transient period. A power law behavior was displayed by all the alloys with the stress exponent ranging from 6.5 to 7. The activation enthalpy for the alloy was found to be independent of stress with an average value of 106 ± 4 kJ/mol. Climb-controlled dislocation creep was considered to be the rate-controlling deformation mechanism for this alloy.

2.3.2 Weldments

Characterizing creep properties of narrow microstructural zones in weld joints is one of the unique advantages of the impression creep technique. Gibbs et al. [31] employed impression technique to determine the local creep properties across weld joint in a pure aluminum gas tungsten arc (GTA) weldment and in a dissimilar weld joint of 316 stainless steel and 2.25Cr-1Mo steel. The flat-ended cylindrical indenters made of Al_2O_3 of diameter 0.92 mm were used for Al weldments and indenters made of molybdenum which had diameter of 1 mm were used for steel weldments. The specimen thickness was about 8 mm. The impression creep testing surface was polished and slightly etched with 2 % nital to reveal the fusion line. A punching stress of 20 MPa was applied at 623 K for Al weld and punching stress of 172 MPa was applied at 948 K for steel weld. Reported results for the dissimilar weld joint are shown in Fig. 2.6. In the dissimilar weld joint, HAZ exhibited high impression velocity due to the carbon depletion in this zone and the creep strength degraded significantly with aging at high temperatures because of the creep cracking which was observed in this region during service.

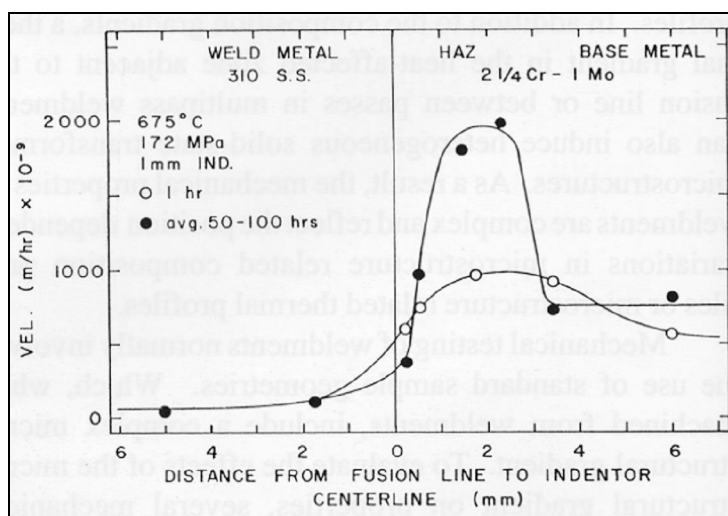


Fig.2.6 Impression velocity vs. distance from the fusion line for 2.25Cr-1Mo steel to type 316 SS weldment joined with type 310 SS filler material. [31].

Wang [32] conducted impression creep tests on a multi-pass ASTM A36 weldment at a punching stress of 252 MPa in the temperature range 820-850 K. A qualitative analysis of the activation energy and stress exponent for the interface region of the solidified weld metal and the reheat affected zone was performed. However, these studies neither showed the impression creep curves of each test nor aimed at establishing any correlation between the impression creep test results and uniaxial creep test results.

Yu et al. [33] studied the mechanical properties of high energy laser beam welds in A36 steel from impression tests at constant punch penetration rates. The yield strength, ultimate tensile strength, strain rate sensitivity, strain hardening coefficients, etc., were obtained at the fusion zone, heat affected zone (HAZ) and the base metal in the as-welded condition and after stress relief. However, impression creep curves for the tests conducted were not shown in this literature.

Hyde et al. [34, 35] performed impression creep tests on HAZ material in a P91 weld joint at 923 K and on three different ex-service 1/2CrMoV steam pipe samples at 873 K, in the stress range 70-93 MPa, using a rectangular indenter of width 1 mm. Hyde's group is the first and the only group which employed rectangular indenters which give a constant stress for a constant applied load like in the case of flat-ended cylindrical indenters. The rectangular indenters were used in place of cylindrical punches. The test specimen-indenter assembly is shown in Fig. 2.7. The specimen dimension used was 10 x 10 x 2.5 mm. The typical creep curves obtained in their study is shown in Figs. 2.8(a) and (b).

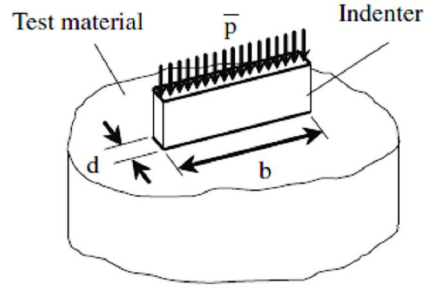


Fig. 2.7 Rectangular indenter-specimen assembly employed by Hyde and Co-workers for impression creep testing of HAZ material in a P91 weld tested at 923 K; The width d of the indenter was 1 mm [34, 35].

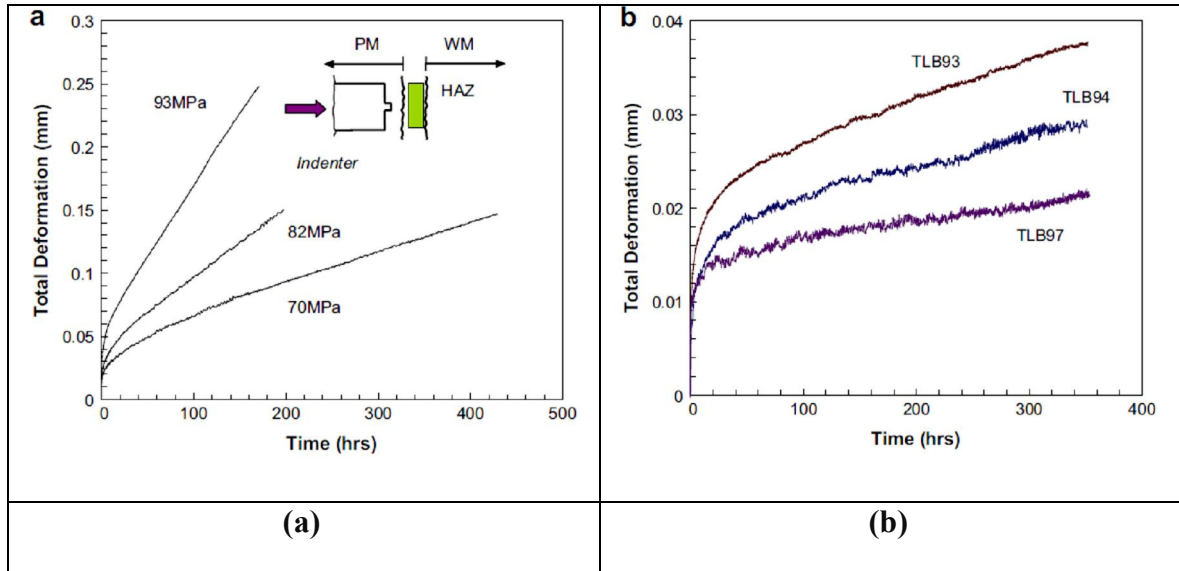


Fig. 2.8 Impression creep curves a) for HAZ material in a P91 weld tested at 923 K, under different stress levels and b) for three different ex-service 1/2CrMoV steam pipe samples tested at 913 K at 90 MPa [34].

Hyde et al. [36] performed creep tests on CrMoV weldments at 913 K using uniaxial, notched, impression and cross weld creep test specimens. The aim of the study was to determine the material constants in creep constitutive equations for the

parent, weld metal and HAZ material which were to be used in FEM modeling. For impression creep tests, a coin shaped specimen was used and a rectangular indenter of width 1 mm was employed. All the tests were carried out in air. Typical impression creep curves for HAZ at different punching stresses are shown in Fig. 2.9. Impression creep test results were consistent with uniaxial creep test results. The authors also pointed out that the effect of oxidation damage on the impression creep test results was more significant than that on the uniaxial creep test results.

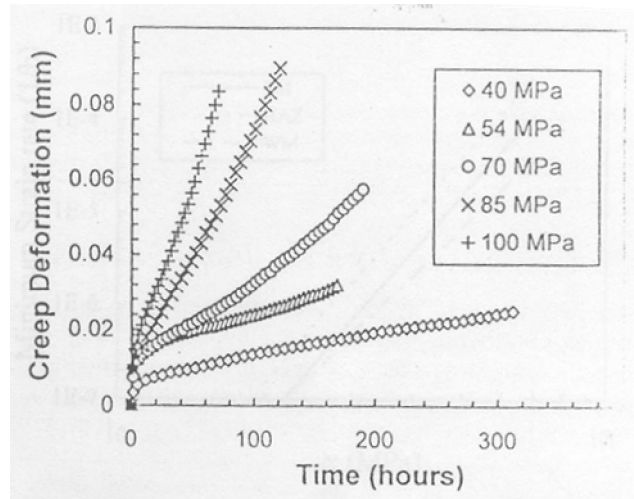


Fig. 2.9 Impression creep curves for HAZ material of CrMoV weldment tested under different stress levels [36].

Sun and Hyde [37] discussed the application of impression creep technique to weldments when direct determination of creep properties by conventional uniaxial tests is impossible.

Lisin et al. [38] employed impression creep technique to evaluate the position-dependent creep behavior across the interface of a roll-bonded Cu-brass laminate which represented an ideal two component weldment. Impression creep tests were carried out at temperatures between 723 and 798 K, and punching stresses between 90

and 117 MPa, using a 1 mm diameter punch made of molybdenum. Impression creep tests were performed using the testing system developed by Gibbs et al. [31]. The results showed that the material below the punch controlled the punch velocity which indicated the localized nature of the test.

Prasanna et al. [39] employed impression creep technique to assess the deterioration effects of AISI 316L stainless steel welds under different ageing conditions. The tests were carried out under punching stresses 440MPa, 495MPa, 550MPa, and 660 MPa. The technique was demonstrated to be useful for comparing the parent metal and weld metal behavior at different levels of aging.

2.3.3 Composites, Ceramics and Glasses

Impression creep technique is most suitable for evaluating creep properties of ceramics, glasses and composite materials as uniaxial creep test specimens from these materials are difficult to fabricate. Mondal and Kumar [40] employed impression creep test technique to investigate creep behavior of AE42 magnesium alloy reinforced with saffil short fibres and SiC particulates, in the temperature range of 448-573 K, under stress levels ranging from 60 to 140 MPa. Normal creep behavior was observed at all the stresses employed at 448 K, and at all the stresses up to 80 MPa, at 513 K. However, a reverse creep behavior, i.e., strain rate decreasing with strain after a steady state creep was observed, above 80 MPa at 513 K, and at all the stresses employed at 573 K, as shown in Figs. 2.10(a)-(d). The reverse creep behavior was attributed to the fibre breakage during creep. Viscous glide as well as dislocation climb were found to be the dominant creep mechanisms in the stress and temperature range employed. A similar observation of strain rate decreasing with time after reaching a steady state was also made by Cseh et al. [41] in their indentation creep studies on Al_2O_3 fibre-reinforced M124+s metal matrix composite (MMC) in the temperature range of 523-

623 K. They correlated this creep behavior with the changes of the microstructure below the indenter during the deformation process. The unreinforced M124 alloy exhibited normal impression creep curves with primary and a secondary creep stage. It should be noted that the reverse creep behavior where strain rate decreases with time after steady state creep is reached was reported only in composite materials.

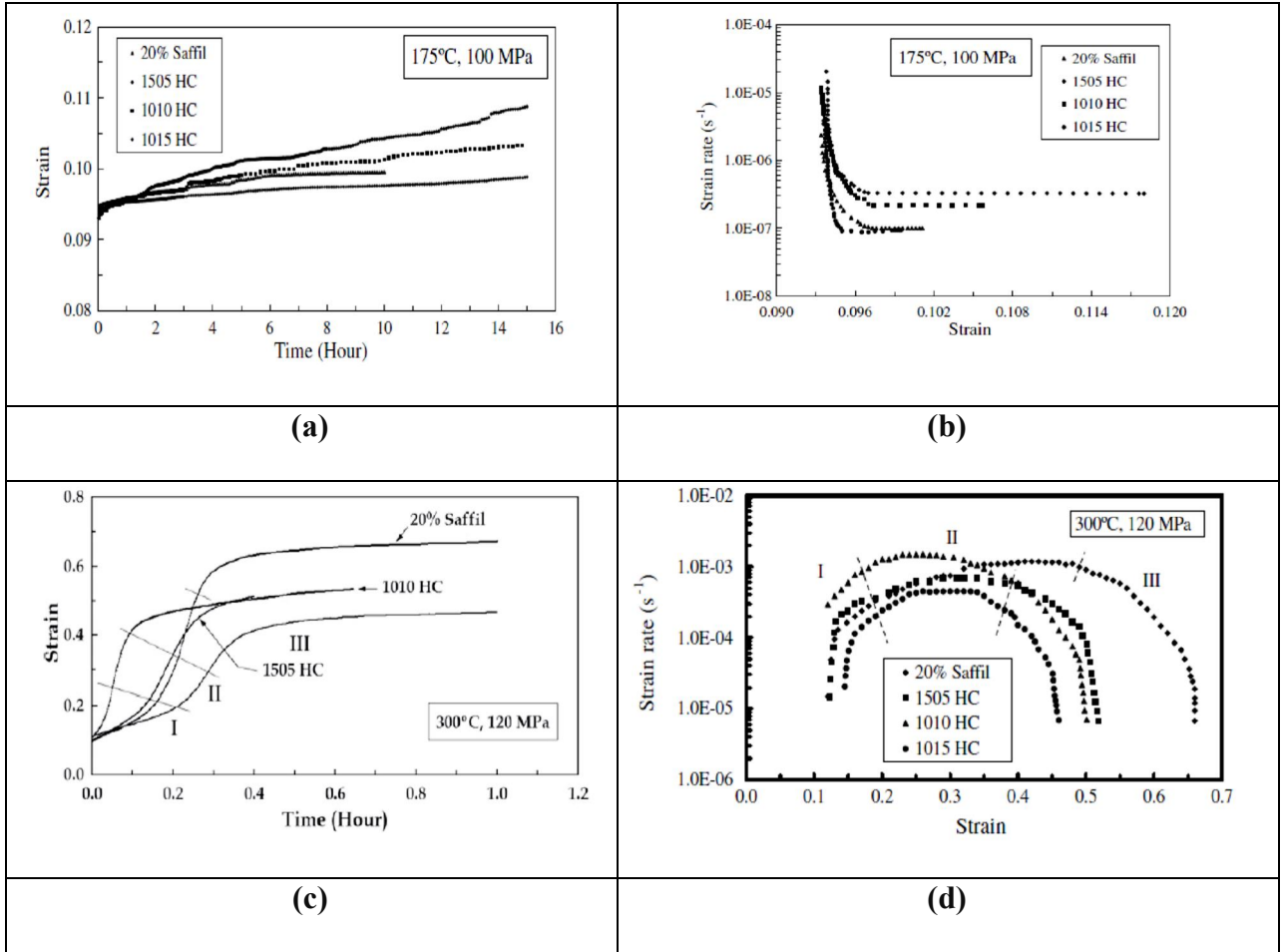


Fig. 2.10 a) Impression creep curves for the composite tested at 448 K and 100 MPa in the transverse direction b) the strain rate vs. strain curves corresponding to (a), c) a reverse creep behavior, i.e., strain rate decreasing with strain, tested at 573 K and 120 MPa, and d) the strain rate vs. strain curves corresponding to (c) [40].

Chinh et al. [42] conducted impression creep tests on a magnesia-silica glass (SiO_2 , Na_2O , CaO , MgO) at different constant punching stresses, in the temperature range between 773 and 923 K. They evaluated stress exponent to be 1 and the activation energy to be 440 kJmol^{-1} which were in agreement with the results obtained from the usual viscosity measurements by the conventional fiber elongation method.

Dorcakova et al. [43] used impression creep technique to study creep behavior of free-standing Y-ZrO₂ (partially stabilized zirconia with 7 wt. % yttria) layer and Sc-Si-Mg-O-N oxinitride glass. A hot pressed SiC cylindrical indenter with flat end was used. Tests were conducted in the temperature range of 1133-1573 K, in the punching stress range of 20-100 MPa. The stress and temperature dependence of steady state creep rates were studied. Stress exponent and the activation energy estimated in the investigation were lower than the reported values of stress exponent and activation energy from standard creep tests. These differences in the values were attributed to the microstructural differences in the specimen material.

Bernard et al. [44] used indentation technique to study creep properties of soda-lime-silica glass using spherical, flat punch and Vickers indenters, at temperatures between 813 and 913 K, with a maximum load of 15 N. Impression creep curves on this material showed a normal behavior, i.e., curves exhibited a primary creep stage and a secondary creep stage. The impression creep curves obtained on this material are shown in Figs. 2.11(a) and (b). The temperature dependence of viscosity was in good agreement with those reported in the literature. They found that the indentation creep method was a very powerful way for studying the viscoelastic behavior of these materials.

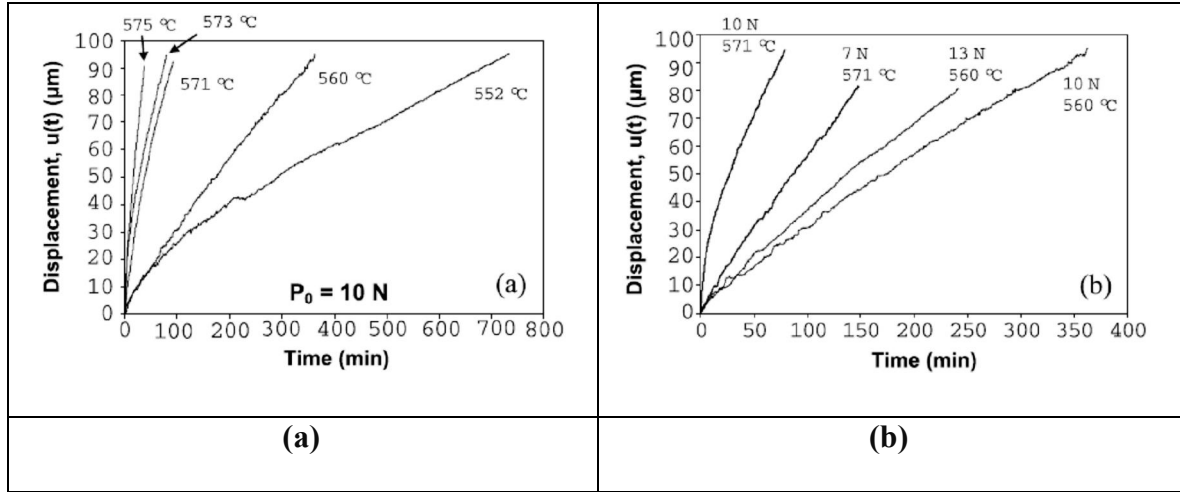


Fig. 2.11 Displacement vs time plots obtained for soda-lime-silica glass using cylindrical flat punch a) influence of temperature and b) influence of load [44].

2.3.4 Polymers

Assessment of creep behavior of polymeric materials is also important as these materials are used for high temperature applications in aerospace and space structures as matrix materials in fibre-reinforced composites. Impression creep technique has been employed for studying creep behavior of polymeric materials also. Chen et al. [45] studied creep behavior of PMR-15 resin (used as matrix in fibre-reinforced composites on aerospace and space structures for high temperature applications) using impression creep technique, in the temperature range of 563-613 K and the punching stress range of 76-381 MPa. The specimen size used was $15 \times 10 \times 4 \text{ mm}^3$. It was found that there existed a steady state creep for the creep tests performed at temperatures of 563 K and higher, from which steady state impression velocity was calculated. The steady state impression velocity increased with increase in temperature and stress, with stress exponent values in the range of 1.5-2.2. The results were found to be consistent with the results obtained from the tensile creep tests.

2.4 Correlation between Impression Creep and Uniaxial Creep

In impression creep test, a constant load (L) is applied to a flat specimen through a flat-ended cylindrical indenter of diameter D . The mean pressure under the punch is referred to as the punching stress (σ_{imp}) which is calculated by dividing the applied load by the area of contact [20]. The rate at which the cylindrical punch penetrates the specimen is referred to as impression velocity (v_{imp}). The punching stress is correlated to the uniaxial applied stress and the ratio of the impression velocity v_{imp} to the punch diameter D is correlated to the steady state creep rate $\dot{\epsilon}_{uni}$ using correlation factors. The general forms of these correlations are,

$$\sigma_{uni} = \alpha \sigma_{imp} \quad (2.2)$$

and,

$$\dot{\epsilon}_{uni} = \frac{v_{imp}}{\beta D} \quad (2.3)$$

where, α and β are the correlation factors.

The punching stress applied in impression creep is higher than the uniaxial stress. This is because of the fact that the impression creep test is essentially a compression test and the plastically deformed zone under the punch is confined within a large volume of the material in the specimen which is either elastic or rigid. Thus, there is no free flow of material. To overcome the resistance offered by this volume of material to the plastic flow, it is required to apply a higher load or stress in order to achieve an equivalent uniaxial stress and hence equivalent steady state creep rate. Empirically, there is a factor, around one third, which converts the punching stress to an equivalent uniaxial stress. This factor is almost equivalent to the constraint factor

which is used to relate the hardness (mean contact pressure) to the uniaxial flow stress of the material proposed by Prandtl [46], Tabor [6] and other researchers [47, 48].

Li and co-workers [19, 20] carried out finite element analysis for materials obeying power-law creep. The impression creep experiment was simulated by considering power law constitutive equation for the deformation of each finite element. It was found that the impression velocity v_{imp} was proportional to the punch diameter and had the same stress dependence as was observed in the conventional uniaxial creep test. The stress conversion factor was found to be 0.3 [49].

Hyde et al. [50] introduced the reference stress method to determine the value of α such that both α and the effective gage factor (a fraction of indenter diameter) are independent of n values. The value of α obtained this way was 0.296 which was comparable to $\alpha = 0.3$, determined by Yu and Li [49]. Based on this α value, the effective gauge length was found to be 0.755 times the indenter diameter.

The values of correlation factors α and β for converting the stress and steady state creep rates from two testing techniques used for various materials are given in Table 2.1.

Table 2.1 Correlation factors for comparison of impression creep test results with corresponding uniaxial creep test results for various materials.

Materials	α	β	References
Pb-Sb alloys	0.33	1	[51]
Al alloys	0.33	1	[27]
Mg-8Zn-4Al-0.5Ca alloys	$1/3.3 \approx 0.303$	1	[52]
Fe ₃ Al based alloys	0.33	1	[53]
Mg-5Sn-xCa	0.33	1	[54]
Mg	0.33	1	[24]
Cd	0.25	1	[23]
Ti-48Al-2V	0.33	1	[55]
Ti Al alloy	0.296	0.755	[56]
316 SS	0.296	0.755	[28]
2-1/4Cr1Mo	0.296	0.755	[35]
AZ91 Mg alloys	0.33	1	[57]
Sn3.5Ag eutectic alloy	0.303	1	[58]
Sn-40Pb-2.5Sb solder alloy	0.33	1	[59]
Solder balls	$1/3.5 \approx 0.286$	1	[60]
AZ91 magnesium alloy	0.3	0.5	[61, 62]
Mg ₆₆ Zn ₆₃ Cu cast alloy	0.33	1	[63]
AZ31 Mg alloy	0.33	1	[64]

2.5. Indenter Geometry and Dimensions

As discussed already, cylindrical indenters with flat end have generally been used in most impression creep experiments. However, as an alternate, Hyde et al. [34, 35, 65,

66] employed rectangular indenter (see Fig. 2.7) to characterize creep properties of mainly heat affected zones in weld joints. The idea of using a long rectangular indenter was to ensure that the contact area between the indenter and test material is relatively large compared to microstructural feature (e.g., grain size) in order to obtain the characteristic bulk properties of materials. However, this purpose can be achieved with flat-ended cylindrical indenters also by suitably selecting the diameter of the cylindrical flat punch according to the microstructural features such as grain size or the width of heat affected zones in weld joints.

The flat-ended cylindrical indenters having various diameters have been used for impression creep tests by various researchers. The diameter of the indenters range from 0.1 mm [67] to 2 mm depending on the applications [68, 69].

2.6 Plastic Zone in Impression Creep

Yu and Li [20] studied the dislocation structure under the punch in LiF single crystal after impression creep test using etch-pits technique. The dislocation etch-pits were examined under the optical microscope. The test was carried out at 973 K under punching stress of 4.3 MPa, using indenter of diameter 1.18 mm. The highest dislocation density was observed near the indentation. The dislocation structure as revealed by etch-pits indicated that the depth of the plastic zone was about the diameter of the punch. Juhasz et al. [27] also observed the plastic zone size to be of the order of diameter of the indenter (indenter diameter used was 1 mm) in impression creep of fine grained Al alloys tested in the temperature range 723-823 K. However, there is no detailed analysis of different microstructural zone in the vicinity of the indentation discussed in these papers.

Butt et al. [69] examined the plastic zone in SiC particle-MoSi₂ composite specimen after impression creep test. They observed a hydrostatic zone below the indentation. This zone was observed to be surrounded by the deviatoric stress region (Fig. 2.12). Similar observation of hydrostatic zone immediately under the indentation was also reported by Mahmudi and co workers in cast magnesium alloy [57].

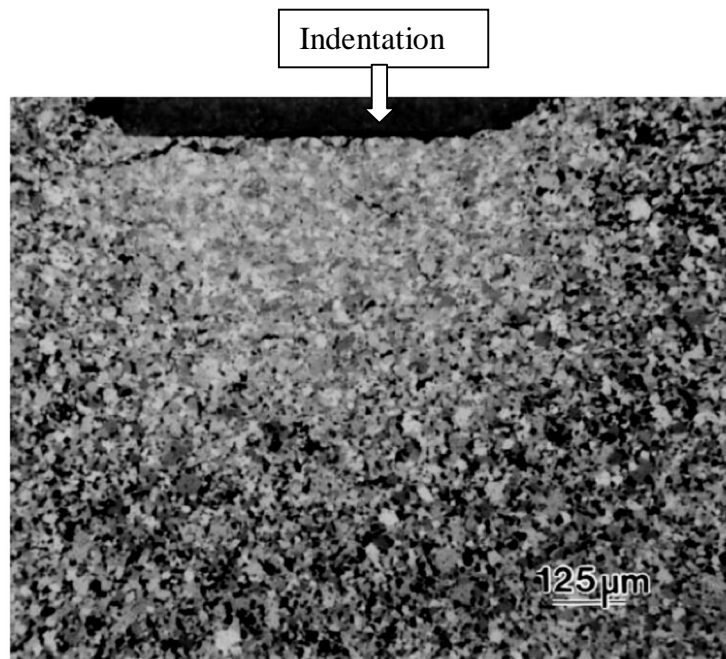


Fig. 2.12 Optical micrograph of the deformation region observed by Butt et al. [69] in SiC particle-MoSi₂ composite specimen.

Dorner et al. [56] studied deformation under the indentation in TiAl alloy after impression creep tests. The study revealed line patterns as shown in the Fig. 2.13. These line patterns were supposed to be associated with the material flow during indentation.

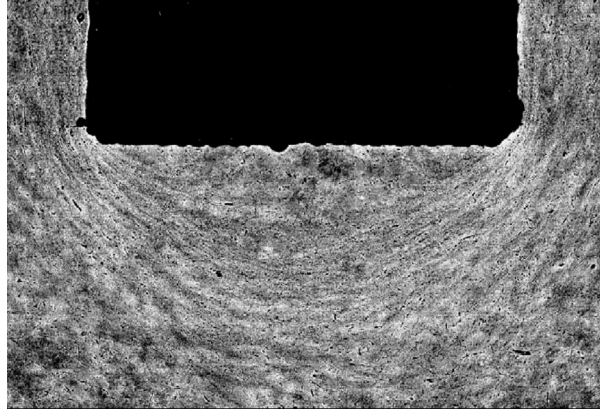


Fig. 2.13 Scanning Electron Micrograph showing deformation under the punch in TiAl alloy reported by Dorner et al. [56].

2.7 Finite Element Analysis

Li and co-workers [19, 20] carried out finite element analysis of impression creep for succinonitrile crystals in the power-law creep regime. The FE model was an axis-symmetric model consisting of 186 elements. The impression creep experiment was simulated by considering power law constitutive equation for the deformation of each finite element. This power law was between the creep rate and the Von Mises stress. The Von Mises flow rule was used to calculate the various strain components. The validity of the FE model was analyzed by comparing elastic stress field under the punch obtained from their FE analysis with the theoretical solutions for elastic stress field for semi-infinite medium given by Terazawa [70] and Harding and Sneddon [71]. A good agreement between the FEA and theoretical results was obtained. The FE analysis established a power law between in the steady state impression velocity and punching stress. This relationship between the steady state impression velocity and the punching stress was,

$$v_{imp} = 2Aa \left(\frac{\sigma_{imp}}{m} \right)^n \quad (2.4)$$

where v_{imp} is the steady state impression velocity, A is material constant, a is the radius of the cylindrical flat punch, σ_{imp} is punching stress, m is the stress conversion factor, and n is power law exponent. The stress conversion factor m was found to be 0.3 [49]. They also studied the Von Mises stress distribution under the punch. It was found that the maximum Von Mises Stress was not located in the region immediately under the punch-specimen contact but at a distance away from it approximately equal to the radius of the punch.

Hyde et al. [50] repeated the finite element calculations of Yu and Li [20] for the power law material. They introduced the reference stress method, to determine the value of α such that both α and the effective gage factor (a fraction of indenter diameter) were independent of n values. The α value obtained this way was 0.296. This was comparable to the $\alpha = 0.3$, determined by Yu and Li [20, 49]. Based on this α value, the effective gauge length was found to be 0.755 times the indenter diameter.

Lu et al. [72] carried out finite element analysis of spherical and cylindrical indentation for determining the plastic properties (yield strength) of a compression moulded high impact polystyrene and cast aluminium. FE simulations were primarily used for investigating the load-depth responses of the material. The indenter was assumed to be rigid. For simulation, a vertical displacement was applied to the rigid indenter and resultant reaction force was calculated to study the load-displacement response of the materials. The plasticity was modelled by the Von Mises flow criterion given in ABAQUS [73]. The FE model was validated for the elastic deformation described by classical Hertz solution for spherical indentation [74] and Sneddon's solution for elastic deformation with flat-ended cylindrical indentation [75]. The elastic

stress field under the punch which was studied analytically by Sneddon [76] was also studied from their FE analysis in cast Al material. It was found that the analytical solution agreed well with the FEA results in their study. The study of Von Mises stress distribution under the punch revealed that the maximum value of Von Mises stress at the edge of the indentation was approximately $0.78 P_m$, where P_m is the mean contact pressure which is obtained by dividing the applied load by the indenter-specimen contact area. The study of equivalent plastic strain revealed that the size of the plastic zone was approximately twice the indenter diameter. It was also observed that the material directly underneath the indenter showed no or little plastic deformation during indentation. The material pile-up was also observed. However, detailed analyses of deformation which involve the material displacement and pile-up mechanism were not studied.

References:

-
- [1] A. C. Fischer-Cripps, "Introduction to Contact Mechanics" Springer, 2000.
 - [2] D. Tabor, The hardness of solids, Surface Physics, Cavendish Laboratory, Cambridge, 145-179.
 - [3] A. Wahlberg, "Brinell's method of determining hardness", J. Iron Steel Inst. London, 59, (1901)243-298.
 - [4] R. L. Smith and G. E. Sandland, Proc. Inst. Mech. Eng., 1(1922) 623-641.
 - [5] L. Prandtl: "Über die Eindringungsfestigkeit (Harte) Plastischer Baustoffe und die Festigkeit von Schneiden, Z. Angew. Math. Mech., 1(1921), 15620.
 - [6] D. Tabor, Proc. R. Soc. London. A 192 (1948) 247-274.
 - [7] F. M. Haggag, R. K. Nanstad, J. T. Hutton, D. L. Thomas, and R. L. Swain, American Society for Testing and Materials, Philadelphia, (1990) 188-208.

-
- [8] K. L. Murty, M. D. Mathew, Nucl. Eng. Design, 228 (2004) 81696.
- [9] T.O. Mulhearn and D.Tabor, J. Inst. Met., 7 (1960) 89-93.
- [10] O. D. Sherby and P.E. Armstrong, Met. Trans., 2 (1971) 3479-3484.
- [11] P. M. Sargent and M. F. Ashby, Mater. Sci. Technol., 8 (1992) 594-601.
- [12] H. D. Merchant, G. S. Murty, S. N. Bahadur, L. T. Dwivedi and Y. Mehrotra, J. Mater. Sci., 8 (1973) 437-442.
- [13] R. M. Hooper and C. A. Brookes, J. Mater. Sci., 19 (1984) 4057-4060.
- [14] G. Cseh, N. Q. Chinh, P. Tasnadi and A. Juhasz, J. Mater. Sci., 32 (1997) 5107-5111.
- [15] G. Cseh, N. Q. Chinh and A. Juhasz, J. Mater. Sci., 17 (1998) 1207-1209.
- [16] M. Fujiwara and M. Otsuka, Mater. Sci. Eng. A., 319-321 (2001) 929-933.
- [17] U. K. Viswanathan, T. R. G. Kutty, R. Keswani and C. Ganguly, J. Mater. Sci., 31 (1996) 2705-2709.
- [18] B. N. Lucas and W. C. Oliver, Metall. Mater. Trans. A., 30A (1999) 601-610.
- [19] S. N. Chu and J. C. M. Li, J. Mater. Sci., 12(1977), 2200-2208.
- [20] E. C. Yu and J. C. M. Li, Philos. Mag., 36(4) (1977) 811-825
- [21] S. N.G Chu and J. C. M. Li, J. Mater. Sci. Eng., 39 (1979) 1-10.
- [22] F. Yang and J.C.M. Li, Mater. Sci. Eng. R 74 (2013) 233-253.
- [23] G. S. Murty and D. H. Sastry, Trans. Indian Inst. Met., 34 (1981) 195-201
- [24] D. H Sastry, Mater. Sci. Eng. A., 409 (2005) 67-75.
- [25] G. S. Murty and D. H Sastry, Phys. Stat. Sol. (a), 70 (1982) 63-71.
- [26] P.S. Godavarti, K.L. Murty, J. Mater. Sci. Lett., 6 (1987) 4566458.
- [27] A. Juhasz, N.Q. Chinh, P. Tasnadi, P. Szaszvari and I. Kovacs, Mater. Sci. Forum, 13-14(1987) 421-428.
- [28] T. H. Hyde, K.A. Yehia and A.A. Becker, Mater. High Temp., 13 (1995) 1336138.

-
- [29] T. H. Hyde, High Temp. Technol., 6 (1988) 51-61.
 - [30] T. R. G. Kutty, C.B. Basak, A. Kumar and H.S. Kamath, J. Nucl. Mat., 408 (2011) 90-95.
 - [31] W. S. Gibbs, S. H. Wang, D. K. Matlock and D. L. Olson, Welding Res. Suppl., (1985) 153-158.
 - [32] S. H. Wang, J. Mar. Sci. Technol., 2(1) (1994) 17-24.
 - [33] H.Y. Yu, M.A. Imam and B.B. Rath, Welding Journal, 64 (1985) 55s-65s.
 - [34] T. H. Hyde and W. Sun, Int. J. Pressure Vessels and Piping, 86 (2009) 757-763.
 - [35] T.H. Hyde and W. Sun, J. Strain Analysis, 44 (2009) 171-185.
 - [36] T. H. Hyde, W. Sun and J.A. Williams, Mater. High Temp. 16 (1999) 117-129.
 - [37] W. Sun, T. H. Hyde, Acta. Metall. Sin., 12 (1999) 68-76.
 - [38] M.A. Lisin, I. D. Choi, D. K. Matlock and D. L. Olson, Weld. J., 69 (1990) 159s-165s.
 - [39] H. Udaya Prasanna and K. Rajendra Udupa, Nucl. Eng. Design., 241 (2011) 4938-4943.
 - [40] A. K. Mondal and S. Kumar, Composite Sci. Technol., 69(2009) 1592-1598.
 - [41] G. Cseh, J. Bar, H. J. Gudladt, J. Lendvai and A. Juhasz, Mater. Sci. Eng. A., 272 (1999) 145-151.
 - [42] N.Q. Chinh, P. Tasnadi, A. Juhasz, P. Szommer, E. Szep-Kiss and I. Kovacs, Key Eng. Mater., 97-98 (1994) 159-167.
 - [43] F. Dorcaková, V. Jan, L. Hegedusov and J. Dusza, Key. Eng. Mater., 333 (2007) 281-284.
 - [44] C. Bernard, V. Keryvin, J. C. Sangleboeuf and T. Rouxel, Mech. Mater., 42 (2010) 196-206.

-
- [45] R. Chen, Y.C. Lu, F. Yang, G.P. Tandon, and G.A. Schoeppner, *Poly. Eng. Sci.*, (2009)1-5.
- [46] L. Prandtl: „U“ber die Eindringungsfestigkeit (Harte) Plastischer Baustoffe und Die Festigkeit von Schneiden, *Z. Angew. Math. Mech.*, 1(1921), 15620.
- [47] A. G Atkins and D. Tabor, *J. Mech. Phys. Solids*, 13 (1965) 149-164.
- [48] K. L. Johnson, *J. Mech. Phys. Solids.*, 18 (1970) 115-126.
- [49] J. C. M. Li, *Mater. Sci. Eng. A.*, 322 (2002) 23-42.
- [50] T. H. Hyde, K. A. Yehia and A. A. Becker, *Int. J. Mech. Sci.*, 35 (1993) 451-462.
- [51] R. Mahmudi, A. R. Geranmayeh and A. Razaee-Bazzaz, *J. Alloys. Comp.*, 427(2007) 124-129.
- [52] L. Peng, F. Yang, J. Feng Nie and J. C. M Li, *Mater. Sci. Eng. A* 410-411 (2005) 42-47.
- [53] R. S. Sundar and D. H Sastry, *Intermetallics*, 8 (2000) 1061-1065.
- [54] G. Nayyeri and R. Mahmudi, *Mat. Sci. Engg. A.*, 527(2010) 2087-2098.
- [55] M. Sujata, D. H. Sastry and C. Ramachandra, *Intermetallics.*, 12 (2004) 691-697.
- [56] D. Dorner, K. Roller, B. Skrotzki, B. Stockhert and G. Eggeler, *Mater. Sci. Eng. A.*, 357 (2003) 346-354.
- [57] F. Kabirian and R. Mahmudi, *Metal. Mater. Trans. A.*, 40 (2009) 116- 127.
- [58] F. Yang and L. Peng, *Mat. Sci. Eng. A.*, 409 (2005) 87-92.
- [59] R. Mahmudi, A. R. Bazzaz and H. R. Banaie-Fard, *J. Alloys. Comp.*, 429 (2007) 192-197.
- [60] D. Pan, R. A. Marks, I. Dutta, R. Mahajan and S.G. Jadhav, *Rev. Sci. Instrum.*, 75 (2004) 5244-5252.
- [61] B. Nami, H. Razavi, S. M. Miresmaeili, Sh. Mirdamadic and S.G. Shabestari, *Scr. Mater.*, 65 (2011) 221-224.

-
- [62] B. Nami, H. Razavi, S. Mirdamadi, S.G. Shabestari, S.M. Miresmaeili, *Metall. Mater. Trans. A* 41 (2010)1973-1982.
- [63] S. Golmakaniyoon and R. Mahmudi, *Mater. Sci. Eng A.*, 528 (2011) 1668-1677.
- [64] Sh. Ansary, R. Mahmudi, M. J. Esfandyarpour, *Mater. Sci. Eng A.*, 556 (2012) 9-14.
- [65] T. H. Hyde, W. Sun and A.A. Becker, *Int. J. Mech. Sci.*, 38 (1996) 1089-1102.
- [66] W. Sun, T.H. Hyde and S. J. Brett, *J. Mater. Des. Appl., Proc. I Mech. E.*, 222 (2008) 175-181.
- [67] C. Park, X. Long, S. Haberman, S. Ma, I. Dutta, R. Mahajan and S.G. Jadhav, *J. Mater. Sci.*, 42 (2007) 5182-5187.
- [68] D. Chiang and J.C.M. Li, *J. Mater. Res.*, 9(1994) 903-908.
- [69] D. P. Butt, D. A. Korzekwa, S. A. Maloy, H. Kung and J. J. Petrovic, *J. Mater. Res.*, 11 (6) (1996) 1528-1536.
- [70] K. Terazawa, *J. Coll. Sci. Imperial. U. Tokyo*, 37 (1916) Art. 7
- [71] J. W. Harding and I. N. Sneddon, *Proc. Cambridge Phil. Soc.*, 41 (1945) 16
- [72] Y. C. Lu, S. N. V. R. K. Kurapati and F. Yang, *J. Phys. D: Appl. Phys.*, 41 (2008) 115415, 1-8.
- [73] ABAQUS 2007, ABAQUS Usersø Manual (Pawtucket, RI: Habbitt, Karlson and Sorenson Inc.)
- [74] H. Hertz, *Miscellaneous Papers* (Eds: Hertz et al.) London: Macmillan.
- [75] I. N. Sneddon, *Int. J. Eng. Sci.*, 3 (1965) 47-57.
- [76] I. N. Sneddon, *Proc. Cam. Philos. Soc.*, 42 (1946) 29-39.

CHAPTER 3

Experimental Details: Impression Creep Testing System, Materials and Characterization Techniques

3.1 Introduction

This chapter describes the impression creep testing system which is developed at IGCAR. The materials used in the present investigation and their chemical compositions are detailed. The specimen preparation techniques for the impression creep tests are explained. The chapter also describes the material characterization studies carried out before and after impression creep testing to study the initial microstructure of the materials and to analyze plastic deformation zone associated with impression creep, respectively. The characterization techniques which include optical microscope, scanning electron microscope, transmission electron microscope, microhardness, optical profilometer employed for the aforementioned investigations, the specimen preparation techniques for these investigations and its analysis procedures are described.

3.2 Impression Creep Testing System

A unique impression creep testing facility has been developed at IGCAR, and it consists of two identical machines which are shown in Fig.3.1. Schematic of the impression creep machine with details is shown in Fig.3.2.



Fig. 3.1 Impression creep testing facility established at IGCAR.

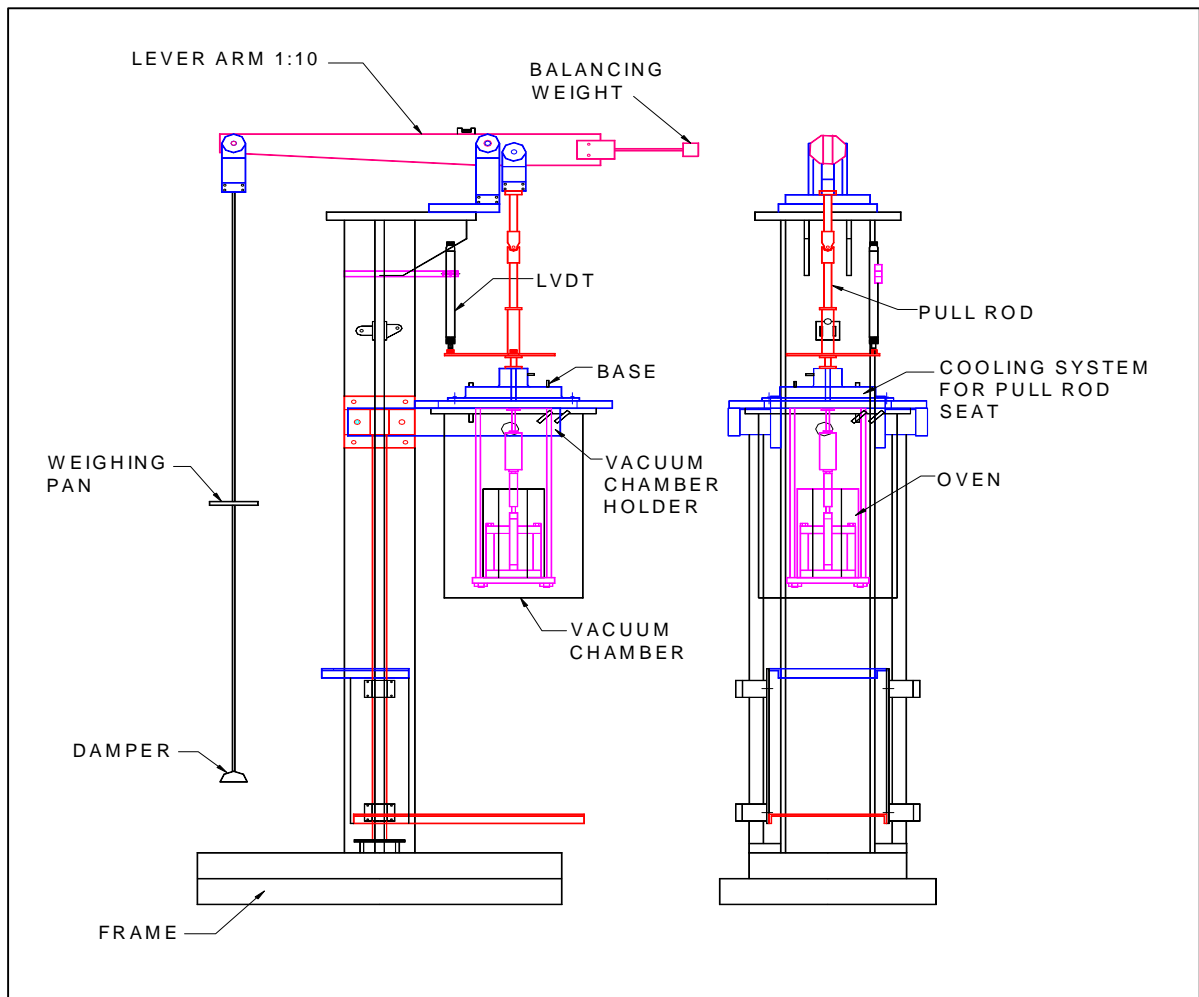


Fig. 3.2 Schematic diagram showing different parts of the impression creep testing machine.

The impression creep testing system comprises of the following main components.

1. Vacuum Chamber
2. Furnace
3. Indenter- Specimen Cage
4. Indenters
5. Displacement Measurement System
6. Loading Mechanism
7. Vacuum System
8. Control Unit
9. Water Cooling System
10. Data Acquisition System

The features and functions of these components are described below.

3.2.1 Vacuum Chamber

The vacuum chamber (shown in Fig. 3.2 and 3.1) is made of stainless steel with a flange for vacuum sealing (gasket). This chamber is mounted on a rectangular plate which can be moved vertically for lowering and raising the chamber. Copper tubes are mounted on the outer surface of the vacuum chamber for circulating water for the purpose of protecting o-rings during high temperature tests.

3.2.2 Furnace

Inside the vacuum chamber is located a cylindrical type furnace which is shown in Fig. 3.3. The furnace can operate upto 800 °C. The temperature controller which is connected to the furnace is capable of maintaining the temperature on the specimen

constant with an accuracy of $\pm 1^{\circ}\text{C}$. The temperature controller used here is a Proportional-Integral-Derivative (PID) controller which are commonly used in uniaxial creep testing machines. The K-type thermocouple was used to measure the specimen temperature by just touching the specimen.

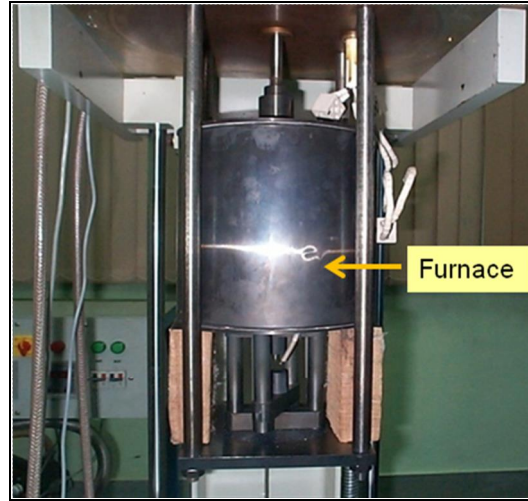


Fig. 3.3 Furnace inside the vacuum chamber.

3.2.3 Indenter- Specimen Cage

The indenter-specimen cage is situated inside the furnace. It consists of two rigid frames, one fixed to the bottom plate of the specimen cage and the other connected to the pull rod which is free to move vertically along with the pull rod. These two frames are indicated as the Frame-1 and Frame-2 as shown in Fig. 3.4. The Frame-1 has an indenter holder to which the indenter is fixed and the Frame-2 has a sample holder over which the test specimen is mounted exactly below the indenter.

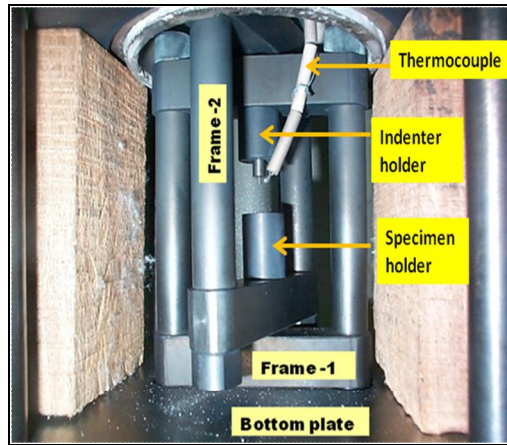


Fig. 3.4 A view of the specimen cage situated inside the furnace.

3.2.4 Indenters

The flat-ended cylindrical indenters are made of tungsten carbide and have typically 1 mm diameter. In the present study, flat-ended cylindrical indenters having diameter 1 mm were used. However, one can use indenters of different diameters (1mm, 1.5mm, 2 mm or 2.5 mm) depending on the requirement for the tests. The indenters with different diameters are shown in Fig. 3.5.



Fig. 3.5 Tungsten carbide indenters of different diameters.

3.2.5 Displacement Measurement System

The depth of penetration of the indenter into the specimen is measured by the vertical displacement of the pull rod through a Linear Variable Differential Transducer (LVDT). The LVDT is rested on the horizontal bar which moves along with the pull rod. The arrangement of the LVDT system for measurement of the indenter displacement is shown in Fig. 3.6. The accuracy of the LVDT is $\pm 0.5\%$ or better. The resolution of the LVDT is $1\ \mu\text{m}$.

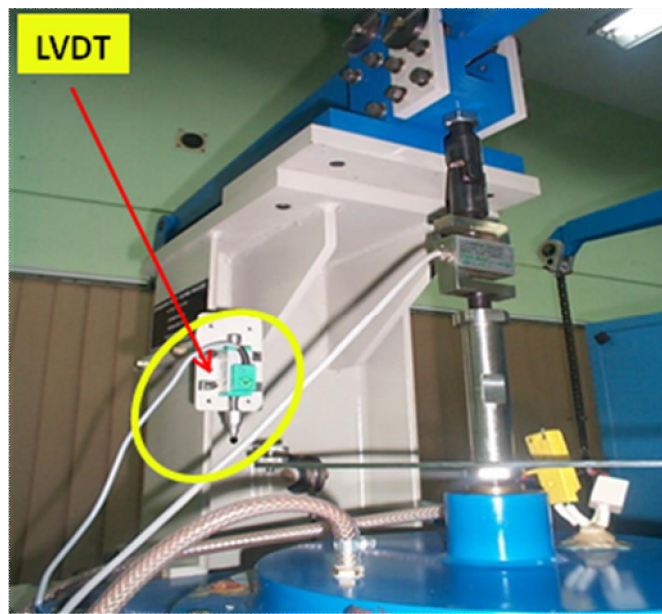


Fig. 3.6 The LVDT set up for displacement/depth measurement.

3.2.6 Loading Mechanism

The system consists of a lever arm with lever ratio 1:10. Loading is manual and applied on the loading pan (see Fig. 3.2). A load cell of maximum capacity of 1 kN load is attached to the load train to measure the load applied on the specimen.

3.2.7 Vacuum System

Vacuum system connected to the impression creep machine consists of a rotary pump and a diffusion pump which are shown in Fig. 3.7. The vacuum system can produce a vacuum level upto 10^{-6} mbar. Tests are done under vacuum in order to avoid oxidation of the specimen at higher test temperatures.

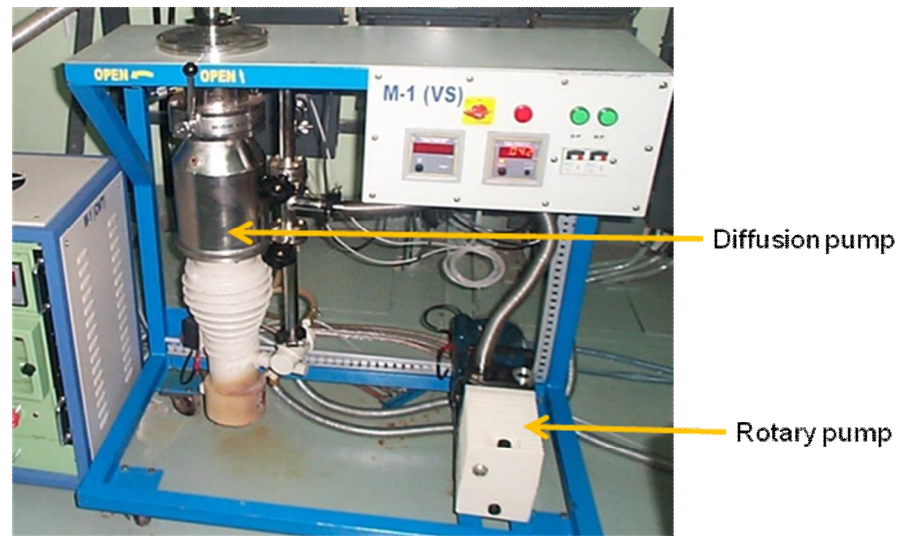


Fig. 3.7 Vacuum system incorporated with the impression creep testing system.

3.2.8 Control System

Figure 3.8 shows the control unit which is connected to the impression creep machine. It consists of a temperature controller, a timer, load cell reading display and LVDT reading display.

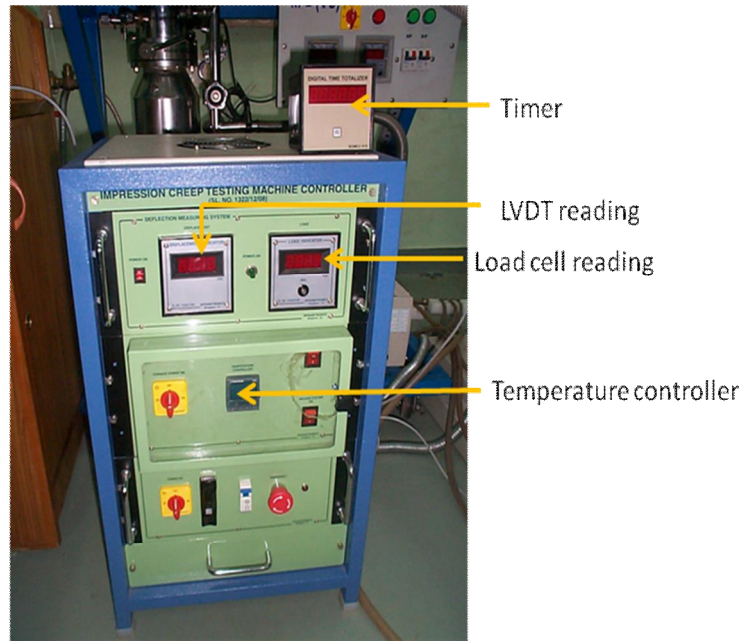


Fig. 3.8 Impression creep machine control unit.

3.2.9 Cooling System

In order to protect the vacuum sealing or rubber o-rings during high temperature tests, copper tubes are provided at the outer surface of the vacuum chamber and near the vacuum sealing to circulate water continuously during the test. Each impression creep machine is provided with a separate water inlet connection with a common outlet value. An electric pump is used for pumping water through pipes.

3.2.10 Data Acquisition System

Impression creep testing system is incorporated with a PC- based online data acquisition system to record the data continuously during the test. Data is typically acquired for every 300 sec. However, this time interval can be adjusted in the data acquisition system depending on the requirement.

The technical specifications of the impression creep testing system are briefly summarized in table 3.1.

Table 3.1 Technical specifications of the impression creep testing system.

Load capacity	980 N
Loading arrangement	Liver arm; ratio 1:10
Temperature range	800 °C maximum
Temperature sensor	K-type thermocouple
Vacuum level	Vacuum of 10^{-6} mbar using diffusion pump and rotary pump combination
Displacement measurement	LVDT; 0-2.5 mm; accuracy better than $\pm 0.5\%$
Data processing	PC based online Data Acquisition System
Indenter material	Tungsten carbide
Indenter dimensions	1.0, 1.5, 2.0 and 2.5 mm diameter

3.3 Materials and Specimens

3.3.1 316LN SS

In the present investigation, four heats of 316LN SS containing 0.07, 0.11, 0.14, and 0.22 wt.% nitrogen were used. The chemical compositions of the four heats of 316LN SS are given in Table 3.2.

Table 3.2 Chemical composition (in wt. %) of type 316LN SS.

Designation	Chemical composition (in wt. %)									
	N	C	Mn	Cr	Mo	Ni	Si	S	P	Fe
7N	0.07	0.027	1.7	17.53	2.49	12.2	0.22	0.0055	0.013	Bal.
11N	0.11	0.033	1.78	17.62	2.51	12.27	0.21	0.0055	0.015	Bal.
14N	0.14	0.025	1.74	17.57	2.53	12.15	0.2	0.0041	0.017	Bal.
22N	0.22	0.028	1.7	17.57	2.54	12.36	0.2	0.0055	0.018	Bal.

3.3.1.1 Specimen Preparation

Rectangular strips of 22 x 22 mm cross-section were cut from the 316LN SS plates in the rolling direction. From these strips, rectangular blocks of each 12 mm thickness were cut and machined to get the flat surfaces using a surface grinding machine. The perpendicularity between the faces of the specimen was less than 0.008° . The impression creep testing surfaces of the specimens were polished upto 1 μm diamond finish. Care was taken to maintain the parallelism of the surfaces while polishing the surface manually. Before diamond polishing, the specimen was solution treated at 1373 K for 1 hour followed by water quenching. Process of solution treatment was carried out by keeping the specimen inside a vacuum sealed glass tube. The final dimension of the specimens used for the impression creep tests were 20 mm x 20 mm x 10 mm. Figure 3.9 shows the typical impression creep test specimen employed in the present investigation.

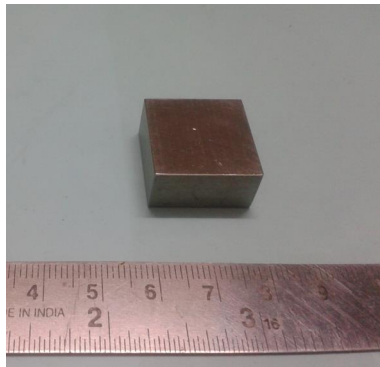


Fig. 3.9 Typical impression creep test specimen employed in the present investigation.

3.3.2 316LN SS Weld Joint

316LN SS weld pad of dimension 500 mm x 250 mm x 23 mm was prepared by employing manual metal arc welding process using 316(N) SS electrode. The details of the weld pad preparation are given in Table 3.3. The chemical compositions of 316LN

SS base metal and 316(N) SS consumable electrode are given in Table 3.4. The weld pad was subjected to radiographic examination and the region of weld defects, if any was avoided while selecting test specimens.

Table 3.3 Details of preparation of the weld pad.

Welding Process	Manual Metal Arc
Joint Design	Single V groove
Number of passes	32
Inter-pass temperature	423 K
Flux	Basic coated
Current	150 A
Voltage	25 V
Travel speed	3 mm/s

Table 3.4 Chemical composition (in wt. %) of the 316LN SS weld joint.

	Chemical composition (in wt. %)								
	C	Ni	Cr	Mo	Mn	Si	S	P	N
316 LN SS base metal	0.025	12.15	17.57	2.53	1.74	0.2	0.0041	0.017	0.14
316 (N) SS weld metal	0.052	11.5	18.6	2.2	1.74	0.64	0.007	0.022	0.067

3.3.2.1 Specimen Preparation

Rectangular blocks of width 15 mm were cut from the weld pad of thickness 23 mm. The cross sectional surface of the weld joints were polished up to 1 μm finish using standard metallographic techniques. The 316LN SS weld joint used in the present investigation is shown in Fig. 3.10.



Fig. 3.10 The cross section of the 316LN SS weld joint on which impression creep tests were conducted.

3.4 Materials Characterization—Before and After Impression Creep Tests

3.4.1 Initial Microstructures of the 316LN SS and Its Weld Joints

Initial microstructure of the 316LN SS containing 0.07, 0.11, 0.14 and 0.22 wt. % nitrogen and that of heat-affected zone, the weld metal and the base metal of the 316LN SS weld joint was studied using a Olympus GX51 model optical microscope.

Specimen surfaces were polished with 1 μm diamond paste using standard metallographic techniques. Electrolytic etching was carried out using 60 % nitric acid in distilled water (60 ml HNO_3 + 40 ml H_2O) to reveal the microstructures. Grain size measurements of 316LN SS containing 0.07, 0.11, 0.14 and 0.22 wt. % nitrogen were

performed by linear intercept method based on the ASTM standard. The average grain size of the materials was found to be 85 μm . Initial microstructures of the 316LN SS containing 0.07, 0.11, 0.14 and 0.22 wt. % nitrogen were also observed from the EBSD analysis.

3.4.2 Characterization of the Plastic Zone in Impression Creep

3.4.2.1 Microstructural Characterization

3.4.2.1.1 Optical Microscopy

In order to characterize the microstructural changes in the vicinity of the impressions, the specimens were sectioned just outside of the indentation using a low speed diamond saw and the sectioned surface was carefully ground and polished such that the final polished surface passed through the impression. The schematic illustration of the sectioning of the tested specimen is given in Fig. 3.11. The final polishing was carried out using 1 μm diamond paste. The polished samples were etched electrolytically with 60 % nitric acid in distilled water (60 ml HNO_3 + 40 ml H_2O). Microstructures were examined in an optical microscope of model Olympus GX51.

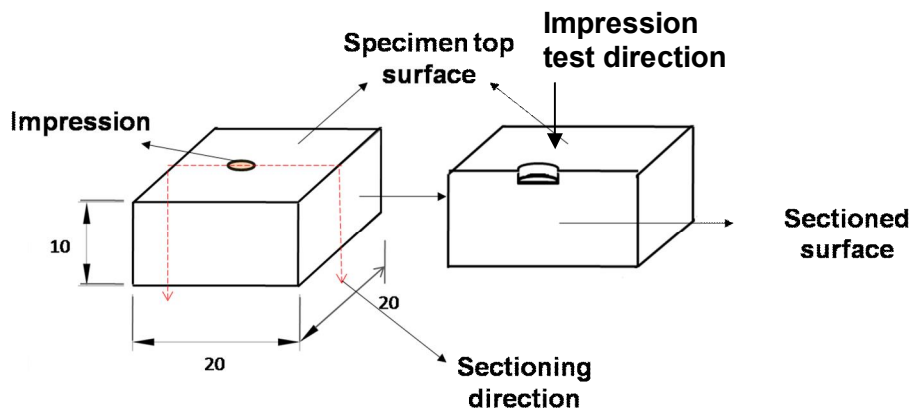


Fig. 3.11 Schematic illustration of sectioning of the tested specimen for cross-sectional microstructural analysis (for optical, SEM and EBSD).

3.4.2.1.2 Scanning Electron Microscopy

Extent of material deformation in the vicinity of the impression at higher magnifications was studied using a SUPRA 55 FE-SEM. Specimen preparation for this analysis was same as mentioned for optical microscopy analysis.

3.4.2.1.3 Electron Back-Scattered Diffraction Analysis

Electron Backscattered Diffraction Analysis was carried out on the impression creep tested specimens in order to identify the crystallographic planes participating in the deformation process and analyze the plastic zone around the indentation. Impression creep tested specimen was sectioned along the diameter of the impression using an electrodischarge wire-cut machine. Sectioning of the specimen was done as illustrated in Fig. 3.11. The sectioned surface (see Fig. 3.11) was ground and polished mechanically using SiC abrasive papers (80, 120, 320, 400, 600, 800, 1000, 1200). The surface was further polished upto 0.25 μm using diamond paste. The final polishing was performed using colloidal silica of size 50 nm. The polished specimen was ultrasonically cleaned in methanol and dried before examining under the microscope.

SUPRA 55 FE-SEM equipped with electron backscattered diffraction detector (EBSD) was used to analyse the impression creep tested specimens. An accelerating voltage of 20 kV, an aperture of 120 μm , a working distance of 16 mm, a tilt angle of 70°, sample-detector distance 178 mm and an indexing algorithm based on eight detected bands was utilized. A magnification of 500X and a scan step size of 5 μm (square grids) required a scan time of ~2 hours. Aztec software was used for data collection and HKL-Channel 5TM software was used for post processing of the data.

3.4.2.1.4 Transmission Electron Microscopy

With an aim to study the substructural evolution endured in the highly deformed region under the indentation, TEM studies were carried out. In order to identify the deformed location from which the section for TEM specimen is to be extracted, the deformed zone under the indentation was first observed using optical microscope. This was carried out as follows. The specimen was sectioned outside the impression using a low speed diamond saw in the direction as shown in Fig. 3.12(a). The sectioned surface was ground and polished upto 1 μ m diamond finish such that the final polished surface reached the impression. The polished surface was etched electrolytically with 60 % nitric acid in distilled water. The deformed zone under the indentation was then examined in an optical microscope. The region which experienced maximum deformation was marked and a thin rectangular section was cut from this region using low speed diamond saw such that the region of interest was within the rectangular section as shown schematically in Fig. 3.12 (b) (Deformation regions under the indentation are discussed in chapter 4).

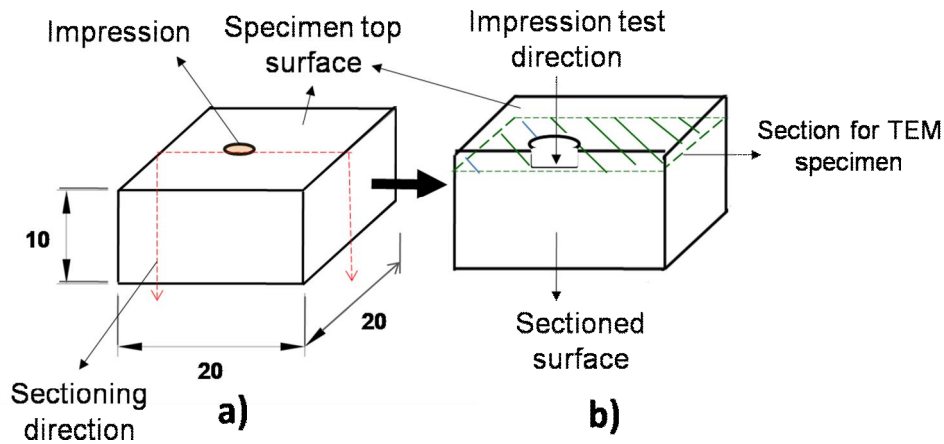


Fig. 3.12 Schematic diagram showing a) sectioning of the impression creep tested specimen and b) region from which a rectangular section was cut for TEM specimen.

TEM specimen preparation from the rectangular section was carried out as follows. First, the rectangular section was ground and polished mechanically using SiC abrasive papers (80, 120, 320, 400, 600, 800, 1000, 1200, 1400), thinned down to a foil of 80 μm thickness. A disc 3mm diameter was then punched from this foil such that the 3 mm TEM disc contained the region exactly below the indentation. The TEM specimen was ultrasonically cleaned in methanol and electropolished using a solution of 10% perchloric acid in methanol using Struers Tenupol-5 twin jet polisher. The cell potential was maintained at 10 V and the bath temperature was maintained at $-40\pm 2^\circ\text{C}$. After polishing, the specimen in the holder was immediately rinsed in methanol and then dried. Samples were examined using a Phillips CM200 ATEM (200 kV) transmission electron microscope.

3.4.2.2 Microhardness

In order to study the size and the shape of the plastic zone associated with impression creep, a series of microhardness profiles were taken on the sectioned surface along different lines and directions in the specimens as shown schematically in Fig. 3.13. A Microhardness tester of model HMV-2 with a Vickers scale was used. A Load of 100 g was applied for 10 seconds on each microindentation. For microhardness measurements, the surfaces were fine polished upto 1 μm using diamond paste. Microhardness measurements were also made on the 316LN SS weld joint to study the variation of hardness across the fusion line along the weld metal, heat-affected zone and the base metal. For this case, a constant load of 200 g was applied for 15 seconds.

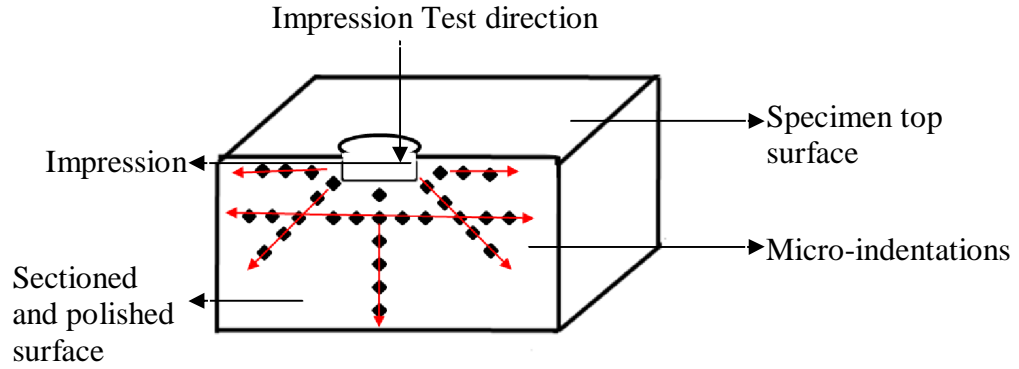


Fig. 3.13 Schematic diagram illustrating the microhardness measurements made around the impressions on the sectioned surface of the specimen.

3.4.2.3 Optical Profilometry

Optical profilometry is a non-contact interferometric-based method for characterizing surface topography. In the present study, an optical profilometer, Talysurf CLI-1000 model, was used to examine the indentation surface profile in the impression creep tested specimen.

CHAPTER 4

Impression Creep Behavior of 316LN Stainless Steel

4.1 Introduction

In the preceding chapter, the impression creep testing system which is developed at IGCAR has been discussed. One of the potential applications of the impression creep technique is in the development of creep resistant alloys for rapid screening of creep properties of laboratory heats of materials. The present chapter demonstrates the usefulness of impression creep technique as applicable to alloy development studies of a creep resistant austenitic stainless steel (316LN SS) which has been employed as structural material for Prototype Fast Breeder Reactor at Kalpakkam. In view of establishing the technique and understanding the impression creep behavior of austenitic stainless steels, a systematic study of creep deformation behavior of 316LN SS using this technique has been undertaken. Impression creep tests were carried out on 316LN SS containing different nitrogen contents, at different stress levels and temperatures. Chapter details the analysis of impression creep test parameters and its correlation with the conventional uniaxial creep test parameters. Chapter discusses the impression creep test results on 316LN SS and its comparison with the uniaxial creep test results on the similar materials. The extensive studies on the characteristics of the plastic zone in impression creep, which is one of the key areas which is not well understood so far, have been carried out and the results are discussed.

4.2 Equivalence between Impression Creep and Uniaxial Creep in 316LN SS

Impression creep process, as illustrated in Chapter 1, can be defined as the time dependent penetration of the cylindrical flat punch into the specimen material under a constant load at elevated temperature. Penetration of the punch into the test specimen is guided by the time dependent displacement of the material under the punch which can be regarded as time dependent plastic deformation of the material beneath the indenter. Thus, impression creep technique essentially determines the creep behavior of materials. The following sections describe the analysis of the impression creep parameters and its correlation with uniaxial creep parameters in 316LN SS.

4.2.1 Analysis of Impression Creep Test Parameters

There are two important parameters involved in impression creep. One is the punching stress and other is the impression velocity.

4.2.1.1 Punching Stress

In impression creep test, a constant load L is applied to the test specimen through a cylindrical punch of diameter D . The mean pressure under the punch which is referred to as the punching stress is evaluated as,

$$\sigma_{imp} = \frac{4L}{\pi D^2} \quad (4.1)$$

4.2.1.2 Impression Velocity

Under the punching stress σ_{imp} , the cylindrical punch penetrates into the surface of the test specimen to a depth h in time t . The rate at which the cylindrical punch penetrates the specimen surface is referred to as impression velocity and is given by,

$$v_{imp} = \frac{dh}{dt} \quad (4.2)$$

4.2.2 Correlation between Impression Creep and Uniaxial Creep Test Parameters

The ratio of impression velocity v_{imp} to the punch diameter D in the impression creep test is correlated to the steady state creep rate $\dot{\varepsilon}_{uni}$ in uniaxial creep test. Similarly, the punching stress σ_{imp} is correlated to an equivalent uniaxial stress σ_{uni} .

The constitutive equation between the uniaxial steady state creep rate $\dot{\varepsilon}_{uni}$ and the uniaxial stress σ_{uni} describing the power law creep is given by,

$$\dot{\varepsilon}_{uni} = A \sigma_{uni}^n \quad (4.3)$$

where, n is the stress exponent and A is the power law coefficient which incorporates the temperature dependence of steady state creep rate.

As discussed in Chapter 2, for materials obeying power law creep, it was found that the impression velocity v_{imp} was proportional to the punch diameter and had the same stress dependence as was observed in the conventional uniaxial creep test [1,2,3]. Hence,

$$\frac{v_{imp}}{D} \propto \sigma_{imp}^n \quad (4.4)$$

where, v_{imp} is impression velocity, σ_{imp} is the punching stress, D is the diameter of the punch and n is the stress exponent value. Therefore, uniaxial creep parameters in Eqn. 4.3 and impression creep parameters in Eqn. 4.4 can be correlated as,

$$\sigma_{uni} = \alpha \sigma_{imp} \quad (4.5)$$

and,

$$\dot{\varepsilon}_{uni} = \frac{v_{imp}}{\beta D} \quad (4.6)$$

where, α and β are the correlation factors.

As mentioned in Chapter 2, experimentally determined values of α range from 0.26 to 0.36 for a range of materials such as Pb, TiAl alloys, Mg-8Zn-4Al-0.5Ca alloy, Zn, cast Mg-5Sn-xCa alloys, 316 stainless steel [1, 4,5, 6,7, 8, 9]. Equation (4.6) is often used with $\beta=1$ [1, 10, 5, 6, 8]. For the present analysis, we used the conversion factors $\alpha=0.33$ and $\beta=1$, determined by finite element calculation reported by H. Y. Yu et.al [2, 11] to relate the creep data from impression and conventional tensile creep tests.

The plot of steady state impression velocity versus punching stress on a log-log scale gives a straight line with a slope equivalent to n_{imp} . It can be written as,

$$n_{imp} = \left(\frac{\partial \ln(dh/dt)}{\partial \ln \sigma_{imp}} \right) \quad (4.7)$$

4.2.3 Impression Creep Tests

Impression creep tests were conducted at 923 K on 316LN SS under different constant punching stress levels of 472, 591, 675 and 760 MPa. The impression creep testing system which is developed at IGCAR for conducting these studies is described in Chapter 3. Impression creep specimens of dimension 20 mm x 20 mm x 10 mm were used. Specimen preparation for impression creep tests are explained in Chapter 3. For impression creep tests, the sample dimension requirements are not stringent as long as two flat ends are parallel, and the specimen height should be large enough to contain the plastic zone well within the specimen. A tungsten carbide flat-ended cylindrical indenter of 1 mm diameter was employed. The experiments were carried out in vacuum of 10^{-6} mbar in order to avoid the oxidation of the specimens during the test. A pre-load of 9.8 N (100 g on loading pan) was applied on the specimen for keeping the specimen

and indenter in contact before the actual load is applied. The test temperature was maintained within $\pm 1^{\circ}\text{C}$ during the test. After the application of the final load the displacement of the cylindrical punch was recorded as a function of elapsed time using Linear Variable Differential Transducer (LVDT), and the data was acquired online by the data acquisition system. The accuracy of the punch displacement measurement was better than $\pm 0.5\%$.

4.2.4 Microstructure of the Alloy Prior to Impression Creep Testing

Microstructural characterization of 316LN SS containing 0.14 wt. % nitrogen was carried out before impression creep testing. Figure 4.1 shows the back-scattered image (BSE) of the microstructure of the alloy which was solution treated at 1373 K for 1 hour followed by water quenching. Nearly equiaxed grains which are distributed uniformly in the matrix were observed. The average grain size of the alloy was about 85 μm .

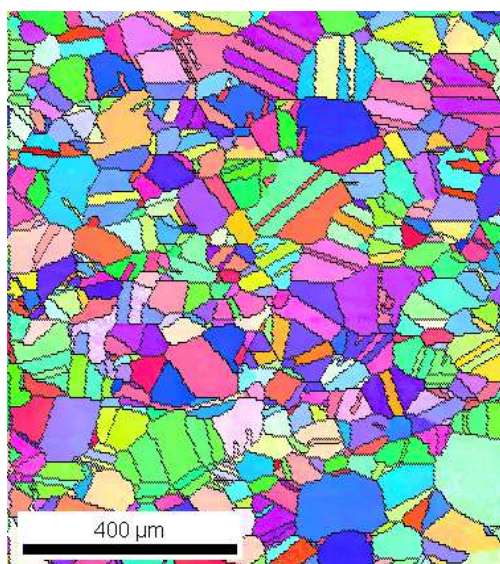


Fig. 4.1 Microstructure of solution annealed 316LN SS containing 0.14 wt. % nitrogen.

4.2.5 Impression Creep Curves

Figure 4.2 shows the typical impression creep curves obtained for 316LN SS containing 0.14 wt. % nitrogen, under punching stress levels of 472, 591, 675 and 760 MPa, at 923 K. The depth of penetration of the indenter was plotted as a function of test time for different stress levels. Impression creep curves exhibited two characteristic creep stages, namely, a primary creep stage and a secondary creep stage. However, the tertiary creep stage that appears in conventional creep curves was found to be absent here. This is attributed to the fact that in impression creep test, loading is compressive in nature. As a consequence, creep cracks and necking of specimen which occur during the tertiary creep stage leading to fracture do not take place. An advantage with the absence of tertiary creep stage here is that the deformation of the material under the punch is stable and hence the secondary creep stage sustains for a long time resulting in a true steady state. Further, because of the absence of tertiary creep stage there is no slope change after the steady state creep stage is attained. Hence, it is easier to locate the steady state portion (where depth increases linearly with time) from the creep curve directly and determine the true steady state creep rate. The rate at which the cylindrical punch penetrated into the test specimen was controlled by the time dependence of the movement of the material under the punch, and thus directly monitored the creep behavior of the materials. It is evident that increasing punching stress at a constant temperature results in higher punch penetration rates as we generally observe in uniaxial creep curves where creep rate increases with increasing applied stress. The longest test time in this investigation was 1000 h. Figure 4.3 shows the typical impression on the surface of the specimen after the test. It should be noted that the test at 760 MPa was interrupted as soon as it reached the steady state while tests at lower stresses were continued in the steady state for sufficiently longer time.

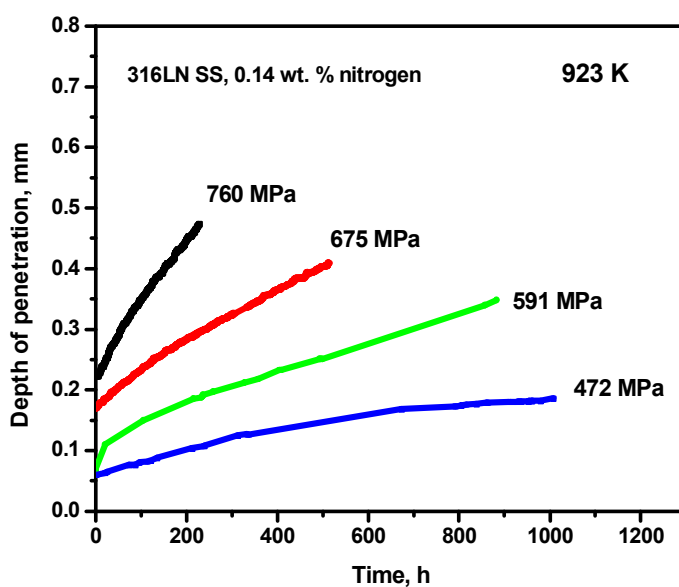


Fig. 4.2 Plot of impression depth versus time for 316LN SS containing 0.14 wt. % nitrogen at various stress levels.

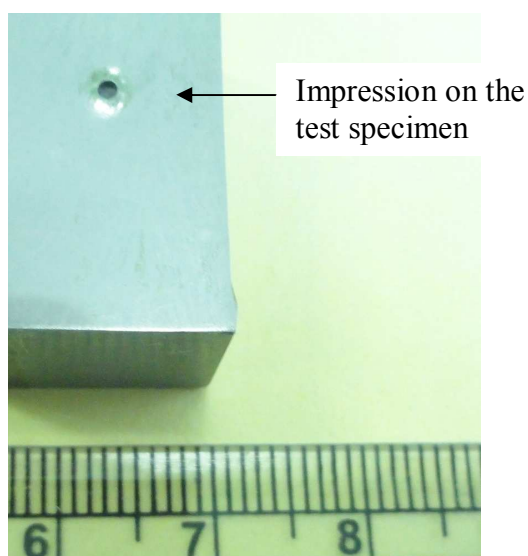


Fig. 4.3 Image of typical impression on the surface of the specimen.

4.2.6 Stress Dependence of the Steady State Impression Velocity

Figure 4.4 shows the typical variation of impression velocity with time at different stress levels for 316LN SS containing 0.14 wt. % nitrogen. It was observed that the impression velocity decreases initially during the primary creep stage and then reaches a constant value indicating the steady state creep stage.

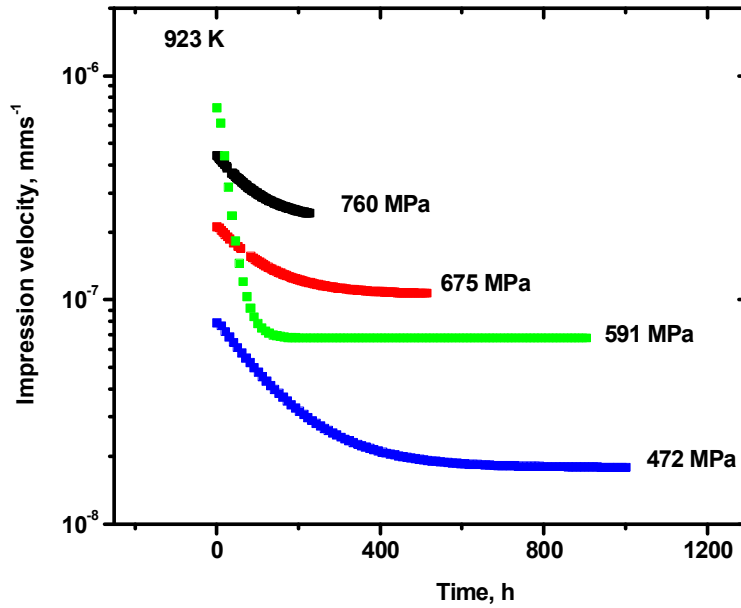


Fig. 4.4 Variation of impression velocity with time for various stress levels indicating the steady state for 316LN SS containing 0.14 wt. % nitrogen.

In order to determine the stress dependence of the steady state impression velocity, the slope of steady state portion of the impression creep curves which gives the steady state impression velocity (or from impression velocity versus time graphs) was calculated for each stress level. These steady state impression velocities were plotted against the punching stresses on a log-log scale. Figure 4.5 shows the variation of steady state impression velocity with punching stress (log-log plot) for 316LN SS containing 0.14 wt. % nitrogen. The Norton power law relationship between the steady

state impression velocity and punching stress was found to be obeyed. According to the Eqn. 4.7, the slope of the straight line yields power law exponent value n_{imp} . The power law exponent thus obtained for 316LN SS containing 0.14 wt. % nitrogen was 6.4 [12,13].

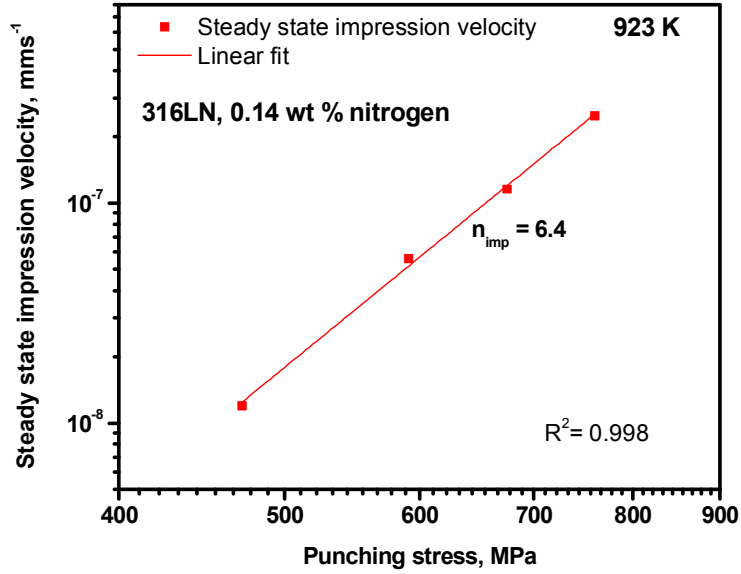


Fig. 4.5 Norton power law relationship between steady state impression velocity and punching stress for 316LN SS containing 0.14 wt. % nitrogen.

4.2.7 Comparison of Impression and Uniaxial Creep Data

In order to validate the impression creep technique, the data obtained from impression creep tests were compared with the data obtained from conventional uniaxial creep tests. The calculated steady state impression velocity and the punching stress were converted to an equivalent uniaxial steady state creep rate and uniaxial stress using Eqns. 4.5 and 4.6 respectively with the help of correlation factors. Figure 4.6 shows the comparison between the steady state creep rate obtained from conventional uniaxial creep tests and from impression creep tests for various stress levels. The steady state

creep rate values obtained from impression creep tests and from uniaxial creep tests were found to be in close agreement. The power law exponent value $n_{imp} = 6.4$ obtained from impression creep tests was in close agreement with the stress exponent value $n_{uni} = 6.9$ obtained from conventional uniaxial creep tests on 316LN SS containing 0.14 wt. % nitrogen [14].

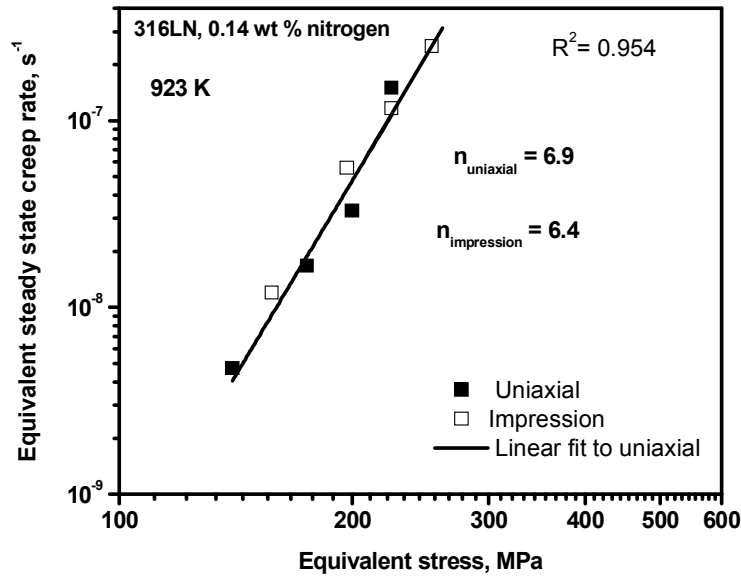


Fig. 4.6 Correlation between impression creep and conventional uniaxial creep data [14] for 316LN SS at 923 K.

4.2.8 Evaluation of the Apparent Activation Energy for Creep Deformation from Impression Creep Technique

4.2.8.1 Impression Creep Tests

Impression creep tests were conducted on 316LN SS containing 0.14 wt. % nitrogen at different temperatures of 898, 923, 948 and 973 K, at a constant punching stress level of 675 MPa. Tests were conducted as described in the previous section. All the

experiments were carried out under vacuum of 10^{-6} mbar. Different specimens were used for each test at different temperatures.

4.2.8.2 Impression Creep Curves

Typical impression creep curves at 898, 923 and 948 K, at a punching stress of 675 MPa are shown in Fig. 4.7. As can be seen, impression creep curves exhibited a primary creep stage followed by a secondary creep stage where impression depth increased linearly with time. It can be observed that increase in temperature under a constant stress, results in a higher penetration rate [15].

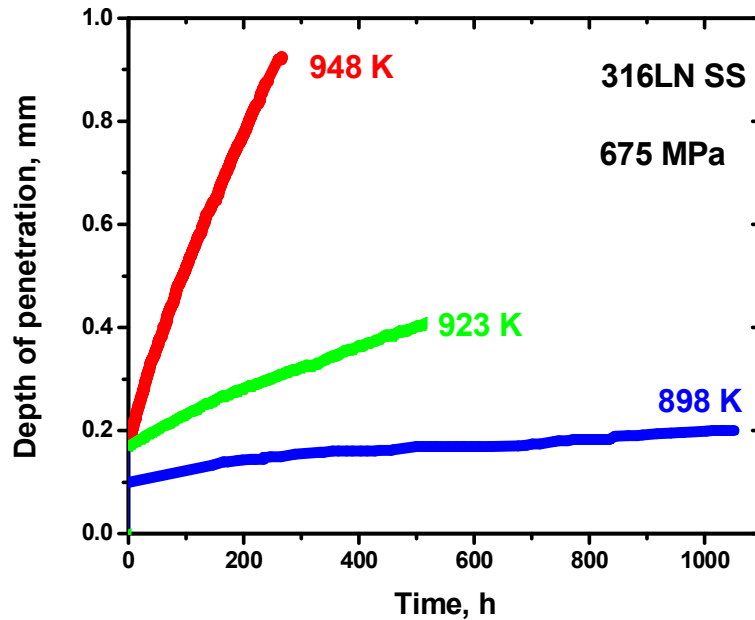


Fig. 4.7 Typical impression creep curves at various temperatures at a constant punching stress of 675 MPa for 316LN SS containing 0.14 wt. % nitrogen.

Figure 4.8 shows the plot of variation of impression velocity with time for different test temperatures. The impression velocity decreased in the primary creep stage and then reached a constant value indicating a steady state creep region. It can be noted that variation of the test temperature in a small range of 25 °C produced a significant change

in the indenter penetration rate. The steady state impression velocity was found to be very sensitive to the temperature change.

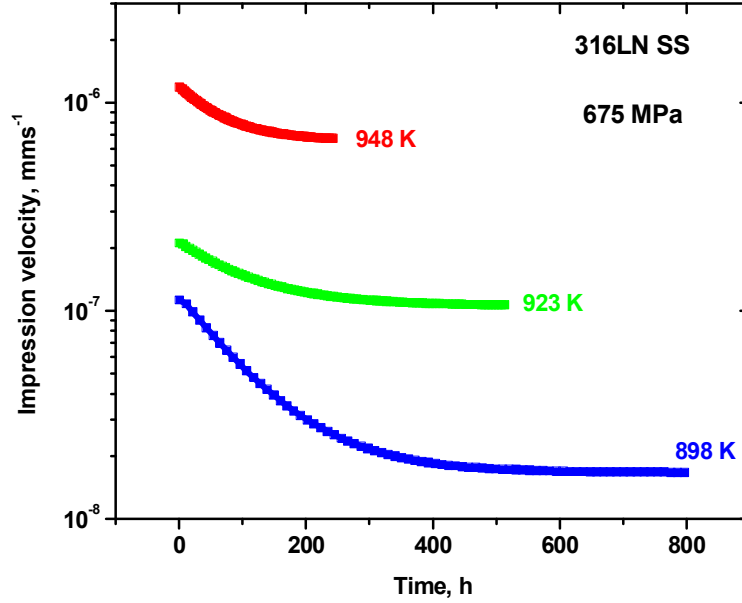


Fig. 4.8 Temperature dependence of impression velocity in 316LN SS containing 0.14 wt. % nitrogen at 675 MPa.

4.2.8.3 Analysis of Activation Energy for Creep in 316LN SS

The steady state creep rate of the material depends on the stress and temperature. When the stress is constant, creep rate depends on the temperature according to Arrhenius rate equation which is given by,

$$\dot{\epsilon}_{uni} = A \exp\left(-\frac{Q_c}{RT}\right) \quad (4.8)$$

where $\dot{\epsilon}_{ss}$ is the steady state creep rate, A is the constant, Q_c is the apparent activation energy for rate controlling process, R is the universal gas constant ($8.314 \text{ Jmol}^{-1}\text{K}^{-1}$), T is the absolute temperature.

To determine the apparent activation energy from impression creep technique, a similar methodology which we generally use in conventional creep technique was followed here. The steady state impression velocities were plotted against the reciprocal of the absolute temperature on a semi-logarithmic scale as shown in Fig. 4.9. The graph illustrates the temperature dependence of the steady state impression velocity at constant punching stress of 675 MPa. Arrhenius rate equation was found to be operative between the steady state impression velocity and the temperature. Hence, Arrhenius rate equation in impression creep can be stated as,

$$\frac{v_{imp}}{D} = A \sigma_{imp}^n \exp\left(-\frac{Q_c}{RT}\right) \quad (4.9)$$

where, v_{imp} is the steady state impression velocity, d is the diameter of the punch, Q_c is the apparent activation energy for rate controlling process, R is the universal gas constant and A is the constant.

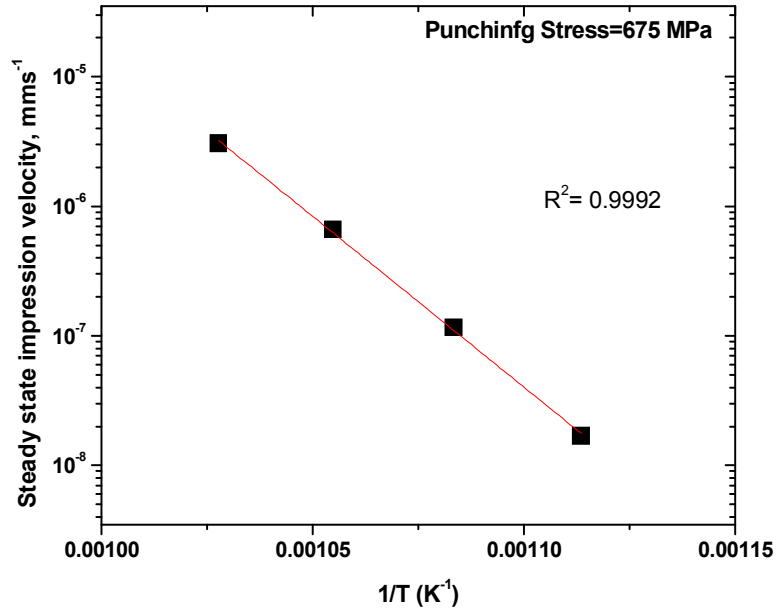


Fig. 4.9 Arrhenius type relationship between the steady state impression velocity and the temperature.

The steady state impression velocities were converted to an equivalent uniaxial steady state creep rate using the Eqn 4.6 and the correction factor $\beta=1$. The equivalent steady state creep rate was then plotted against the reciprocal of the absolute temperature on a semi-logarithmic scale as shown in Fig. 4.10. The apparent activation energy calculated from the slope of the straight line, i.e $-Q/2.3R$ was 504 kJmol^{-1} [15] This apparent activation energy value was in general agreement with the apparent activation energy value reported by Morris et al. [16] for type 316 SS ($480\text{-}500 \text{ kJmol}^{-1}$), Mathew et al. [17] for type 316 SS (475 kJmol^{-1}) and for 316LN SS (585 kJmol^{-1}) and Park et al. [18] for type 316 SS (395 kJmol^{-1}). Morris et al. [16] found that the apparent activation energy value for type 316 SS at all the stresses in the range 50-500 MPa and temperatures above 848 K, was approximately constant i.e., $480\text{-}500 \text{ kJmol}^{-1}$. The range of temperature and the stress in which Mathew et al. [17] studied creep behavior was 873-973 K and 215-335 MPa, respectively, and studied by Park et al.[18] was 923-983 K and 205-285 MPa.

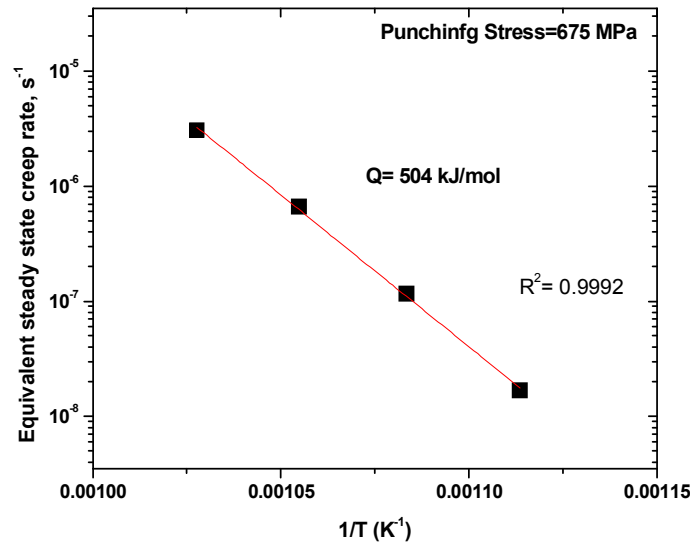


Fig. 4.10 Temperature dependence of the equivalent steady state creep rate for 316LN SS.

The apparent activation energy together with the stress exponent is used to identify the creep deformation mechanism. Based on the apparent activation energy value of $Q_c=504 \text{ kJ mol}^{-1}$ and the stress exponent $n=6.4$ obtained in this investigation, it can be concluded that the rate controlling deformation mechanism is dislocation creep. Dislocation creep involves the movement of dislocations which overcome barriers by thermally assisted mechanisms involving diffusion of vacancies or interstitials, i.e., dislocation glide aided by vacancy diffusion [19]. At elevated temperature, if a gliding dislocation is held up by an obstacle, a small amount of climb may permit it to overcome the obstacle, allowing it to glide to the next set of obstacles where the process is repeated. The glide step produces almost all of the strain but climb step controls the velocity. Since dislocation climb requires diffusion of vacancies or interstitials, the rate controlling step is atomic diffusion. The stress exponent for dislocation creep varies from 3-8 for most metals, with a value of 5 most common. It is important to note here that the stress exponent in the present study also lie in the above mentioned range, signifying the occurrence of dislocation creep mechanism in the alloy studied although the determined activation energy is higher than the activation energy for self diffusion of various elements in type 316 SS determined by Hirano and Iijima [20] from tracer diffusion measurements ($Q_{Fe}=228 \pm 3 \text{ kJ mol}^{-1}$, $Q_{Cr} = 243 \pm 3 \text{ kJ mol}^{-1}$, $Q_{Mo} = 143 \pm 7 \text{ kJ mol}^{-1}$ and $Q_{Mn} = 260 \pm 4 \text{ kJ mol}^{-1}$). As mentioned earlier the apparent activation energy value obtained in the present study are in close agreement with the values determined from independent creep tests reported by Morris et al.[16], Mathew et al.[17] and Park et al.[18]. However, activation energy determinations from temperature change tests yielded a value of $270 \pm 20 \text{ kJ mol}^{-1}$ [16]. The difference in these values has been attributed to the structural differences (carbide and dislocation density) that occur during two testing methods [17]."

The unified equation for steady state creep rate proposed by Bird and co workers [21] is given by,

$$\dot{\varepsilon}_{uni} = A_3 \left(\frac{b}{d} \right)^p \left(\frac{D_0 E b}{kT} \right) \left(\frac{\sigma_{uni}}{E} \right)^n \exp \left(- \frac{Q_c}{RT} \right) \gamma^a \quad (4.10)$$

where, $\dot{\varepsilon}_{uni}$ is the steady state creep rate, A_3 is the constant, b is the Burger vector of the material, d is the grain size, D_0 is a frequency factor, E is the temperature dependent elastic modulus, k is the Boltzmann's constant, T is the absolute test temperature, σ_{uni} is uniaxial stress, Q_c is the apparent activation energy, R is the gas constant, γ is the stacking fault energy, p and n are constants, defined as the inverse grain size exponent and the stress exponent, respectively, and a is constant.

Applicability of this constitutive equation (Eqn. 4.10) for the impression creep test results has been analyzed. The temperature-compensated steady state impression velocity (in place of steady state creep rate) for different temperatures (898, 923, 948 and 973 K) at 675 MPa and for different punching stresses (760, 675, 591 and 472 MPa) at 923 K, were plotted against the modulus-compensated punching stress on a double logarithmic scale as shown in Figure 4.11. Here, the temperature dependent elastic modulus E was calculated according to the equation $E(\text{MPa}) = 201660 - 84.8 \theta(^{\circ}\text{C})$ [22]. The apparent activation energy value 504 kJmol^{-1} obtained in the present analysis was used in the plot. It was observed that the temperature-compensated steady state impression velocity plotted so fall on a straight line indicating that the above constitutive equation which is obeyed in uniaxial creep test correlates satisfactorily in impression creep test also. The value of stress exponent was determined to be 6 [15].

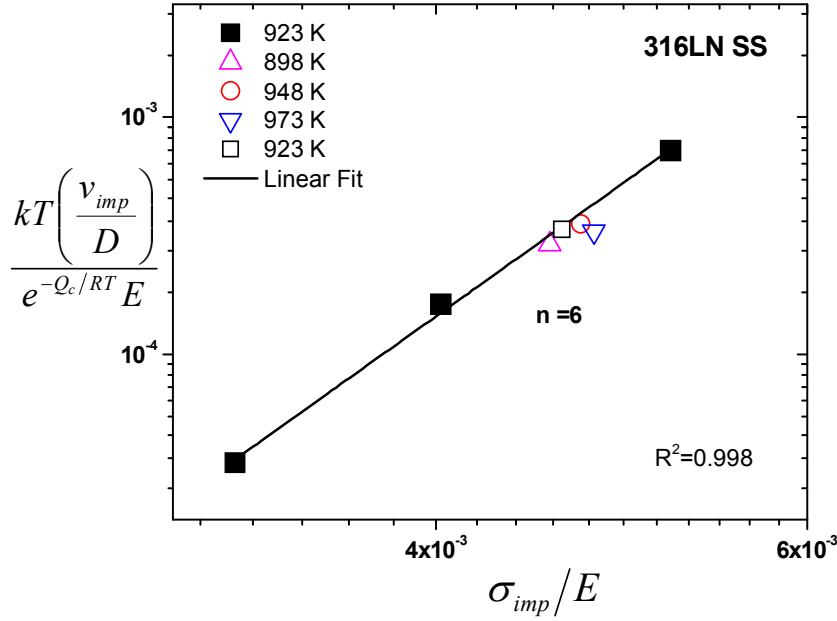


Figure 4.11 The variation of temperature-compensated steady state impression velocity with the modulus-compensated punching stress (log-log scale) for 316LN SS (the steady state impression velocity normalized to the diameter D of the punch represents the uniaxial steady state strain rate). The constitutive equation given in Eqn.4.10 satisfactorily correlates for the impression creep test data for 316LN SS.

4.3 Evaluation of the Effect of Nitrogen on Creep Behavior of 316LN SS

In order to study the influence of nitrogen on the creep behavior of 316LN SS, impression creep tests were carried out on 316LN SS containing varying nitrogen contents [23]. For this purpose, four different heats of 316LN SS which contain 0.07, 0.11 0.14 and 0.22 wt. % nitrogen were selected. Impression creep tests were conducted at 923 K on each heat under different punching stress levels of 472, 591, 675 and 760 MPa. Vacuum of 10^{-6} mbar was maintained during the test at 923 K.

4.3.1 Initial Microstructure of the Alloys

The initial microstructure of the 316LN SS containing 0.07, 0.11, 0.14 and 0.22 wt. % nitrogen are shown in Fig. 4.12. Microstructures shown in Fig. 4.12 are BSE images studied using scanning electron microscope. The material was solution treated at 1373 K for 1 hour followed by water quenching before specimen preparation for creep tests. Nearly equiaxed grains which are distributed uniformly in the matrix, was observed. The average grain size of the material was found to be 85 μm .

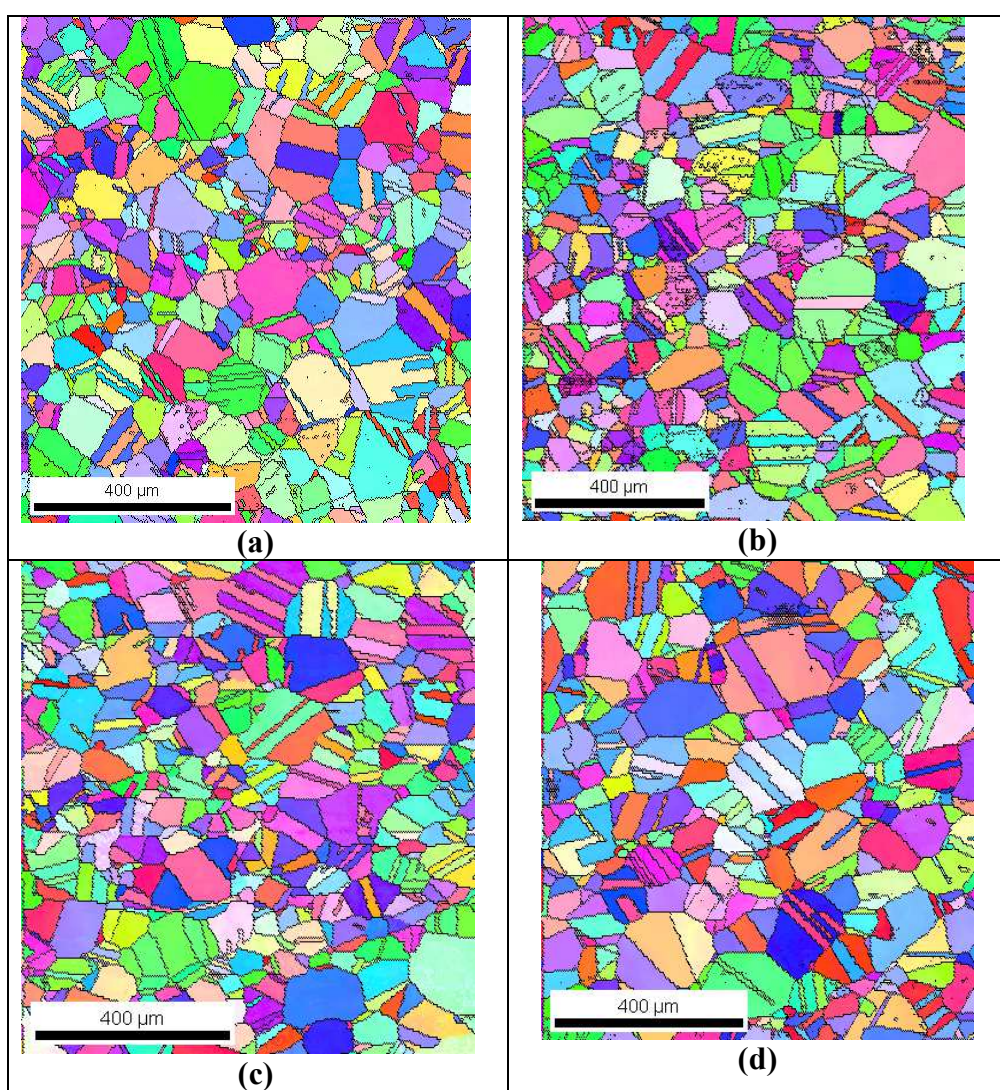


Fig. 4.12 Microstructure of solution annealed 316LN SS containing (a) 0.07, (b) 0.11, (c) 0.14 and (d) 0.22 wt. % nitrogen.

4.3.2 Impression Creep Curves

Typical impression creep curves presented as variation of punch penetration depth with dwell time under different punching stress levels for 316LN SS containing different nitrogen contents are depicted in Figs. 4.13, 4.14 and 4.15 respectively. As was observed for alloy containing 0.14 wt. % nitrogen, these creep curves also exhibited a primary creep stage and a secondary creep stage.

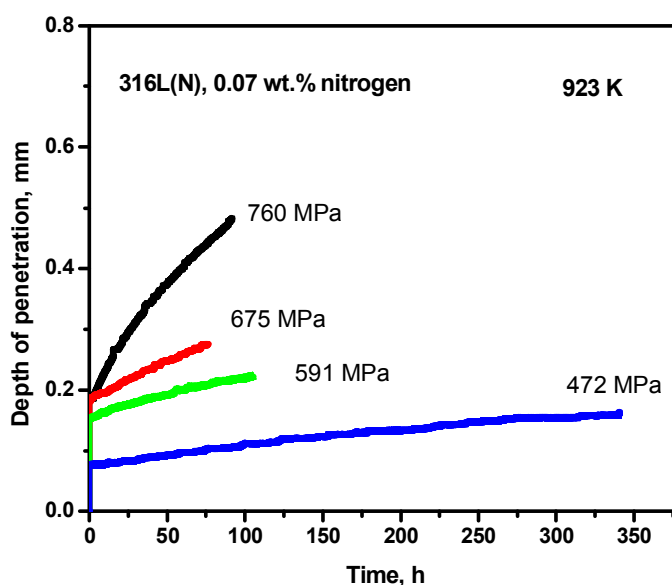


Fig. 4.13 Plot of impression depth versus time for 316LN SS containing 0.07 wt. % nitrogen at various stress levels.

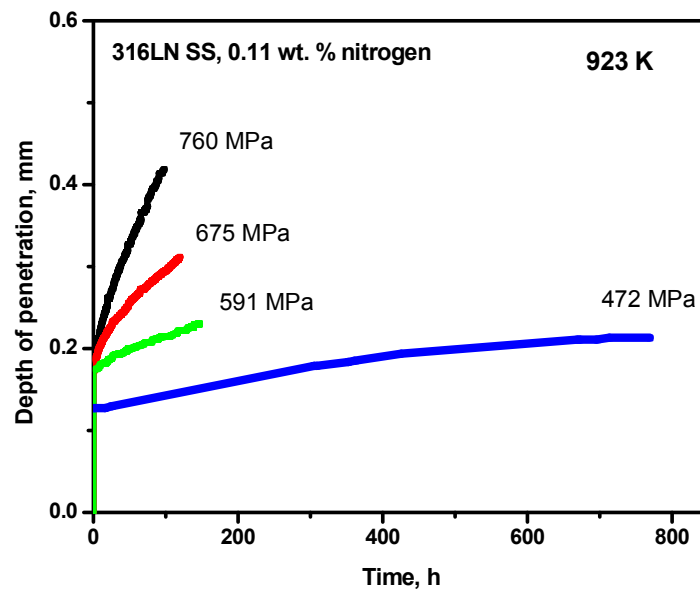


Fig. 4.14 Plot of impression depth versus time for 316LN SS containing 0.11 wt. % nitrogen at various stress levels.

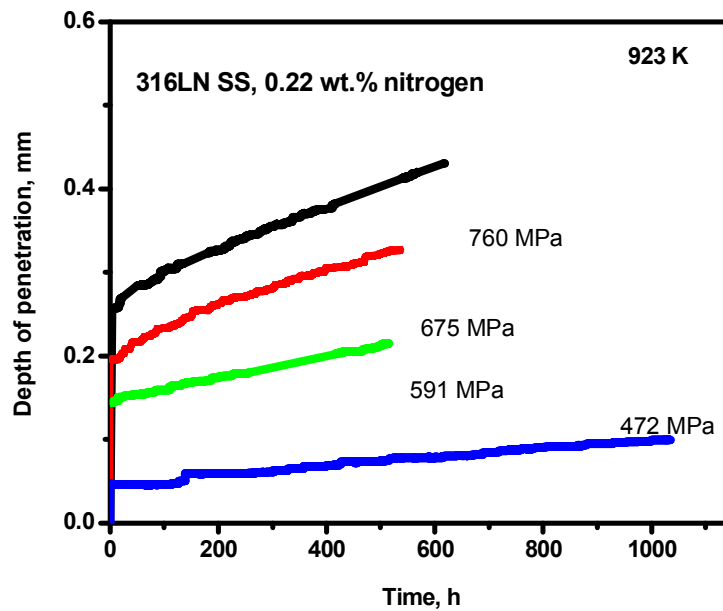


Fig. 4.15 Plot of impression depth versus time for 316LN SS containing 0.22 wt. % nitrogen at various stress levels.

4.3.3 Effect of Punching Stress on Impression Velocity

Figure 4.16 shows the log-log plot of steady state impression velocity against punching stress for all the four heats. Steady state impression velocity was found to increase with increasing punching stress. A power law relationship between steady state impression velocity and punching stress was found to be obeyed in all the four heats. The power law exponent (n) varied between 3.3 and 8.2 depending upon the nitrogen content in the heat. Similar observations were found in the case of conventional uniaxial creep tests carried out on these materials [14]. Figure 4.17 shows the plot of equivalent steady state creep rates and uniaxial tensile stresses derived from steady state impression velocities and punching stresses using Eqns. 4.5 and 4.6 for various nitrogen levels.

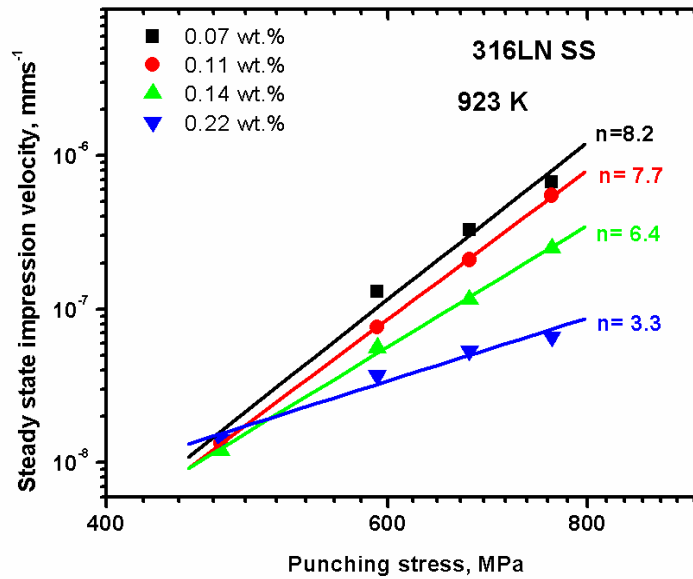


Fig. 4.16 Variation of steady state impression velocity with punching stress for different nitrogen content.

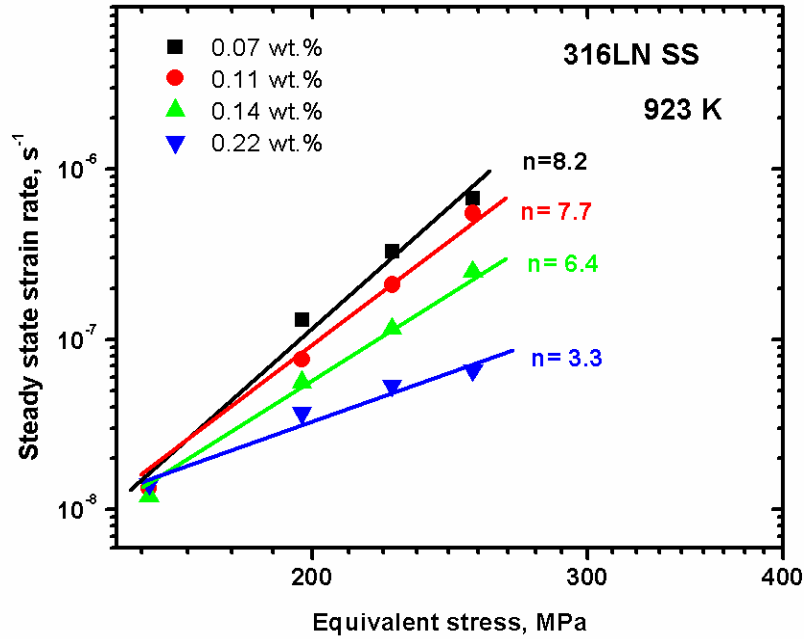


Fig. 4.17 Plot of equivalent steady state creep rates and uniaxial tensile stresses derived from steady state impression velocities and punching stresses using Eqns. (4.5) and (4.6) for various nitrogen levels.

A decrease in n value (stress exponent) with increasing nitrogen content was observed. This could be attributed to the following reasons. Nitrogen addition generally enhances solid solution strengthening in 316LN SS because of strong pinning of dislocations by nitrogen interstitials. Also, with increasing nitrogen the stacking fault energy decreases [14]. As a result, the tendency for the occurrence of thermally activated dislocation motion for e.g. dislocation climb decreases which causes decrease in steady state creep rate with increase in nitrogen content. This in combination with the effect of stress causes the decrease in slope (n value) with increasing nitrogen content.

4.3.4 Influence of Nitrogen content on Impression Velocity

Figure 4.18 shows the variation of the steady state impression velocity with nitrogen content for different punching stress levels. The nitrogen content, the only element which is varied in the material, showed a pronounced effect on the steady state impression velocity. Impression creep testing technique was found to be sensitive to capture the small variation in creep rate due to the small change in composition in the alloy. It was observed that the steady state impression velocity decreased with increasing nitrogen content at all the four stress levels. This result is in good agreement with the results obtained from conventional uniaxial creep tests which showed a decrease in steady state creep rate with increasing nitrogen content [14,24]. Nitrogen was found to be beneficial to creep properties at all the stress levels. The beneficial effect of nitrogen on the creep properties of 316LN SS was clearly brought out in the present investigation. Decrease in the steady state impression velocity with increasing nitrogen content could be attributed to the following reasons. Nitrogen is considered to be a potent interstitial solid solution strengthener which improves tensile, creep and fatigue strength of austenitic stainless steels [25]. Interstitially dissolved nitrogen increases the yield strength and ultimate tensile strength of austenitic stainless steels. The variation of the yield strength with nitrogen content in austenitic stainless steel was reported to be linear at room temperature and above [26,27]. The beneficial effect of nitrogen can be attributed to the fact that dissolved nitrogen caused a strong pinning with dislocations [14]. Furthermore, the stacking fault energy (SFE) also influences the creep strength of 316LN SS. Lower SFE is known to be beneficial to creep strength. In 316LN SS it was found that SFE value decreases with increasing nitrogen content [14].

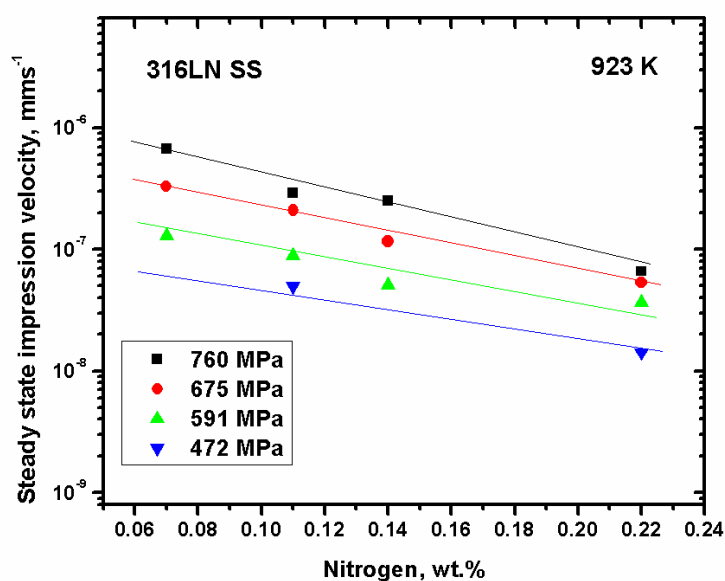


Fig. 4.18 Variation of steady state impression velocity with nitrogen content in 316LN SS for various stress levels.

4.4 Analysis of the Plastic Zone in Impression Creep Test

In impression creep tests, the material beneath the indenter undergoes complex elastic/plastic deformation during the initial loading and creep deformation stages. Hence, in spite of the fact that the test methodology is simple and straightforward, interpretation and the analysis of the complex deformation which occur during indentation is quite intricate. The basic requirement for understanding the mechanism of impression creep is the thorough knowledge of the plastic zone associated with impression creep. It is very much essential that the size and shape of the plastic zone, and the extent of localization of the plastic deformation around the indentation is understood. The knowledge of this also provides useful guiding principles for standardizing the test technique such as the minimum distance that has to be maintained between the adjacent impressions in order to avoid the inaccurate measurement of creep

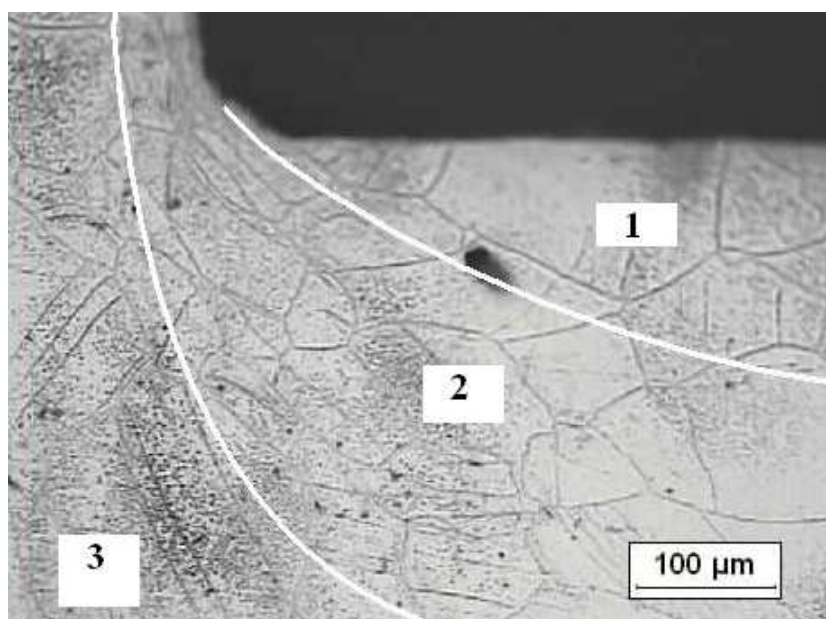
properties due to the interaction of their plastic zones, the minimum thickness of the test specimen required so as to avoid the influence of the specimen holder on creep process and hence its influence on test results. The present investigation is focused on understanding the plastic zone in impression creep tests by employing various characterization techniques.

4.4.1 Microstructural Characterization

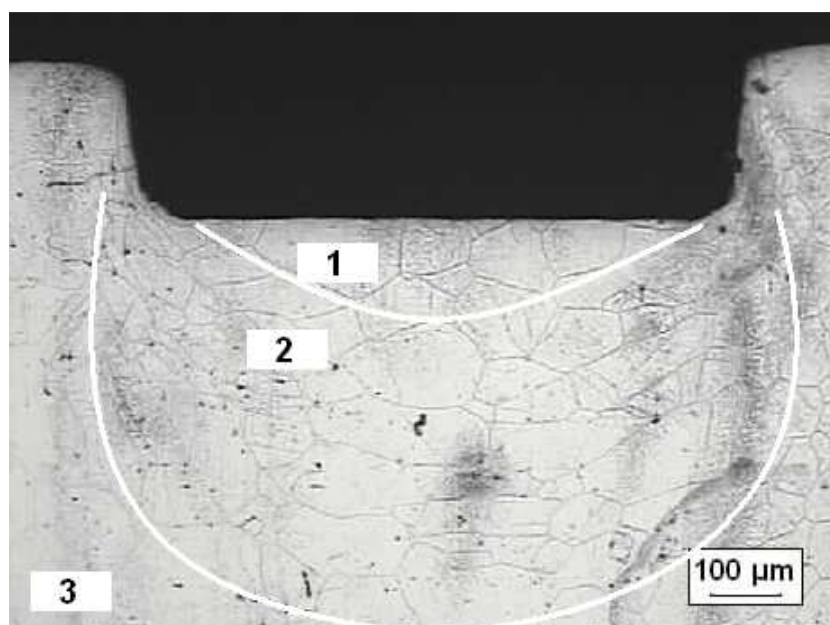
A systematic study of the microstructural evolution associated with the impression creep deformation in the vicinity of indentations was carried out to understand the deformation pattern and the extent of deformation at different locations around the indentation. To this end, cross-sectional analysis of the indentation was carried out. Impression creep tested specimens were sectioned just outside of the indentation using a low speed diamond saw and the surface was carefully ground and polished such that the final polished surface passed through almost the mid-section of the impression. The polished surface was etched electrolytically with solution of 60 % nitric acid in 40 % of distilled water to reveal the microstructure.

Typical microstructural changes observed [23] in the vicinity of the impression in 316LN SS containing 0.14 wt. % nitrogen after the impression creep test is shown in Figs. 4.19(a) and 4.19(b). Three distinct regions were observed which are labeled with numbers 1, 2 and 3. In order to distinguish these three regions clearly, curved lines are drawn. In region 1 no significant changes in grain shape were observed. This shows that the stress in this region may be hydrostatic in nature. The material in region 2 was found to experience an extensive shear deformation. For clear observation of the flow pattern in this region, SEM micrographs taken at higher magnification are shown in Figs. 4.20(a) and 4.20(b). These line patterns are associated with the material flow during the indentation. The density of these lines is found to be higher near the edge of

the indenter than in front of the indenter which indicates that the strain is higher near the edge of the indenter. No change in shape of grains in the region 3 which is far away from the indentation indicates absence of plastic deformation in this region. This clearly demonstrates the localized nature of impression creep test.

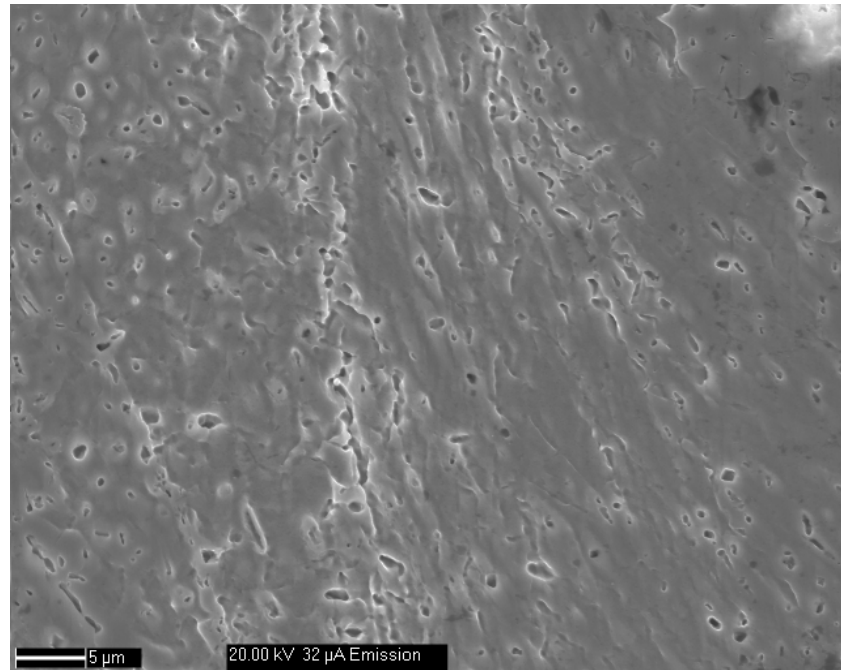


(a)

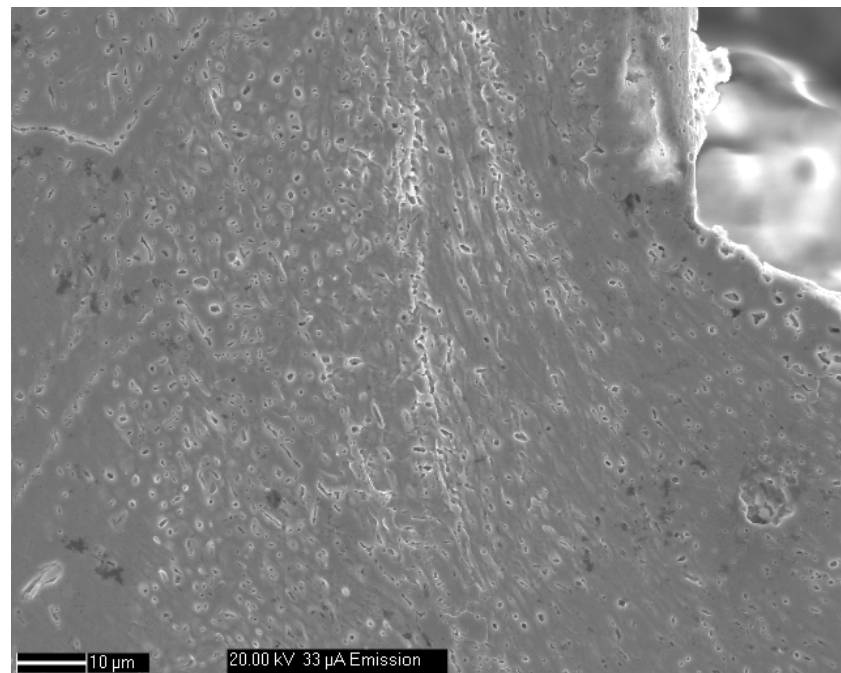


(b)

Fig. 4.19(a) and (b) Optical micrographs showing the typical deformation in the impression creep tested specimen.



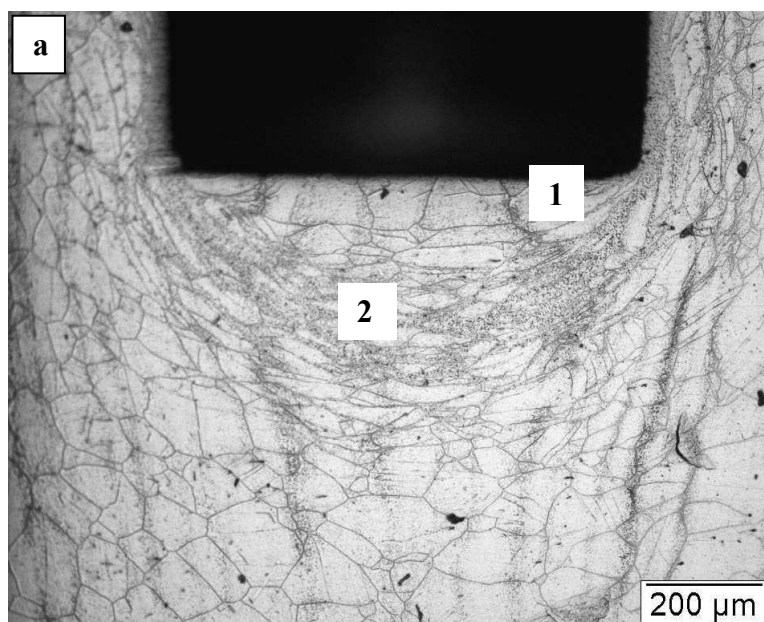
(a)



(b)

Fig. 4.20(a) and (b) SEM micrographs showing the material flow pattern near the edge of the indentation in 316LN SS containing 0.14 wt. % nitrogen after the impression creep test.

In order to clearly observe these distinct regions under the punch, the indenter was allowed to penetrate to a larger depth of about 0.9 mm in an impression creep test carried out on 316LN SS containing 0.14 wt. % nitrogen at 675 MPa. Figure 4.21 (a) and (b) show the deformation occurred in 316LN SS containing 0.14 wt.% nitrogen at a higher depth. It is evident that there exist three distinct regions under the punch and these regions are clearly distinguishable at higher depth of penetration because the extent of deformation is large at higher depth of penetration. This is because, in impression creep test depth is the representative of strain. Hence, higher the depth of penetration greater is the extent of deformation. As the depth increases the region 2 undergoes extensive shear deformation. It can also be observed that the shape of the plastically deformed zone is nearly hemispherical in which grains are elongated. However, in region 1 which is just below the punch, no significant change in the grain shape was observed. The region 3 which is far away from the indentation showed no change in the grain shape.



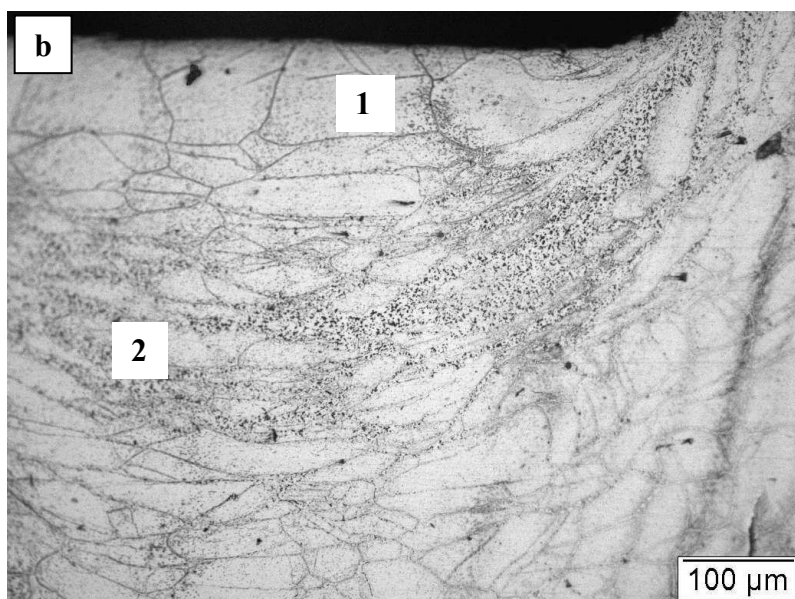


Fig. 4.21 (a) and (b) Optical micrographs showing the deformation in the impression creep tested specimen in 316LN SS containing 0.14 wt. % nitrogen tested at 948 K, under the punching stress of 675 MPa.

Further, in order to deepen the understanding of the extent of deformation and the shape of the plastic deformation zone, an impression creep test was conducted on 316LN SS containing 0.14 wt. % nitrogen, using 1.5 mm diameter indenter. The indenter was allowed to penetrate the specimen to a depth more than 1 mm (but less than 1.5 mm). Figure 4.22 shows the deformation around the impression in this test. Apart from the similar observations of large deformation in the region 2 and no significant grain shape change in region 1, it is evident that the plastic zone shape is almost hemispherical and the deformation zone 2 appears to be extended up to a depth of about 1 mm. Figure 4.23 shows the optical micrograph at a higher magnification depicting the elongated grains in the region 2. Figures 4.24(a) and (b) show the region 1 at higher magnification where there is no significant grain shape change. Micrograph shown in Fig.4.25 is the view in the radial distance where there may be deformation but

not so significantly reflected in the grain shape change. It can be observed from these optical micrographs (Figs. 4.19, 4.21 and 4.22) that the shape of the plastic zone is hemispherical.

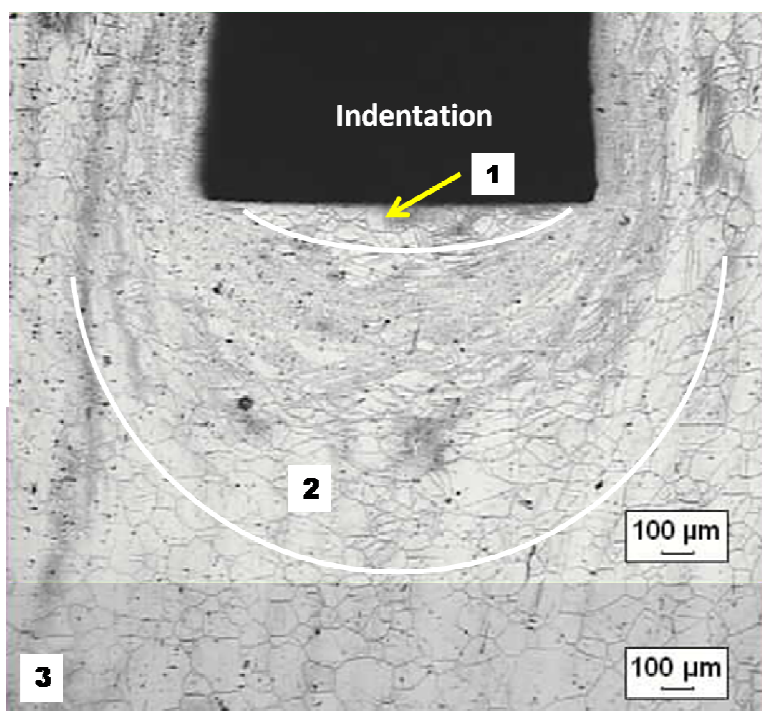


Fig. 4.22 Optical micrographs of impression creep regions in 316LN SS containing 0.14 wt. % nitrogen depicting three distinct regions in the vicinity of the impression. The deformed plastic zone was found to be hemispherical.

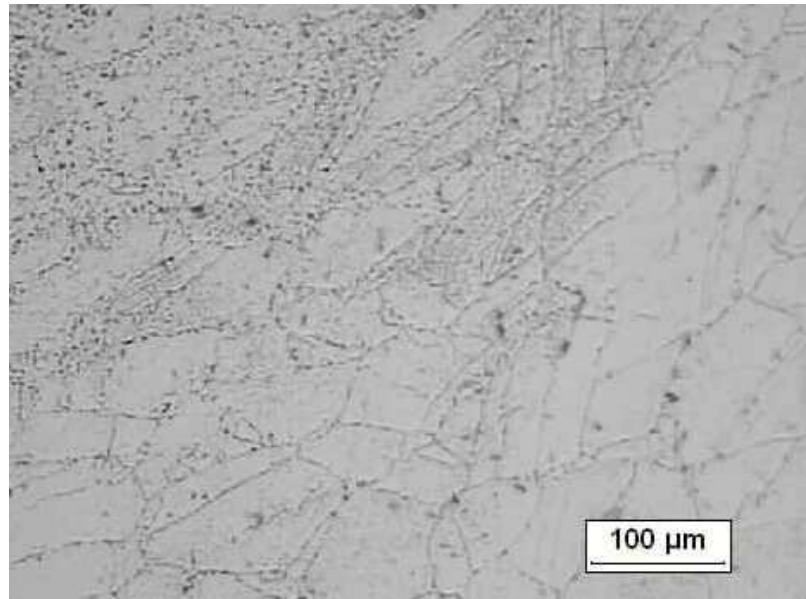
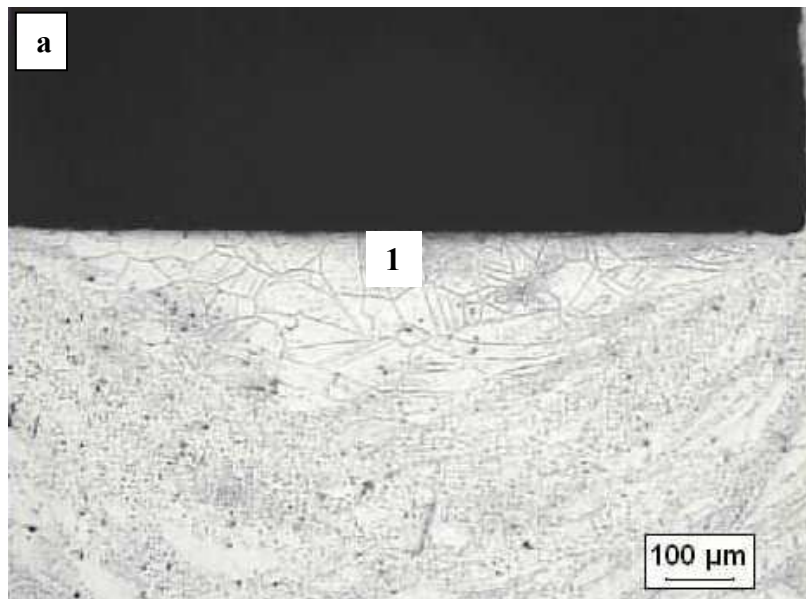


Fig. 4.23 Optical micrograph at a higher magnification showing the elongated grains in the region 2.



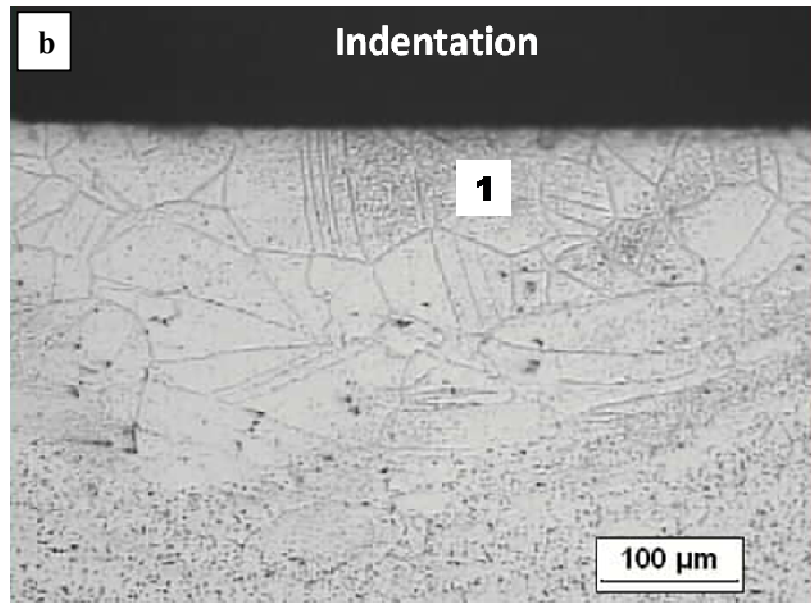


Fig. 4.24 (a) and (b) Optical micrographs at a higher magnification showing the region 1 just beneath the indentation. No significant change in the shape of grains in this region.

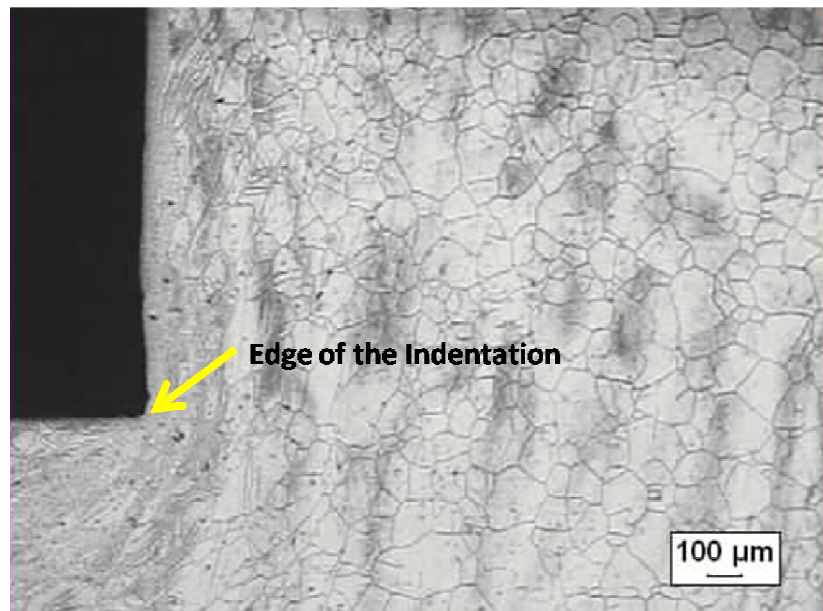
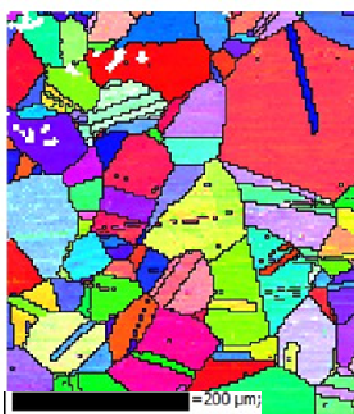
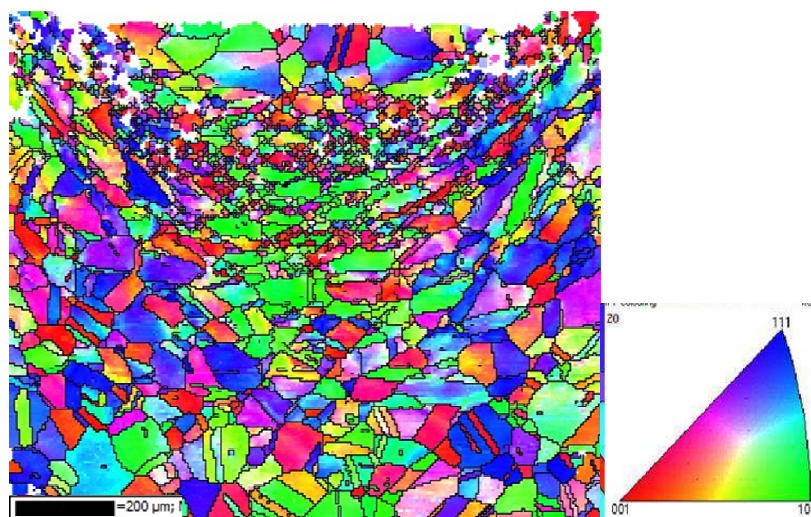


Fig. 4.25 Right corner of the impression showing extensive deformation in region 2 and no significant grain shape change away from the indentation in the radial direction.

Electron Backscattered Diffraction Analysis was carried out on the impression creep tested specimen in order to identify the crystallographic planes participating in the deformation process. The specimen preparation for EBSD analysis has been detailed in the Chapter 3. Inverse pole figure (IPF) maps for the underformed and deformed regions are depicted in Figs. 4.26(a) and (b), respectively, along with the standard legend triangle, in the impression creep specimen tested at 675 MPa, at temperature of 948 K. The deformed region below the punch is divided into two distinct regions which are marked with numbers 1 and 2 as shown in Fig 4.26(b). The region 1 showed no significant deformation in terms of grain shape change. The region 2 experienced extensive deformation as was revealed from optical micrograph discussed earlier (Fig. 4.21). In addition, two distinct features in region 2 were analyzed; one was elongated grains and the other was fine/equiaxed grains. The deformation was found to occur predominantly on most favorable slip system like in any fcc metals.



(a)



(b)

Fig. 4.26 Comparison of inverse pole figure (IPF) maps of 316LN SS in the (a) undeformed which is away from the indentation and (b) deformed regions below the indentation.

The substructural evolution endured in the highly deformed region under the indentation was studied by transmission electron microscopy (TEM). The specimen preparation for this analysis has been detailed in the Chapter 3. Figure 4.27 shows the optical micrograph of the impression creep deformation in the specimen. The line marked on the micrograph indicates the region from which TEM specimen was prepared. Figures 4.28 (a) and (b) show the transmission electron micrographs of the highly deformed region (region 2) of the impression creep specimen tested at 973 K for 24 h, at a punching stress of 675 MPa. The dislocations in this region were found to be well dispersed in the matrix.

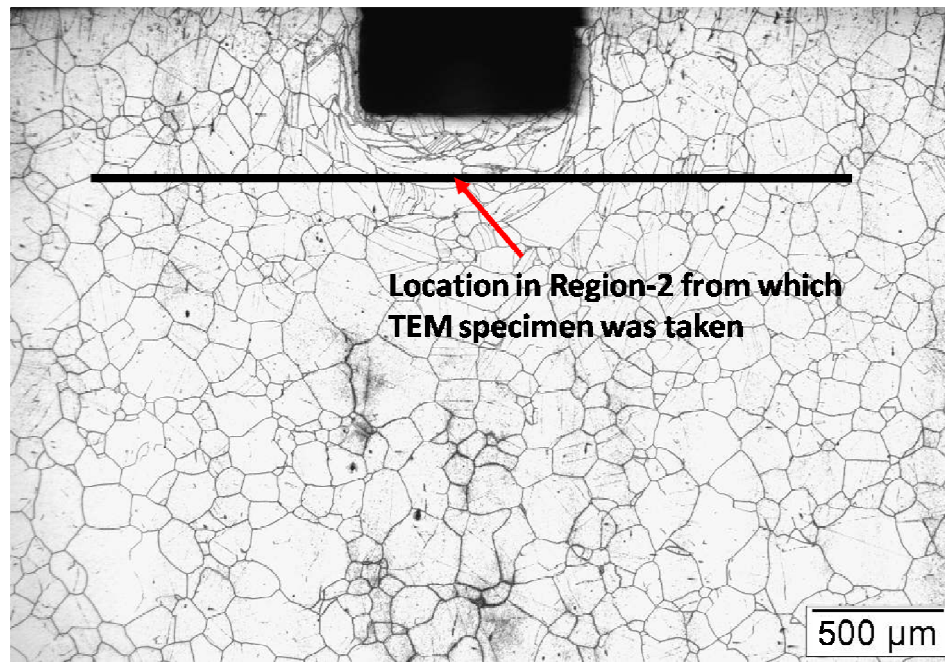


Fig. 4.27 Optical micrographs showing the deformation under the punch and the line indicating the region from which TEM specimen was taken.

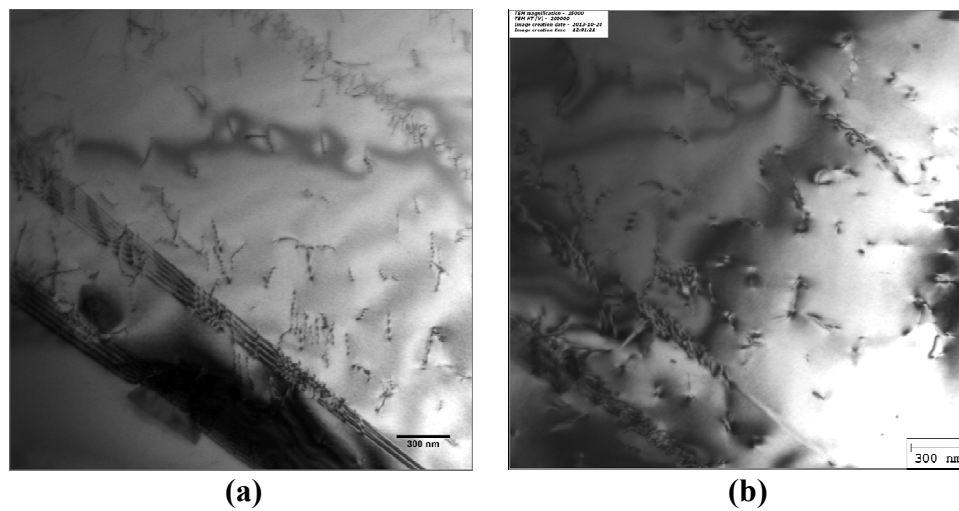


Fig. 4.28 TEM micrograph showing dislocation structure in region 2, which are well dispersed.

4.4.2 Microhardness Studies

Microhardness technique is one of the plastic zone size measurement techniques that is mostly applied to material that strongly work hardens like austenitic stainless steels or work soften like maraging steels [28]. The procedure is as simple as measuring microhardness around the indentation and determining elastic-plastic boundary as a sudden change in hardness.

In the present study, impression creep tested specimens were sectioned using a low speed diamond saw and the surface was carefully ground and polished such that the final polished surface passed through almost the mid-section of the impression. Microhardness measurements were made on the sectioned surface which was polished to 1 μm finish using diamond paste prior to microhardness measurements. A Microhardness tester of model HMV-2 with a Vickers scale was used for microhardness measurements.

A series of microhardness profiles were taken on the sectioned surfaces of the three impressions corresponding to impression creep test at punching stress levels of 760, 675 and 591 MPa in 316LN SS containing 0.22 wt. % nitrogen alloy. Microstructural changes around the indentation for these three different stress levels are shown in Fig. 4.29. Microhardness profiles taken along different lines and directions are shown in the optical micrograph in Fig 4.30 and also shown schematically in Chapter 3. Microindentations were made with spacing between adjacent indentations of at least 3 times the diagonal length of the microindentation as recommended by the ASTM standard for microhardness [29]. This prevents the inaccurate measurement of microhardness due to the overlapping of deformed zone associated with the neighboring microindents. In the present study, a load of 100 g was applied for 10 sec for each hardness measurements. The diagonal length of the microindentation was less than 30

μm and hence a spacing of minimum $125\ \mu\text{m}$ was maintained between the adjacent indentations.

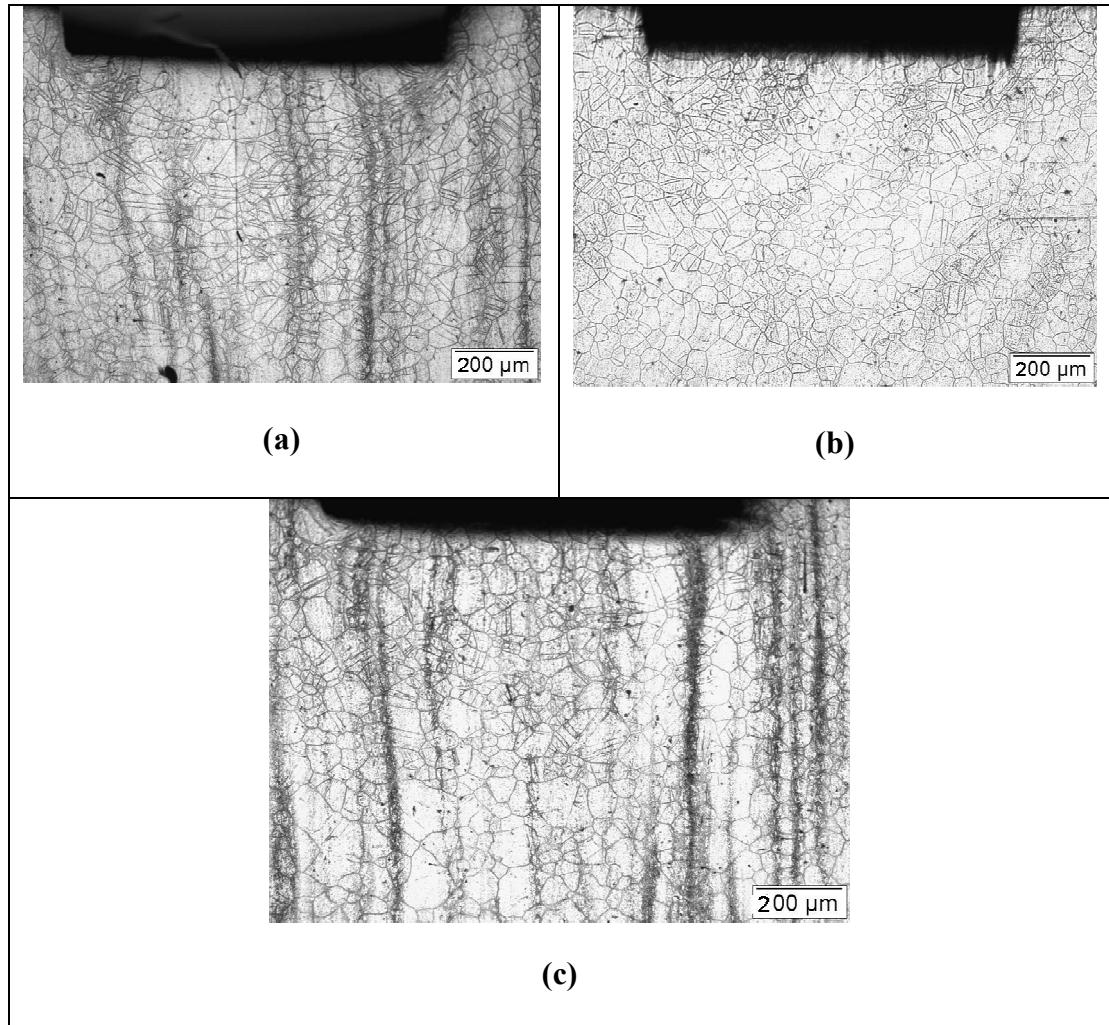


Fig. 4.29 Optical micrographs of impression creep regions in 316LN SS containing 0.22 wt. % nitrogen over which microhardness measurements were made: (a) 760MPa, (b) 675 MPa, (c) 591 MPa.

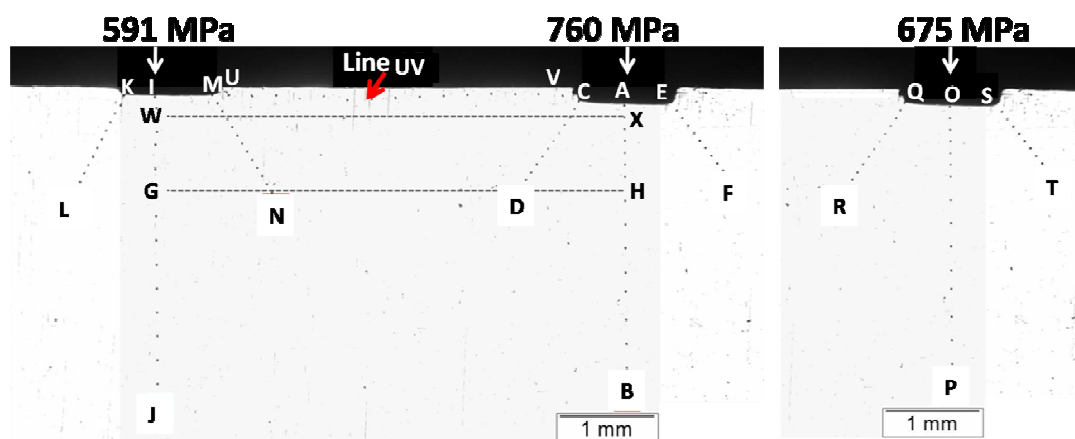


Fig. 4.30 Optical micrograph showing the microhardness profiles measured along different lines around the impressions.

Figure 4.31 shows the microhardness variation along the line UV (horizontal to the specimen surface) between the two impressions, one corresponding to impression creep test at 760 MPa and the other at 591 MPa as indicated in the micrograph. It was observed that the hardness value was higher, about 239 VHN, near the indentation and it decreased with the distance away from the impression and reached a lowest hardness value of 206 VHN at a distance of about 1.25 mm from the edge of the impression. In order to compare the hardness values in the plastic zone with the hardness of unaffected or non-hardened region, a reference region in the same specimen which is at a larger distance was selected and microhardness were measured. The average hardness in this region was 206 VHN as shown in the Fig. 4.32. Increase in the hardness near the impression indicates that the region is strain hardened due to the plastic deformation. Most metals exhibit strain hardening in their plastic response where the flow stress increases with plastic strain. Since the hardness is a strong function of flow stress and material work hardens with strain, hardness should be higher in the region of higher plastic strain.

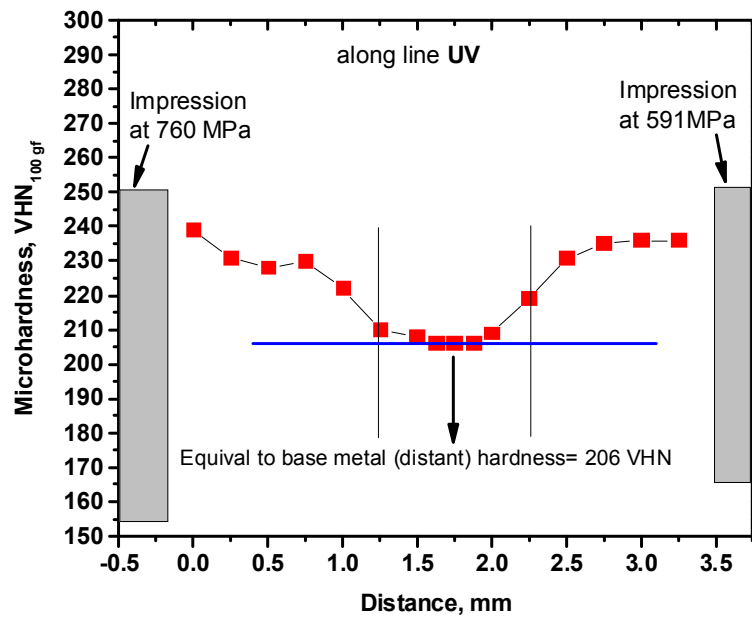


Fig. 4.31 Microhardness profile on the cross sectional surface along the line UV showing that there is no overlapping of the deformed zone of adjacent impressions.

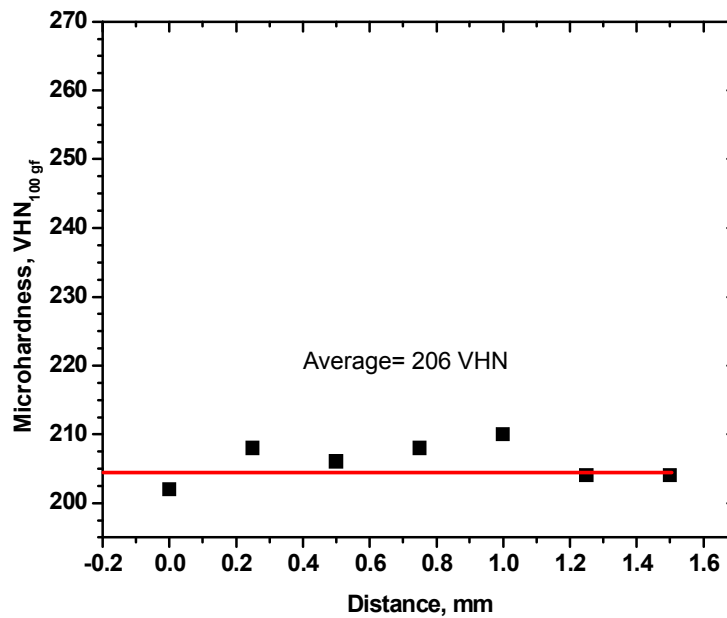


Fig. 4.32 Microhardness in the region far away from the impressions. The average hardness in this region was 206 VHN.

Figure 4.33 shows the microhardness variation along the line AB in the impression test corresponding to 760 MPa punching stress. Hardness profile was measured from the bottom of the impression to the bulk of the specimen in the loading direction. It was observed that at the bottom of the indentation the hardness was lower (211 VHN) and increased to a peak value (252 VHN) at a distance of 0.25 mm. From this peak value, hardness decreased to the base metal (distant) hardness at a distance of about 0.9 mm from the bottom edge of the indentation.

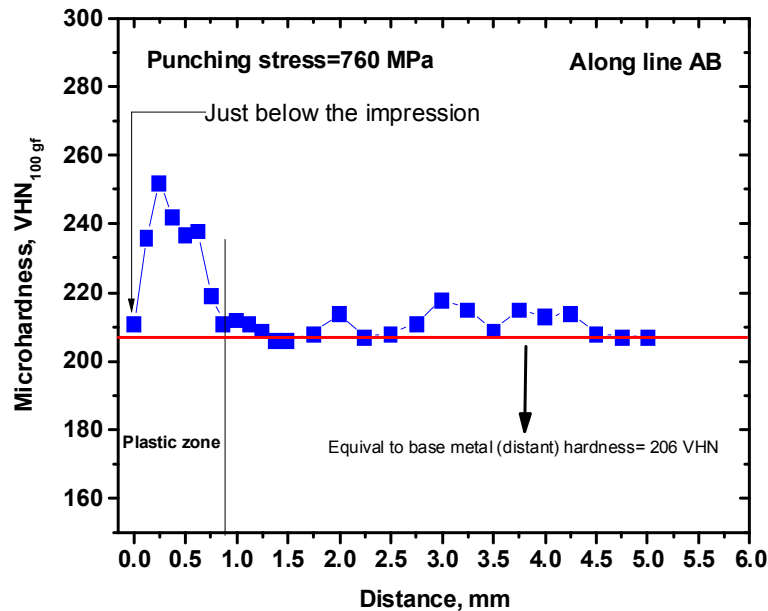


Fig. 4.33 Microhardness profile on the cross sectional surface along the line AB.

The hardness profile along the line CD and EF measured around the same impression is shown in Fig. 4.34. As can be seen, hardness decreased from a peak value of 280 VHN at the corner of the impression to a base value of 206 VHN at a distance of about 0.9-1.1 mm. The hardness of 280 VHN at the corner of the impression was found to be higher than the hardness of 211 VHN at the bottom of the indentation. This is because of the higher stress concentration at the corner of the impression due to the sharp edge

of the indenter. As a result, material in this region experiences a large plastic deformation and strain hardening.

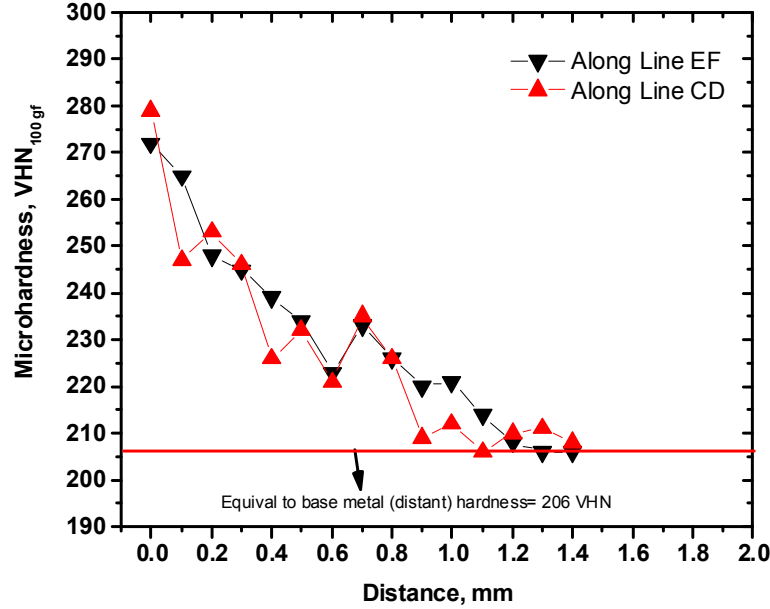


Fig. 4.34 Microhardness profile on the cross sectional surface along the line CD and EF.

From the above analysis, it is apparent that the size of the plastic zone is about 1 mm from the indentation. It can also be noted that the maximum plastic deformation occurs not at the indenter-specimen contact interface but within the material. Similar observations were found from the finite element analysis carried out by Yu and Li [2] which showed that the maximum Von Mises stress is not located directly under the punch but at a distance below it approximately equal to the radius of the punch. This analysis by Yu and Li [38] has been discussed in Chapter 2.

For further verification of this analysis, microhardness measurements were made along the line GH corresponding to a distance of 1.5 mm where the hardness was equal to the base value (206 VHN). Fig. 4.35 shows the hardness variation along this

line. Microhardness values along this line remained the same as the base value (206 VHN) supporting the above conclusion about the depth and the shape of the plastic zone.

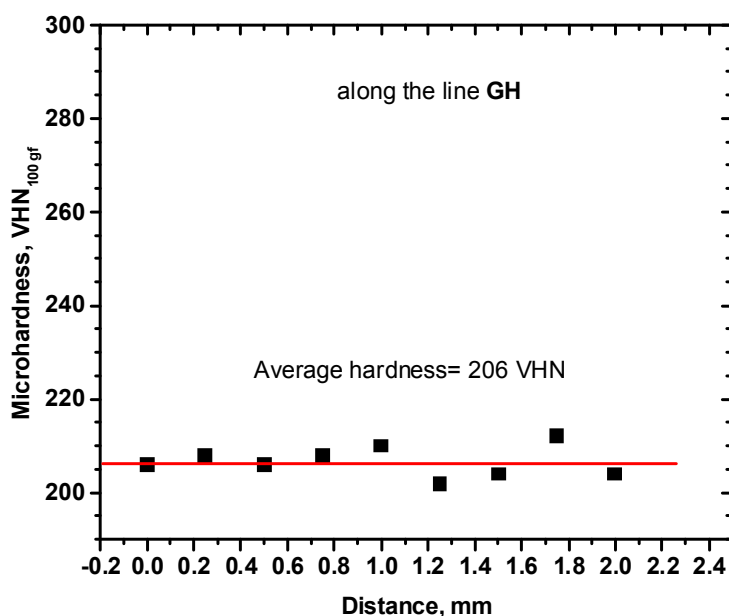


Fig. 4.35 Microhardness profile on the cross sectional surface along the line GH (horizontal line along 1.5 mm distance from indentation corresponding to 760 MPa).

Figure 4.36 shows the microhardness variation along the line WX corresponding to a distance of 0.25 mm (in Fig. 4.33). It was observed that the hardness value at 0.25 mm (252 VHN) decreased and reached the base value (206 VHN) and then increased as it reached the plastic zone of the adjacent impression corresponding to 591 MPa. This observation clearly shows that there is no overlapping of the plastic zones associated with two nearby impressions which would otherwise lead to determination of erroneous creep results. The centre to centre distance between the indentations was 4.8 mm.

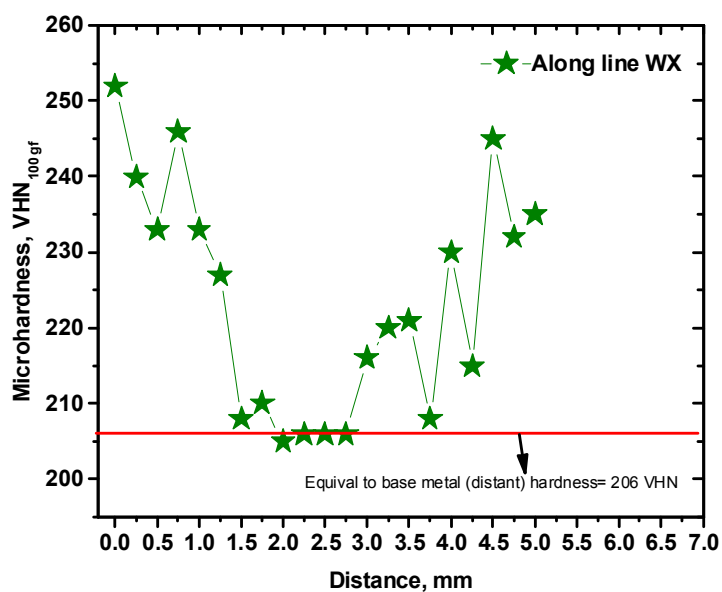


Fig. 4.36 Microhardness profile on the cross sectional surface along the line WX (line along 0.25 mm distance) between the two impressions corresponding to 760 MPa 591 MPa.

Similar studies were performed around the impressions at 591 MPa and 675 MPa. Figures 4.37 and 4.38 correspond to the impression at 591 MPa and Figs. 4.39 and 4.40 correspond to the impression at 675 MPa. The extension of the plastic zone was found to be about 1 mm and the shape of the plastic zone was hemispherical as observed for the previous impression (at 760 MPa).

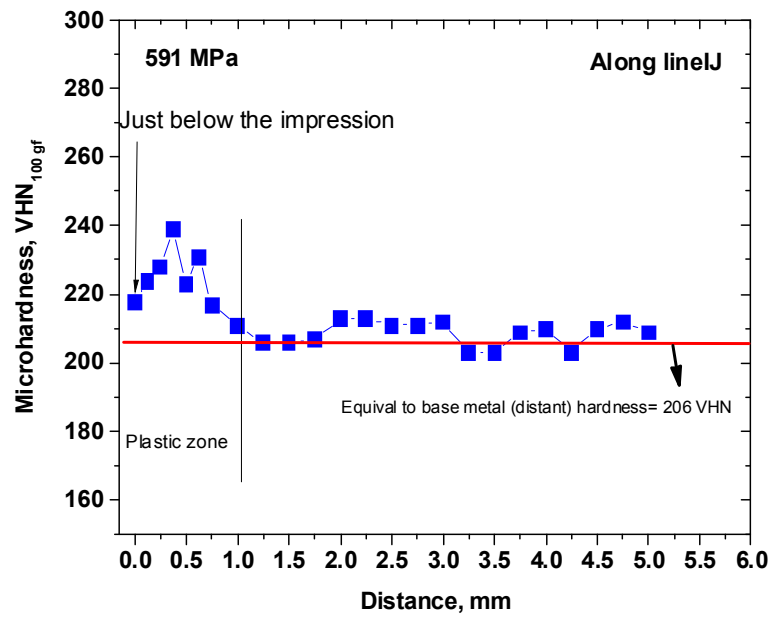


Fig. 4.37 Microhardness profile on the cross sectional surface along the line IJ in the loading direction in the vicinity of the impression at 591 MPa.

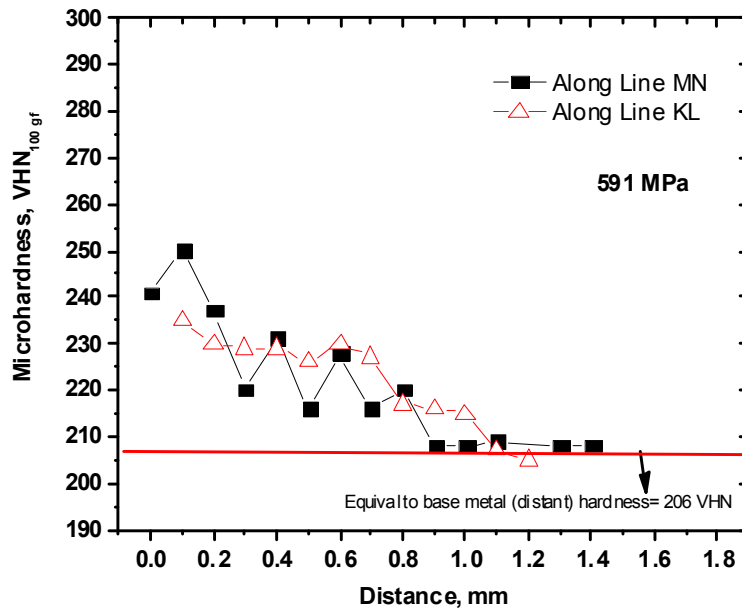


Fig. 4.38 Microhardness profile on the cross sectional surface along the line KL and MN in the vicinity of the impression at 591 MPa.

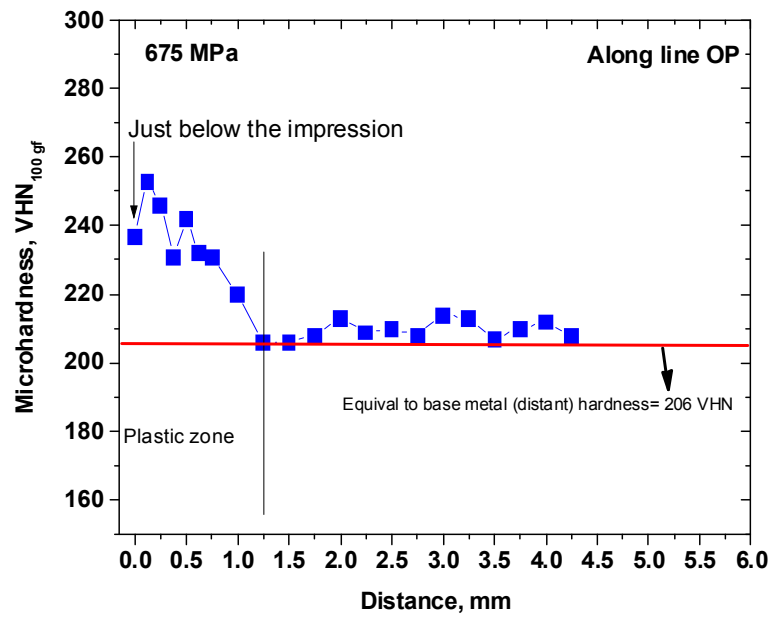


Fig. 4.39 Microhardness profile on the cross sectional surface along the line OP in the loading direction in the vicinity of the impression at 675 MPa.

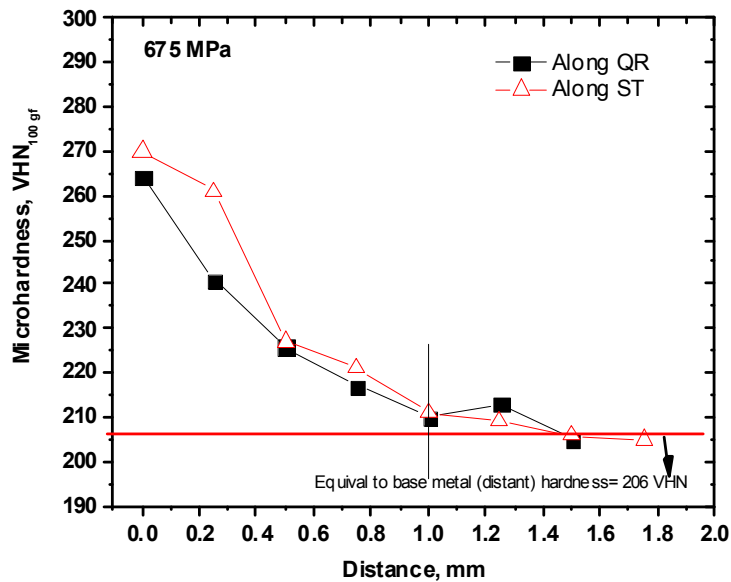


Fig. 4.40 Microhardness profile on the cross sectional surface along the line QR and ST in the vicinity of the impression at 675 MPa.

Thus the β value (in equation 4.6), which is referred to be the depth of the plastic zone beneath the indenter [30], was determined to be 1 from the microstructure and microhardness measurements, which can be used to convert the steady state impression velocity to an equivalent uniaxial steady state creep rate.

4.4.3 Surface Profilometry Studies

In any indentation tests, distance between the neighboring indentations plays a major role on the test results. It is essential to maintain the minimum distance between the adjacent impressions so that there is no interference of the plastic zone associated with the impressions. Despite the above described investigation concerning the plastic zone size, profilometry studies were also carried out to study material pile-up, its height and extension along the specimen surface for further understanding of the plastic zone and are described in the following sections.

4.4.3.1 Material Pile-up

During indentation process, accumulation of considerable amount material on the surface of the specimen around the indentation is termed as material pile-up. In the present study, a non-contact profilometer was employed to analyze the surface profile of the indentation on the test specimen. Fig. 4.41 shows the surface profile measured across the two adjacent impressions, one corresponding to 591 MPa and the other 760 MPa. A prominent material pile-up was observed on the surface of the specimen around the circumference of the indentation. During the penetration of the indenter, material beneath the indenter is initially displaced in the direction of loading. At the same time, large elastic region surrounding the plastic zone offers constraint to the flow of material. This resistance is generally termed as “constraint factor” as described in

Chapter 2 [31]. As a result of this elastic constraint offered by the large undeformed zone and to account for the continuing penetration of the indenter and resulting displacement of the material, the compressed material movement is directed upwards which appears as pile-up on the surface of the specimen around the indentation. The mechanics of material displacement in response to the indentation and the mechanism of material pile-up has been studied numerically by finite element method and is discussed in Chapter 6.

As can be seen from the profile, the pile-up height is more for the indentation with a larger depth of indenter penetration. In the case of indentation at 760 MPa, the depth of penetration was about 160 μm and the pile-up height was about 26 μm . Similarly, in the case of indentation at 591 MPa, the depth of penetration was about 90 μm and the pile-up height was about 15 μm . It indicates that the pile-up height is proportional to the depth of penetration. The effect of depth of penetration on the material pile-up height studied numerically is discussed in Chapter 6.

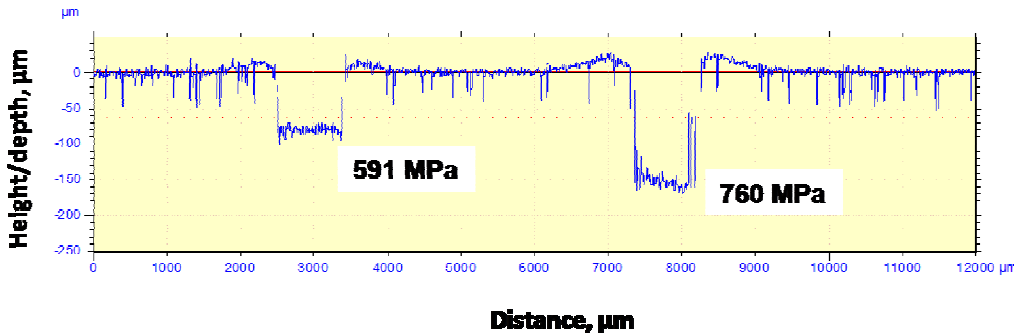


Fig. 4.41 Profilometry of the specimen surface depicting the material pile-up on the specimen surface in the vicinity of the impressions in 316LN SS containing 0.22 wt. % nitrogen.

4.4.3.2 Spacing between the Adjacent Indentations

The width of the pile-up on the specimen surface was estimated from the profile shown in Fig. 4.41. It was found that, for the impression corresponding to 760 MPa (depth about 160 μm) the width of the pile-up was about 980 μm and for the impression corresponding to 591 MPa (depth about 90 μm) the width of the pile-up was found to be 780 μm . The pile-up width was measured from the peak value of the pile-up. The pile-up was found to peak at a distance of about 250 μm from the edge of the indentation. Therefore, the total pile-up width from the edge of the indentation for the indentation corresponding to 760 MPa was about 1230 μm and for the impression corresponding to 591 MPa, it was 1030 μm . In this case, the centre to centre distance between the indentations was about 4800 μm . It can be noted that there is no overlapping of the material pile-up associated with adjacent indentations and hence no overlapping of the plastic zone.

The microhardness measurement made between the adjacent impressions shown in Figs. 4.31 and 4.36 showed no overlapping of the plastic zone associated with neighboring indentations. Based on the analysis of surface profilometry and microhardness measurement which confirmed no overlapping of the pile-up and the plastic zone between the adjacent indentations, the minimum centre to centre distance between adjacent indentations should be optimized to be at least more than five times the diameter of the indenter in order to avoid overlapping of the plastic deformation associated with adjacent indentations and thereby avoiding measurement of erroneous test results.

4.5 Conclusions

- Impression creep technique has been established and employed to characterize creep deformation behavior of 316LN SS as a faster and non-invasive method.
- Impression creep tests were carried out on 316LN SS containing 0.07, 0.11, 0.14 and 0.22 wt. % nitrogen in vacuum of 10^{-6} mbar at various temperatures and stress levels. The impression creep curves were characterized by a primary creep stage and a secondary stage. However, the tertiary stage that appears in conventional creep curves was absent.
- The equivalent steady state creep rates calculated from steady state impression velocities were found to be in close agreement with the steady state creep rates obtained from conventional uniaxial creep tests.
- The steady state impression velocity was found to increase with increasing punching stress. A power law relationship was found to be obeyed between steady state impression velocity and the punching stress in all the four heats. The power law exponent varied between 3.4 and 8.2 depending upon the nitrogen content in the heat.
- The temperature dependence of creep deformation in 316LN SS was investigated and the apparent activation energy for creep was determined to be 504 kJmol^{-1} .
- Based on the apparent activation energy and the stress exponent values, it is concluded that creep deformation is controlled by dislocation creep mechanism in 316LN SS.
- The influence of nitrogen on the creep deformation behavior of type 316LN SS was investigated at 923 K by employing impression creep technique as a faster and non-invasive method.

- Impression creep testing technique was found to be sensitive to capture the small variation in creep rate due to small variation in nitrogen content in the heats. The steady state impression velocity decreased with increasing nitrogen content. This result was found to be in good agreement with the results obtained from conventional uniaxial creep tests.
- A detailed characterization of the plastic zone in impression creep tests were carried out. The deformation under the indentation was inhomogeneous. The plastic zone in impression creep was found to be hemispherical in shape and the material in this hemispherical zone was found to experience extensive shear deformation. The size of the plastic zone was about 1 mm. Thus, the $\beta=1$, determined from the microstructure and microhardness measurements can be used to convert the steady state impression velocity to an equivalent uniaxial steady state creep rate (in equation 4.6). The β value is referred to be the depth of the plastic zone beneath the indenter [30].
- The minimum distance that should be maintained between the adjacent impressions was optimized to be at least 5 times the diameter of the indenter.

References

-
- [1] J. C. M. Li and S. N. Chu, J. Mater. Sci., 12 (1977) 2200-2208.
 - [2] H.Y. Yu and J. C. M Li, J. Mater. Sci., 12 (1977) 2214-2222.
 - [3] E. C. Yu and J. C. M. Li, Philos. Mag., 36 (1977) 811-825.
 - [4] D. Chiang and J. C. M. Li, J. Mater. Res. 9 (1994) 903-908.
 - [5] D. Dorner, K. Roller, B. Skrotzki, B. Stockhert, and G.Eggeler, Mater. Sci. Eng. A., 357 (2003) 346-354.
 - [6] L. Peng, F. Yang, J.Nie and J. C. M Li, Mater. Sci. Eng. A., 410-411 (2005) 42-47.

- [7] P. S. Gondavarti and K. Linga Murty, *J. Mater. Sci. Lett.*, **6** (1987) 456-458.
- [8] G. Nayyeri and R. Mahmudi, *Mater. Sci. Eng. A.*, **527** (2010) 2087-2098.
- [9] T.H. Hyde, K.A. Yehia and A.A. Becker, *Mat. High Temp.*, **13** (1995) 133-138.
- [10] S. N. G. Chu and J. C. M. Li, *J. Mater. Sci. Eng.*, **39** (1979) 1-10.
- [11] J. C. M. Li, *Mater. Sci. Eng. A.*, **322** (2002) 23-42.
- [12] Naveena and M.D. Mathew, in: K. Maruyama (Ed.), *Proceedings of the 12th International Conference on Creep and Fracture of Engineering Materials and Structures*, The Japan Institute of Metals, Kyoto, Japan, 2012, No. B18.
- [13] Naveena and M.D. Mathew, *Proc. 49th National Metallurgists' Day (NMD) and the 65th Annual Technical Meeting (ATM) of the Indian Institute of Metals (IIM)*, Hyderabad (2011).
- [14] M.D.Mathew, K. Laha and V. Ganesan, *Mater. Sci. Eng. A.*, **535** (2012) 76-83.
- [15] Naveena, P. Parameswaran, K. Laha and M. D. Mathew, *Mat. High. Temp.*, **31**(2) (2014) 180-184.
- [16] D. G. Morris and D. R. Harries, *Met. Sci.* **12**(1978) 525-531.
- [17] M.D.Mathew, G.Sasikala, Bhanu Sankara Rao and S.L.Mannan, *Mater. Sci. Eng. A.*, **148** (1991) 253-260.
- [18] J. G. Park and D.Y. Lee, *Scr. Met.* **29** (1993) 595-598.
- [19] G.E. Dieter, *"Mechanical Metallurgy"*, McGraw-Hill, London, 1988.
- [20] K. I. Hirano and Y. Iijima, in N. Igata and J. de Fouquet (eds.), *Proc. Jpn.-Fr. Semin. on Fundamental Aspects of Mechanical Properties and Microstructure Evolution of Stainless Steels at High Temperatures*, Tokyo, March 15-18, 1984, 1984, p. 26.
- [21] J. E. Bird, A. K. Mukherjee and J. E. Dorn, *"Correlations Between High-Temperature Creep Behavior and Structure"*, in: Haifa, Israel, D.G. Brandon and A.

Rosen (Eds.), Quantitative Relation Between Properties and Microstructure, 1969, p. 255-341.

[22] RCC-MR, 2007, Design and construction rules for mechanical components of nuclear installations, Section 2, Subsection Z.A3.3S.22.AFCEN, Paris.

[23] Naveena, V. D. Vijayanand, V. Ganesan, K. Laha and M. D. Mathew, Mater. Sci. Eng. A., 552 (2012) 112-118.

[24] M. D. Mathew, Trans. Indian Inst. Met., 63 (2010) 151-158.

[25] M. D. Mathew and V. S. Srinivasan, Mechanical Behavior of Nitrogen-bearing steels in Monograph on High Nitrogen Steels and Stainless Steels, U. Kamachi Mudali and Baldev Raj (Eds.), Narosa Publications, New Delhi, (2004) pp 182- 204

[26] V. Ganesan, M. D. Mathew and K. B. Sankara Rao, Mater. Sci. Technol., 25 (2009) 614-618.

[27] J. W. Simmons, Mater. Sci. Eng. A., 207 (1996) 159-169.

[28] A. Uguz and J.W. Martin, Mat. Character., 37 (1996) 105-118.

[29] ASTM E-384-89: Standard test method for microhardness of materials, Annual Book ASTM standard, 1.03, Eeston, MD, 1996

[30] D. H Sastry, Mater. Sci. Eng. A., 409 (2005) 67-75.

[31] D. Tabor, The Hardness of Metals, Clarendon Press, Oxford, United Kingdom, 1951.

CHAPTER 5

Application of Impression Creep Technique to Study Creep Behavior of Different Microstructural Zones of 316LN SS Weld Joint

5.1 Introduction

In the previous chapter, impression creep technique was employed as a faster and non-invasive method to characterize creep deformation behavior of different heats of 316LN SS under various stresses and temperatures. The technique was validated and usefulness of the technique in alloy development programme was demonstrated through a systematic study. In addition to the simplicity and time effectiveness of impression creep test technique, it is uniquely suitable for determining creep deformation characteristics of narrow microstructural zones in weld joints. Weld joints exhibit heterogeneity in microstructure and morphology. As a result, the different microstructural zones of a weld joint show a substantial variation in their creep properties. Uniaxial cross-weld creep rupture testing typically provides either an average property of the weld joint or the endurance of its weakest zone. The data obtained from uniaxial cross-weld creep rupture test alone is generally not sufficient to understand the creep behavior of a complete weld joint. Equally important is the understanding of creep properties of different microstructural zones of a weld joint. 316L(N) SS containing 0.02-0.03 wt.% carbon and 0.06-0.08 wt.% nitrogen has been used as a primary structural material for high temperature components in the India's prototype fast breeder reactor [1]. 316(N) SS is chosen as consumable electrode for welding structural components. In order to achieve a better creep strength of weld

joints, creep studies on a high nitrogen grade of 316L(N) SS containing 0.14 wt.% nitrogen welded with 316(N) SS electrodes containing 0.10 wt.% nitrogen are being carried out.

The present chapter deals with the investigation carried out on the creep behavior of narrow microstructural zones, namely, the heat-affected zone, the weld metal, and the base metal of a high nitrogen grade of 316L(N) SS weld joint using the impression creep technique.

5.2 316LN SS Weld Joint

316LN SS weld joint was prepared by multi-pass manual metal arc welding process. The base metal in the weld pad was 316LN SS containing 0.14 wt. % nitrogen. 316(N) SS containing 0.10 wt. % nitrogen was used as consumable electrode for welding. The details of the weld pad preparation, chemical compositions of the base metal and electrode, the typical weld joint on which impression creep tests were carried out have been given in Chapter 3. Figure 5.1 shows the schematic of weldpad configuration used in the present investigation.

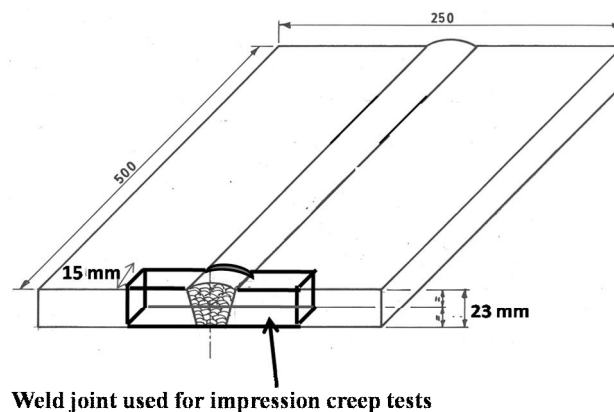


Fig 5.1 Schematic of the weld pad configuration used in the present investigation.

5.3 Identifying the Test Locations in Different Zones of the Weld Joint

To carryout impression creep tests on the narrow microstructural regions like heat-affected zone in the weld joint, care must be taken with respect to the following aspects.

- (i) To determine the exact location on which impression creep tests are to be conducted in this zone prior to impression creep testing.
- (ii) To exactly place the indenter on the determined location during assembling the indenter and specimen for the test to ensure that creep behavior of desired zone is assessed.

In the present investigation, to identify the region of heat-affected zone, the weld metal and the base metal, and to determine the exact locations for impression creep tests in these zones, the weld joint was etched electrolytically with 60 % nitric acid in 40 % distilled water. The analysis of the microstructure of the weld metal, the heat-affected zone and the base metal regions in the weld joint was carried out. Based on these micrographs, the exact test locations in each microstructural zone were marked on the test specimen. A replica of this weld joint with marked test locations was taken on a thin transparent sheet. Once the replica was taken the weld joint surface was again polished upto 1 μ m finish using diamond paste and then was used for impression creep tests. While conducting tests, the replica of the weld joint with all the marked locations on it was used for marking the exact locations on the polished specimen surface. The indenter and specimen were assembled such that the indenter is exactly placed on the respective locations.

5.4 Microstructure of Different Zones of the Weld Joint before Impression Creep Testing

The microstructure of the base metal, the heat-affected zone, and the weld metal was studied before impression creep testing using optical microscope and is depicted in Figs. 5.2, 5.3 and 5.4, respectively. Electrolytic etching using 60 % nitric acid in 40 % distilled water was carried out to reveal the microstructure.

Each zone was characterized by distinct microstructure and morphology. The base metal shown in Fig. 5.2 exhibited equiaxed grain structure. The heat-affected zone shown in Fig. 5.3 was found to have coarse grains. Figure 5.4 shows the typical microstructure of the weld metal which is a duplex structure consisting of austenite and δ -ferrite. The network of interconnected δ -ferrite was distributed uniformly in the austenite matrix.

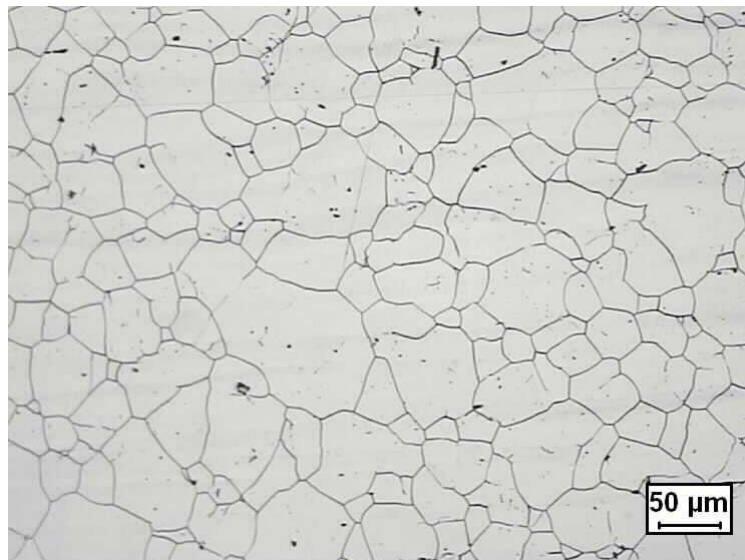


Fig. 5.2 Typical microstructure of the base metal of 316LN SS weld joint exhibiting equiaxed grain structure.

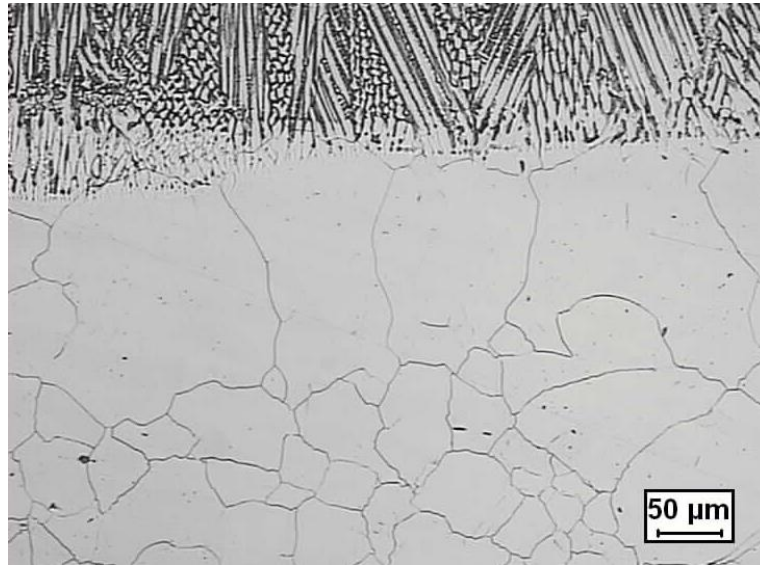


Fig. 5.3 Typical microstructure of the heat-affected zone of 316LN SS weld joint exhibiting coarse grains.

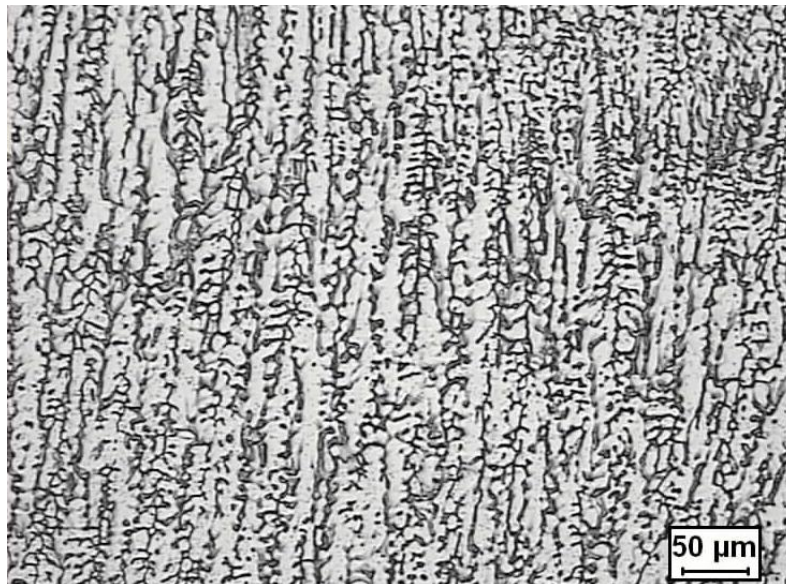


Fig. 5.4 Typical microstructure of the weld metal of 316LN SS weld joint exhibiting duplex structure of austenite and ferrite.

5.5 Microhardness of Different Zones of the Weld Joint before Impression Creep Testing

Microhardness measurement across the weld joint was taken to examine the microhardness variation in different zones. A Microhardness tester of model HMV-2 with a Vickers scale was used. A Load of 200 g was applied for 15 seconds on each microindentation. The microhardness profile measured across the weld joint is shown in Fig.5.5. The base metal had hardness of 218 VHN, whereas the weld metal and the heat-affected zone had a higher hardness of about 265 VHN. The high hardness of the weld metal and the heat-affected zone could be attributed to high dislocation density generated during multi-pass welding in these regions [2, 3]. After the hardness measurements, the weld joint was etched to exactly map the microhardness profile with the microstructural regions. The width of the heat-affected zone as estimated from the microhardness profile was about 3 to 4 mm. Point to be noted that two separate weld joints (from the same weld pad) were used for microhardness measurements and for impression creep tests

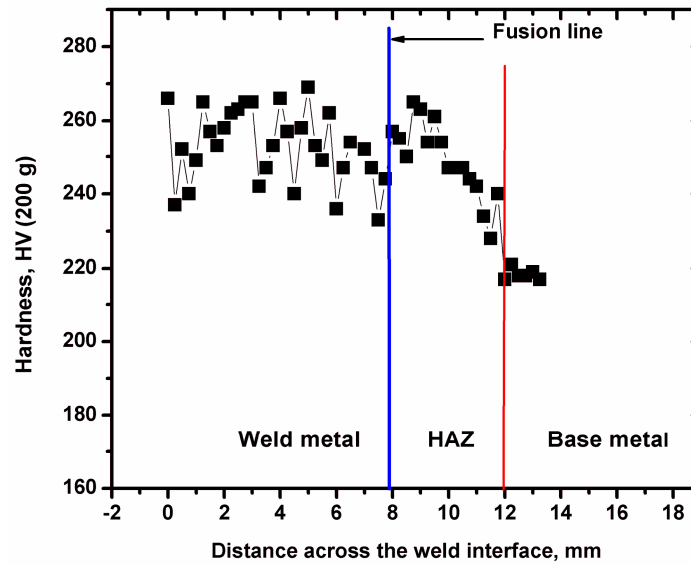


Fig. 5.5 Microhardness profile across the weld joint before creep testing.

5.6 Impression Creep Tests

Impression creep tests were carried out at 923 K on three distinct microstructural regions, namely, the heat-affected zone, the weld metal and the base metal, under the punching stress levels of 675 MPa and 760 MPa [4]. A constant load was applied to the test specimen of thickness 15 mm through a flat ended cylindrical indenter of diameter 1 mm. The temperature was maintained within $\pm 1^\circ\text{C}$ throughout the test. Vacuum of $\sim 10^{-6}$ mbar was maintained throughout the test in order to avoid the oxidation of the specimens.

5.7 Impression Creep Behavior of Different Microstructural Zones

Figures 5.6 and 5.7 show the typical depth of penetration versus time curves obtained for the weld metal, the base metal and heat-affected zone at 923 K under punching stress levels of 675 MPa and 760 MPa respectively. The impression creep curves of all the three different microstructural zones showed a trend characterized by a primary creep stage and a distinct steady state creep stage. The weld metal, the base metal and

the heat-affected zone exhibited distinct creep behavior. However, it is worth noting that all the three regions showed a consistent result at both the stress levels which reflects the consistency of the impression testing system.

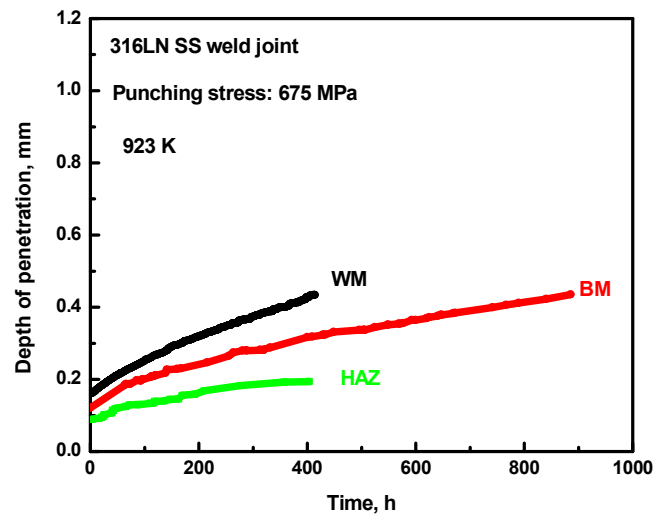


Fig. 5.6 Typical depth versus time curves for the weld metal, the base metal and the heat-affected zone of 316LN SS weld joint at 675 MPa.

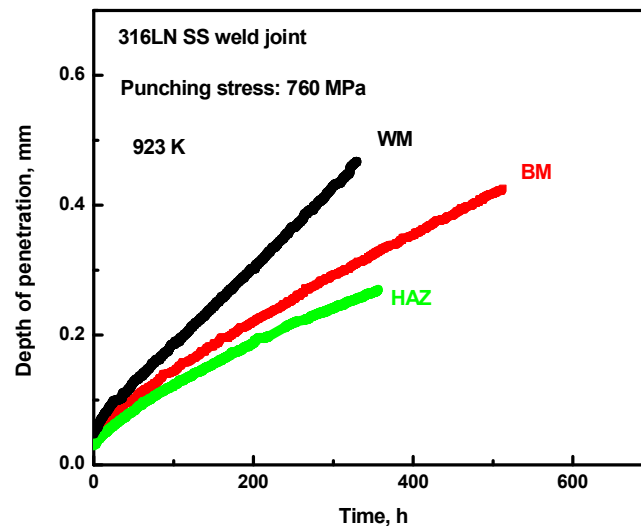


Fig. 5.7 Typical depth versus time curves for the weld metal, the base metal and the heat-affected zone of 316LN SS weld joint at 760 MPa.

Figures 5.8 and 5.9 show the variation of impression velocity with time for the weld metal, the base metal and the heat-affected zones at 923 K under punching stress levels of 675 MPa and 760 MPa respectively.

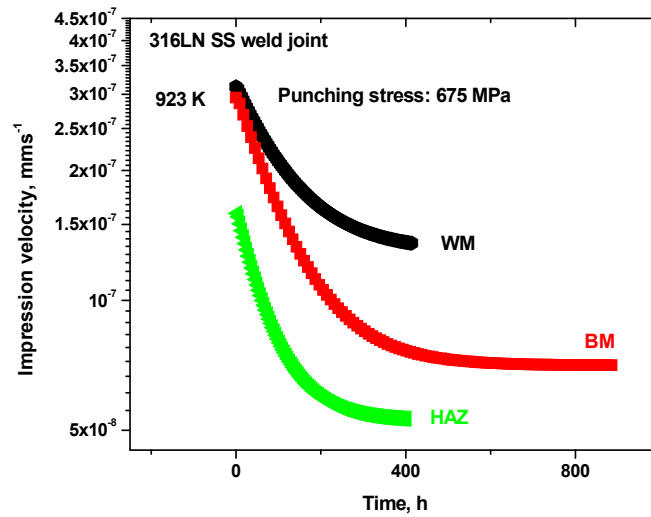


Fig. 5.8 Variation of impression velocity with test time showing the steady state impression velocity in the weld metal, the base metal and the heat-affected zone at 675 MPa.

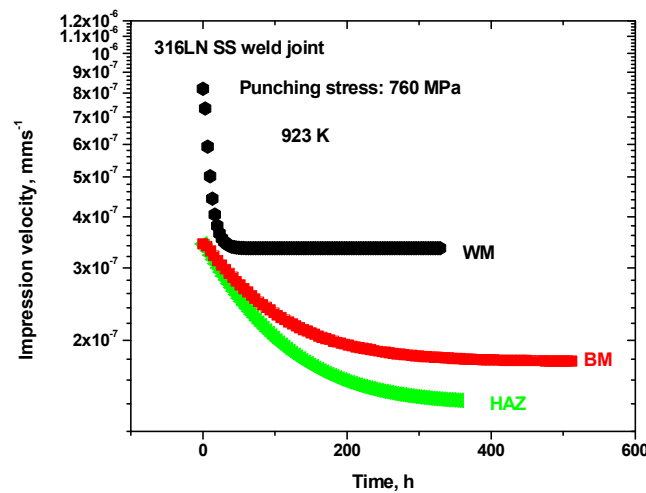


Fig. 5.9 Variation of impression velocity with test time showing the steady state impression velocity in the weld metal, the base metal and the heat-affected zone at 760 MPa.

Impression velocity was found to decrease initially with time and then attain a constant value indicating a true steady state creep stage. Heterogeneity in microstructure and morphology of the weld metal, the base metal and the heat-affected zone is reflected in the variation of steady state impression velocity.

Weld metal region showed a higher steady state impression velocity than the base metal and the heat-affected zone which indicates its lower creep strength. The heat-affected zones were found to have the lowest steady state impression velocity. These observations can be rationalized based on the differences in the microstructure and morphology of three distinct regions, and also on the basis of presence of δ -ferrite in the weld metal. The presence of δ -ferrite in the austenite matrix of the weld metal was found to increase the steady state creep rate of the weld metal due to i) the more open bcc crystal structure of δ -ferrite which offers an easier path for diffusion, ii) the δ - γ interfaces which enhances the diffusion by acting as an effective path for diffusion [5].

The heat-affected zone was found to have the lowest creep rate when compared with the base metal and the weld metal. One of the reasons for the lowest creep rate exhibited by the heat-affected zone could be attributed to the coarse grains present in the heat-affected zone as can be seen from Fig.5.3. The grain size in the heat-affected zone was about 150 μm . The influence of polycrystal grain size on the steady state creep rate, investigated by several researchers in different materials [6, 7, 8], showed that the steady state creep rate decreases with increasing grain size. However, in the present case the width of the coarse grain heat-affected zone (about 300 μm) is smaller than the diameter of the indenter which is 1000 μm (1mm). Therefore, the influence of coarse grains on creep deformation behavior could be minimal. Another reason for the

lowest creep rate could be that during multipass welding process the heat-affected zone is subjected to a number of thermal cycles which induce high dislocation density in this region. Etienne et al. [2] studied the dislocation structure in the heat-affected zone of AISI 316 steel weld joints. The presence of dislocations pinned by the precipitates was reported to decrease the steady state creep rate of the heat-affected zone. The creep behavior of the weld metal, the base metal and the heat-affected zone, characterized from impression creep tests in our investigation, was found to be consistent with the creep behavior of the weld metal, the base metal and the heat-affected zone of AISI 316 steel weld joints characterized from uniaxial creep tests by Etienne et al. [2]. The heat-affected zone had the lowest creep rate, and weld metal the highest creep rate when compared to the base metal. The difference in creep behavior showed by each zone was found to have been caused by the difference in the microstructures exhibited by individual zone. The creep curves of the weld metal, the base metal and the heat-affected zone, characterized by Etienne et al. [2] is shown in Fig. 5.10.

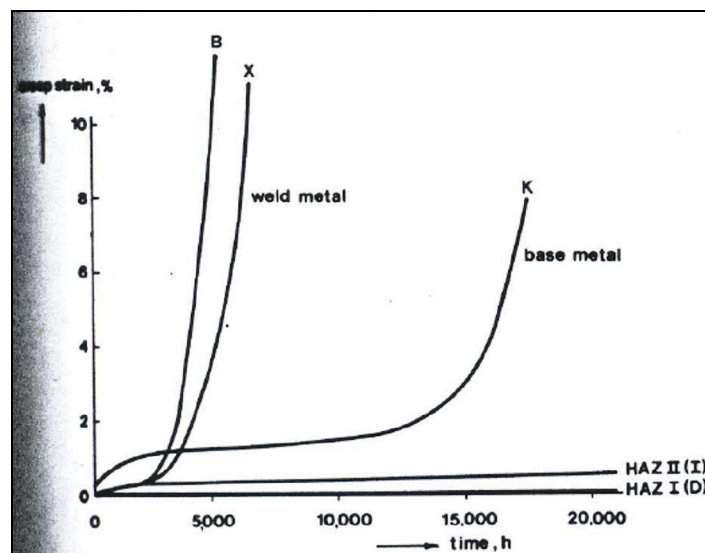


Fig. 5.10 Creep curves for the weld metal, the base metal and the heat-affected zone obtained from conventional uniaxial creep tests after Etienne et al. [2].

5.8 Comparison of Impression and Uniaxial Creep Data

In order to corroborate the validity of the impression creep technique, the data obtained from impression creep tests were compared with the data obtained from conventional uniaxial creep test for base metal and weld metal. The punching stresses and the steady state impression velocities in impression creep were converted to equivalent uniaxial stresses and uniaxial steady state creep rates using Eqs.(4.5) and (4.6) respectively (see Chapter 4). Figures 5.11 and 5.12 show the correlation between uniaxial steady state creep rate and equivalent steady state creep rate obtained from impression creep tests for the weld metal and the base metal respectively. A good correlation was established between impression creep test results and the uniaxial creep test results. The uniaxial creep data for the base metal (316LN SS containing 0.14 wt. % nitrogen) was referred from the work published by Mathew et al.[9].

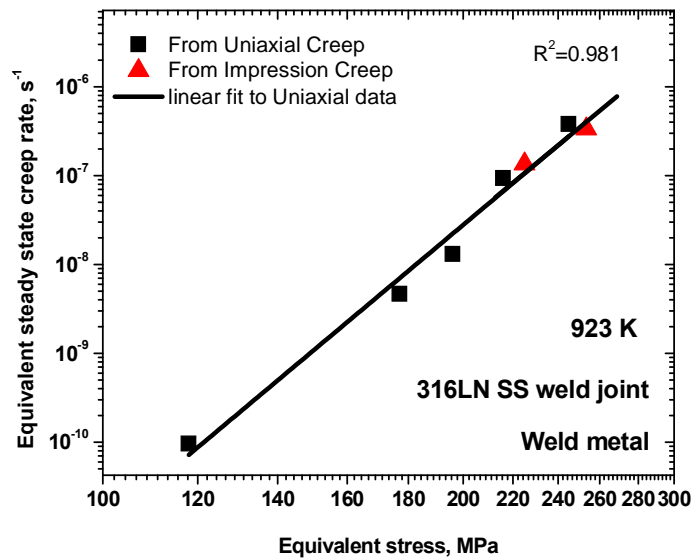


Fig. 5.11 Comparison of steady state creep rate obtained from conventional uniaxial creep tests and impression creep tests on the weld metal.

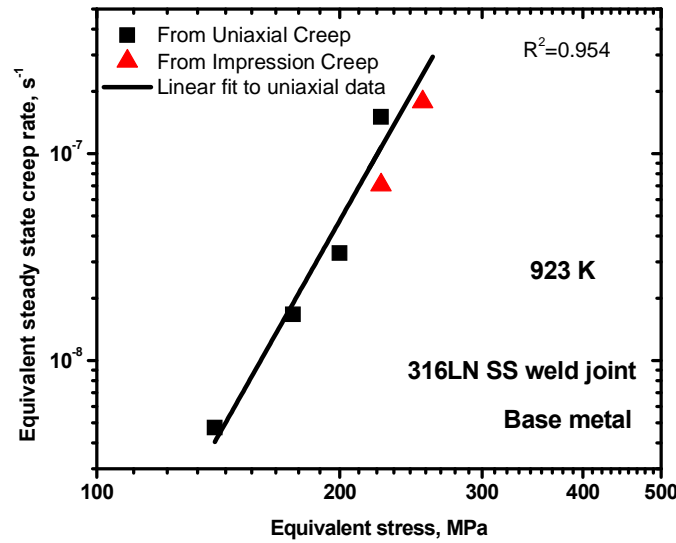


Fig. 5.12 Comparison of steady state creep rate obtained from conventional uniaxial creep tests and impression creep tests on the base metal.

5.9 Microstructural Evolution in Different Zones

Microstructural evolution during impression creep in the vicinity of impressions in the base metal, the heat-affected zone and the weld metal was studied at both the stress levels of 675 and 760 MPa. Similar procedure as was followed for cross sectional microstructural analysis in the case of 316LN SS base materials (Chapter 4) was followed in this case.

The micrographs shown in Figs. 5.13, 5.14 and 5.15 correspond to 675 MPa and those shown in Figs. 5.16, 5.17 and 5.18 correspond to 760 MPa. As was observed in the case of base materials three distinguishable regions which are indicated with numbers 1, 2 and 3 were observed in all the three microstructural zones of the weld joint. In order to distinguish these three regions clearly, curved lines were drawn. In region 1 which is just below the punch, no significant change in grain shape was

detected (in the base metal and heat affected zone). This indicates that the stress in this region may be hydrostatic in nature. Similar observations on the presence of a hydrostatic zone was reported in SiC partial-MoSi₂ composite material by Butt et al. [10] and in cast Magnesium alloy by Mahmudi and co workers [11]. The material in region 2 experienced an extensive shear deformation, more so the material at the corner of indentation. It can be observed that the grains in this region are elongated to a greater extent indicating a larger plastic deformation in region 2. No change in shape of grains in the region 3 which is far away from the indentation were observed which indicates the absence of plastic deformation in this region. In weld metal shown in Figs. 5.15 (a)-(b) and 5.18 (a)-(b), region 2 experienced a larger deformation than the region 1 and 3. This is evidenced by breakage of interconnected vermicular morphology of δ -ferrite which was pronounced in region 2.

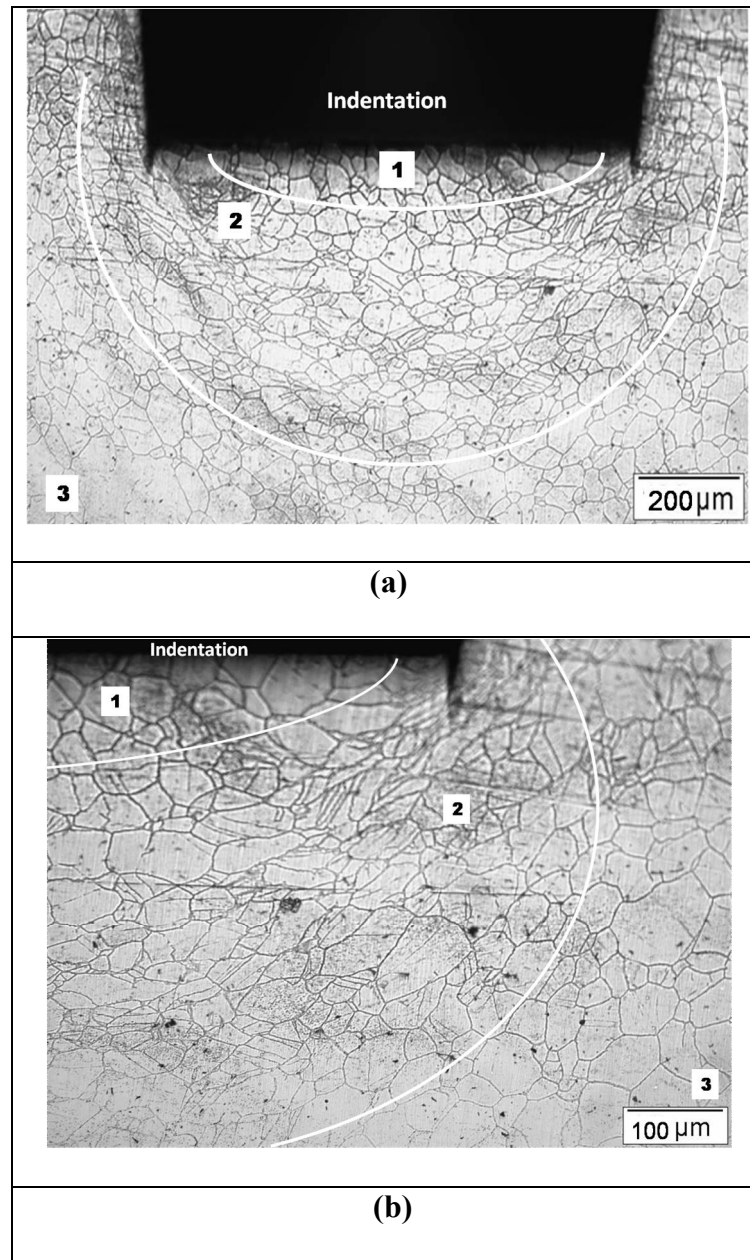


Fig. 5.13. Optical micrographs of impression creep regions in the base metal at 675 MPa: (a) three distinct regions in the vicinity of the impression, and (b) right corner of the impression showing extensive deformation in region 2.

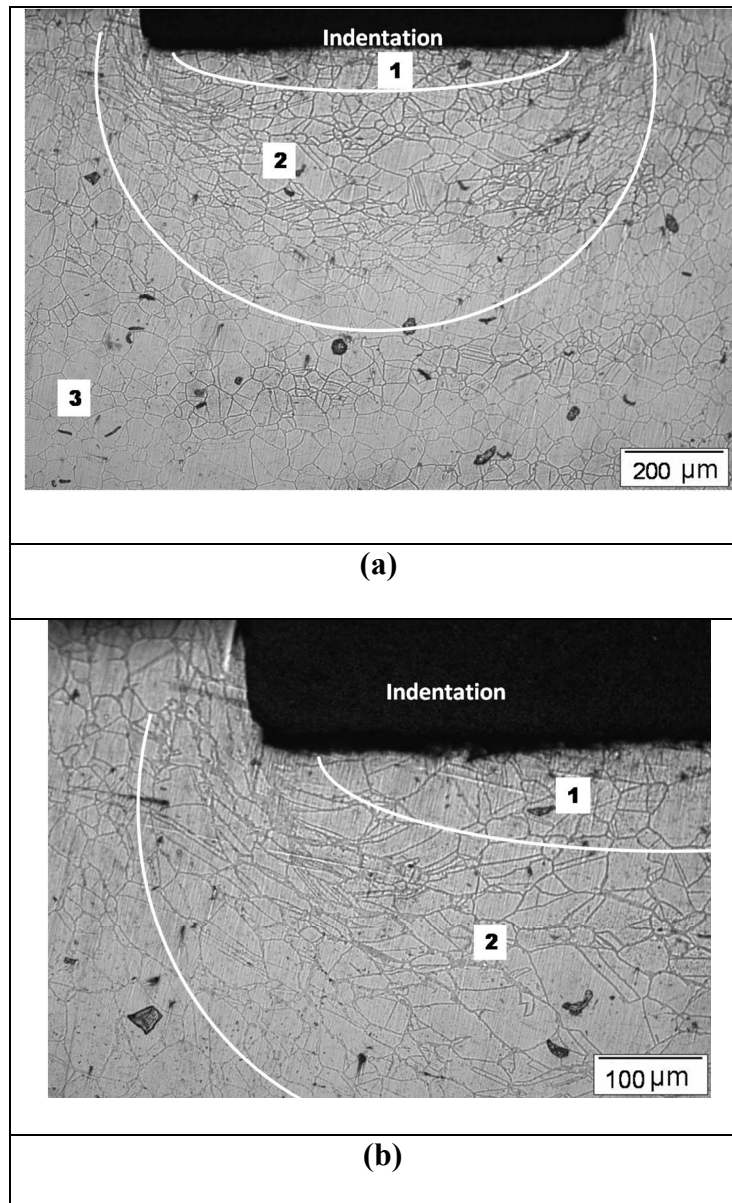


Fig. 5.14. Optical micrographs of impression creep regions in the heat-affected zone at 675 MPa: (a) three distinct regions in the vicinity of the impression, and (b) left corner of the impression at a higher magnification showing extensive deformation in region 2.

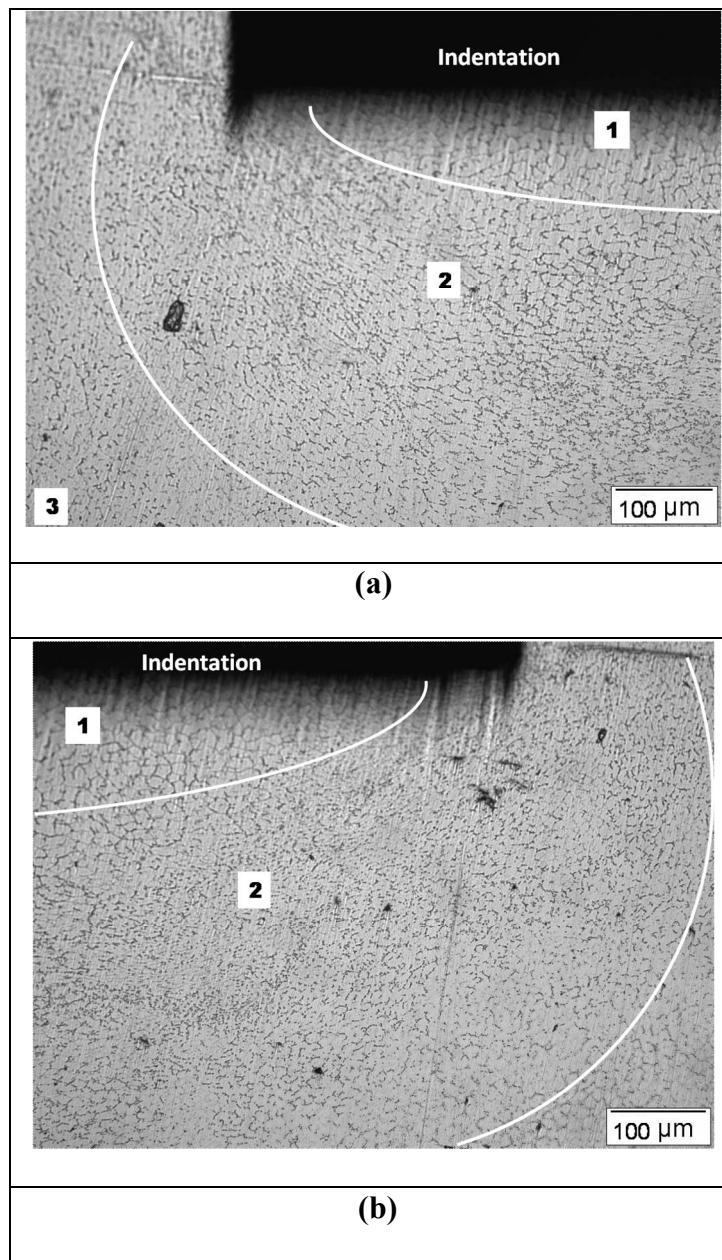


Fig. 5.15. Optical micrographs of impression creep regions in the weld metal at 675 MPa: (a) left corner of the impression, and (b) right corner of the impression showing three distinct regions and extensive deformation in region 2.

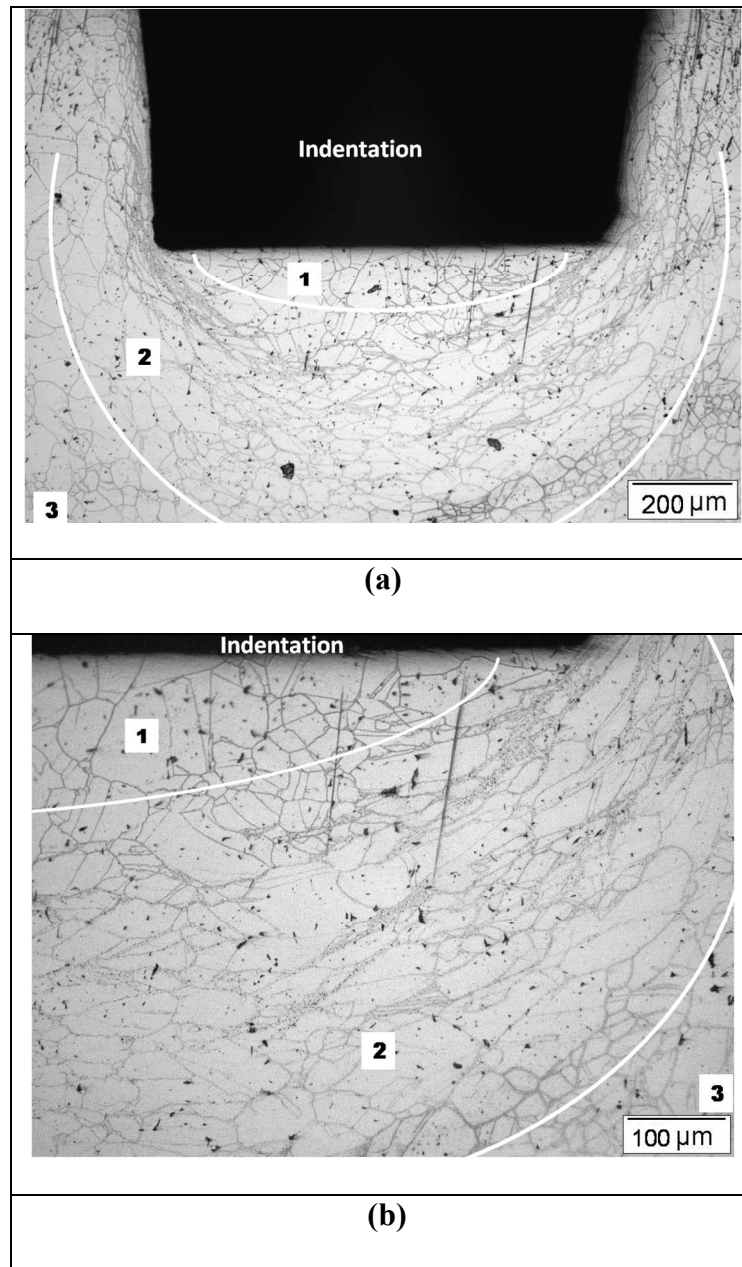


Fig. 5.16. Optical micrographs of impression creep regions in the base metal at 760 MPa: (a) three distinct regions in the vicinity of the impression, and (b) right corner of the impression showing extensive deformation in region 2.

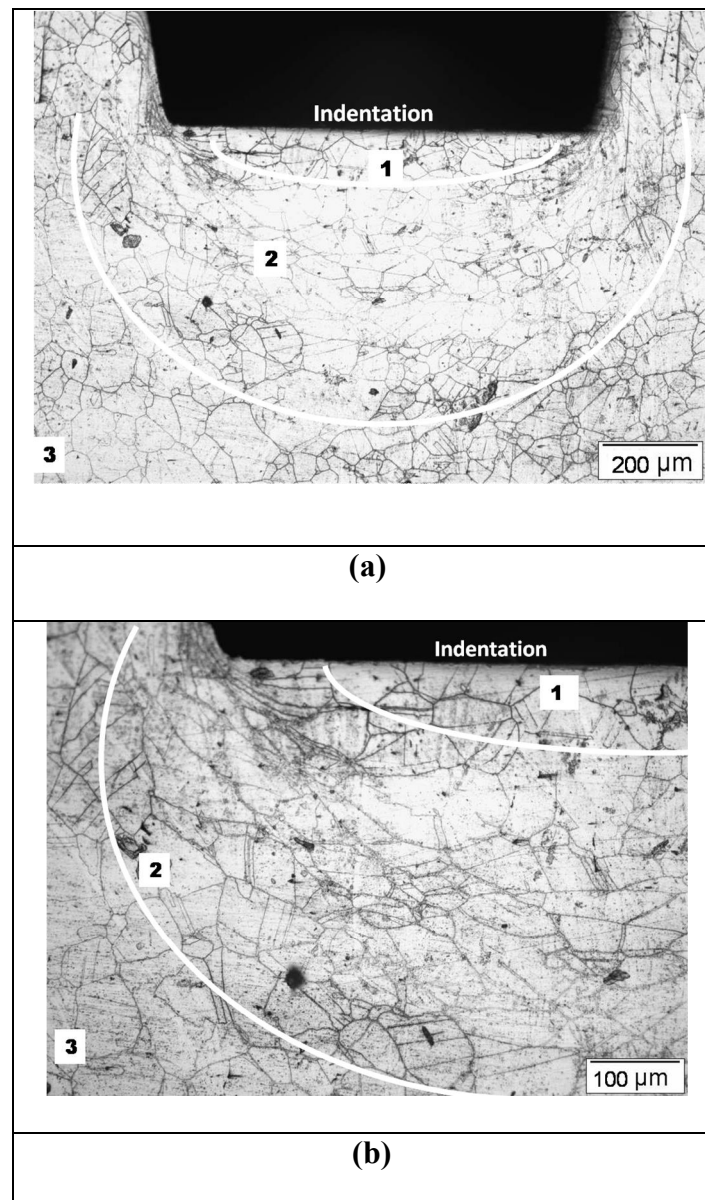


Fig. 5.17 Optical micrographs of impression creep regions in the heat-affected zone at 760 MPa: (a) three distinct regions in the vicinity of the impression, and (b) a higher magnification micrograph showing extensive deformation of grains in region 2.

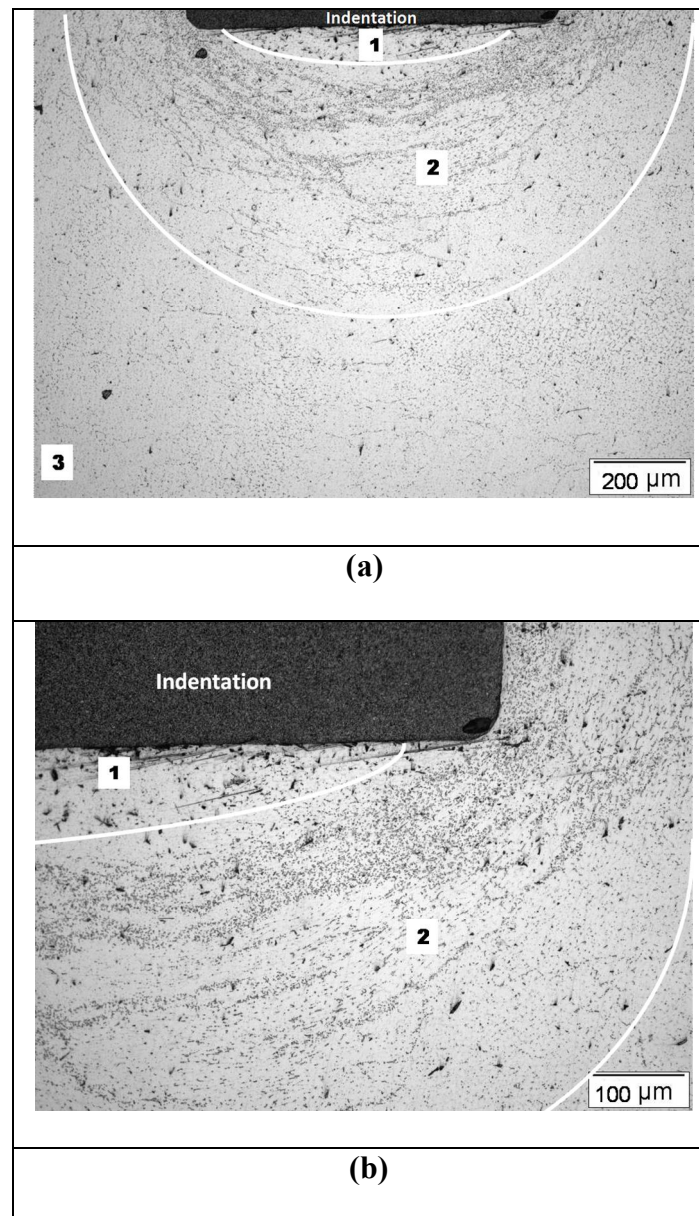


Fig. 5.18. Optical micrographs of impression creep regions in the weld metal at 760 MPa: (a) three distinct regions in the vicinity of the impression, and (b) right corner of the impression at a higher magnification showing extensive deformation in region 2.

5.10 Conclusions

- Impression creep technique was employed to characterize creep behavior of distinct microstructural regions such as the weld metal, the heat-affected zone and the base metal in a high nitrogen grade of 316LN SS weld joint at 923 K, under punching stress levels of 675 MPa and 760 MPa.
- The three distinct zones of the weld joint showed difference in creep behavior. The weld metal exhibited higher steady state impression velocity which is indicative of higher creep rate and relatively lower creep strength.
- The heat-affected zone was found to have the lowest steady state impression velocity compared to the base metal and the weld metal.
- Differences in creep behavior of various zones was attributed to the difference in the microstructure and morphology exhibited by the individual zone.
- A good correlation between impression and conventional uniaxial creep data for the weld metal and the base metal was established.
- The analysis of the microstructural evolution during impression creep could provide an insight to understanding the state of stress/strain field in the vicinity of impressions under the punch.
- Impression creep technique was proved to be an efficient material non-invasive technique uniquely suitable to characterize creep deformation behavior of narrow microstructural zones of weld joints which is not possible to characterize from conventional uniaxial cross-weld creep testing.

References

-
- [1] S. L. Mannan, S. C. Chetal, B. Raj and S. B. Bhoje, Trans. IIM., 56 (2003) 155-178.
- [2] C. F. Etienne, O. Rossum and F. Roode, "Creep of welded joints AISI 316", Proc. Int. Conf. on Engineering aspects of creep, University of Sheffield, UK, 2 (1980) 113-121.
- [3] P. Marshall: "Austenitic Stainless Steels: Microstructure and Mechanical Properties", 1984, New York, Elsevier Applied Science.
- [4] Naveena, V.D. Vijayanand, V. Ganesan, K. Laha and M.D. Mathew, Mater. Sci. Tech., 30(2014) 1223-1228.
- [5] G. Sasikala, M. D. Mathew, K. Bhanu Sankara Rao and S. L. Mannan, J. Nucl. Mater., 273 (1999) 257-264.
- [6] F. Garofalo, W. F. Domis and F. Von Gemmingen: Trans. AIME., 230 (1964) 1460-1467.
- [7] G. S. Al-Ganainy and M. T. Mostafa, Egypt. J. Sol., 23 (2000) 333-340.
- [8] S. L. Mannan and P. Rodriguez, Met. Sci., 17 (1983) 63-69.
- [9] M. D. Mathew, K. Laha and V. Ganesan, Mater. Sci. Eng. A., 535(2012) 76-83.
- [10] D. P. Butt, D. A. Korzekwa, S. A. Maloy, H. Kung and J. J. Petrovic, J. Mater. Res., 11(1996) 1528-1536.
- [11] F. Kabirian and R. Mahmudi, Metall. Mater. Trans A., 40 (2009) 116- 127.

CHAPTER 6

Finite Element Analysis of Impression Creep Deformation Behavior of 316LN SS

6.1 Introduction

In the preceding chapters, detailed experimental investigations on the characteristics of the plastic zone developed in impression creep tests in 316LN SS, using various characterization techniques, have been discussed. The present chapter is focused on understanding the mode of material deformation and flow behavior in impression creep by finite element modeling and simulation studies. An axisymmetric finite element model of indenter-specimen system has been developed using commercial ABAQUS finite element analysis software. FE simulation of impression creep process has been carried out on 316LN SS. This chapter discusses the analyses of the stress distribution under the punch and its evolution during different stages of indentation process, the size and shape of the resulting plastic zone, the dynamics of material flow in response to the indentation and the mechanism of material pile-up on the specimen surface.

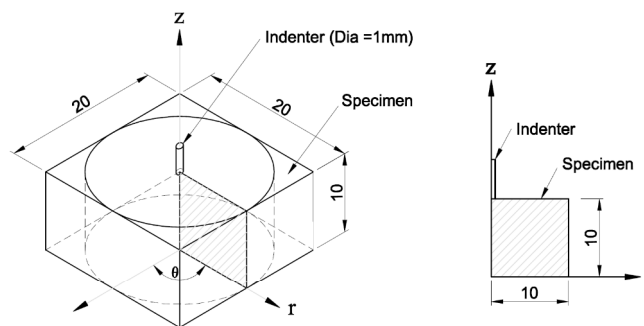
6.2 Finite Element Analysis of Impression Creep Deformation

The impression creep deformation process is associated with a complex multi-axial stress/strain field in the vicinity of the indentation which varies continuously during the indentation process. The deformation in the specimen below the punch is highly inhomogeneous [1,2]. This has been observed experimentally which is discussed in the previous chapters. The stress field around purely elastic indentations by different geometries of indenters (spherical, pyramidal, conical, and cylindrical) can be

described analytically [3, 4, 5, 6]. However, when the material response to the indentation is elastic-plastic or elastic-plastic-creep, the analysis of deformation becomes much more complex and no analytical solution exists to describe these material responses [7]. Therefore, to understand the material flow behavior in the case of elastic-plastic-creep processes, numerical analysis is essential. Rapid advancement in computational mechanics over the past decade has produced the means to analyze the mechanical properties of materials or components under fully non-linear plastic conditions. Sophisticated computer codes such as ABAQUS, ANSYS etc have been developed which enable finite element modeling of non-linear deformation processes like creep. In the present study, finite element analysis was carried out using ABAQUS finite element analysis software.

6.2.1 Axisymmetric Model of Impression Creep Test

Impression creep test model exhibits axisymmetry in geometry, loading and the boundary conditions. Hence, an actual three-dimensional impression creep problem can be solved as an axisymmetric problem. Figure 6.1 illustrates schematically how an actual 3-Dimensional impression creep problem is simplified as an axisymmetric problem.



Note: All dimensions are in mm.

Fig. 6.1 Schematic illustration of an actual 3-Dimensional impression creep model and its simplified axisymmetric model.

6.2.2 Finite Element Model Description

6.2.2.1 FE Model and Meshing

The FE model developed for the simulation of impression creep test is an axisymmetric model of a flat-ended cylindrical indenter of radius 0.5 mm in contact with a flat specimen of size 10 mm x 10 mm x 10 mm. The impression creep specimen was made of 316LN SS and was modelled as a deformable body. The indenter was made of tungsten carbide which is much stiffer than the stainless steel specimen was therefore modeled as a perfectly rigid body. A reference point was assigned on the top of the indenter, on the axis of symmetry, which manipulates the rigid body translation of the indenter. The rigid indenter surface was assigned as the master surface and the deformable specimen surface was assigned as the slave surface. Frictionless finite surface-to-surface sliding contact was defined between the bottom of the indenter geometry and top of the specimen. In the case of flat-ended cylindrical indenter, on account of the sharp corner of the indenter, a large stress concentration occurs at the circumference of the indenter (corner of the indentation). Hence, to avoid the convergence problem arising from this, a small fillet of radius 0.07 mm was created at the circumference of the indenter. Fig.6.2 shows the FE model for simulation of the impression creep test.

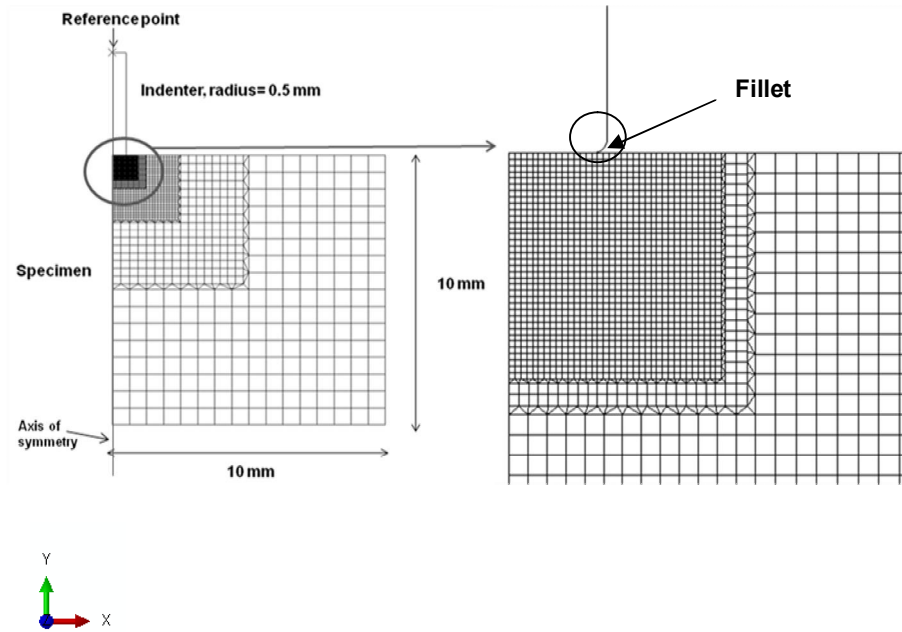


Fig. 6.2 An axisymmetric FE model and FE mesh which consists of linear quadrilateral elements with reduced integration of type CAX4R and linear triangular elements of type CAX3.

The finite element mesh shown in Fig.6.2 comprised of linear quadrilateral elements with reduced integration of type CAX4R and linear triangular elements of type CAX3. CAX4R type elements are recommended for problems involving large stress gradient due to stress concentrations. A finer mesh was adopted in the immediate neighborhood of the punch-specimen contact so that the large deformation and high stress gradients can be precisely analyzed. The mesh size was increased progressively away from the contact region in order to reduce the total size of the model without compromising the accuracy of the results. Optimization of the size of the finer mesh near the indenter-specimen contact region has been carried out and is discussed in the later sections.

6.2.2.2 Material Properties

In the present analysis, impression creep tests were simulated for specimens made of 316LN SS which contains 0.14 wt. % nitrogen. The elastic, plastic and creep properties of this alloy at a temperature of 923 K were used as input material properties in the simulation. These material properties are described below.

6.2.2.2.1 Elastic Property

The stress-strain relation that describes elastic behavior of the material is given by the Hooke's law. This equation was used in the present simulation to describe the material property in the elastic regime. The equation is given by,

$$\sigma = \varepsilon_{el} E \quad (6.1)$$

where the σ is the uniaxial stress, ε_{el} is the elastic strain and E is the Young's modulus of the material which is constant for a material at a given temperature. The material in the present model was considered as an isotropic material. The analysis was performed at a temperature of 923 K. The Young's modulus of 147 GPa corresponding to this temperature and the Poisson's ratio of 0.3 were considered [8].

6.2.2.2.2 Plastic Property

True stress- true plastic strain data obtained from uniaxial tension test for this material at 923 K was used to define the plastic behavior of the material [9]. The range of data from yield strength to ultimate tensile strength was considered.

6.2.2.2.3 Creep Property

The creep analysis was carried out under the steady state condition. The Norton power-law constitutive equation was used as a flow rule for the creep deformation of each element in the model. The power law is given,

$$\dot{\varepsilon} = A \sigma^n \quad (6.2)$$

where $\dot{\varepsilon}$ is the steady state strain rate, σ is the stress, n is the stress exponent and A is the power law coefficient. The A and n value for this alloy are given in Table 6.1[10].

Material	A	n
316LN SS containing 0.14 wt. % nitrogen	8.4569×10^{-22}	7.5734

Table 6.1 Input creep properties for 316LN SS.

The abovementioned power law was used in its strain hardening form which was used to define the creep properties and is given by [11],

$$\dot{\varepsilon}^{cr} = (A \tilde{q}^n [(m+1) \bar{\varepsilon}^{cr}]^m)^{\frac{1}{m+1}} \quad (6.3)$$

where, $\dot{\varepsilon}^{cr}$ is the uniaxial equivalent creep strain rate, $\bar{\varepsilon}^{cr}$ is equivalent creep strain, \tilde{q} is the uniaxial equivalent deviatoric stress, and A , n and m are constants which depends on temperature.

6.2.2.3 Analysis Steps, Boundary Conditions, Loading and Simulations

The numerical simulations of impression creep tests were performed by incorporating two main steps, namely, the initial step and the analysis step. In the initial step, the boundary conditions, output fields and interactions properties were defined and the same were retained in the subsequent analysis step. The analysis step is further divided into two steps, namely, the plastic step and creep step. A static type analysis which includes the effects of non-linearity was used during the plastic step. A visco-analysis procedure was used for carrying out creep analysis in the creep step. Essential parameters such as increment size, the number of increments and the time periods were assigned for each of these steps accordingly so that the solution is converged.

The following displacement boundary conditions were imposed on the indenter-specimen assembly. The displacement of the nodes in the specimen and the reference point on the indenter were constrained along the axisymmetric axis, i.e.,

$$u_x=0; \text{ (along the axisymmetric axis)} \quad (6.3)$$

This allows the indenter to move only in the axial direction (y-direction) and no sliding of the indenter in its radial direction (x-direction). The nodes at the bottom of the specimen were constrained such that there was no displacement of nodes in the axial direction along the bottom line of the specimen.

$$u_y=0; \text{ (on the bottom surface of the specimen)} \quad (6.4)$$

In the plastic step, concentrated force type load in the range of 370 to 600 N was applied at the reference point on the rigid indenter. This range of load corresponds to the punching stress range 400-800 MPa. This load was held constant in the creep step and the simulation was run for sufficiently long (up to 1000 h) creep time.

6.3 FEA Results and Discussion

6.3.1 Optimization of the Mesh Size

The mesh in FE model influences the accuracy, convergence and speed of computation. In the present study, prior to the FE simulations, a mesh convergence test was performed to assess the sensitivity of the mesh size on the FEA results. The element size near the indenter specimen contact region which experienced large deformation was varied upto an optimum size of 30 μm . It was found that the difference in the magnitude of Von Mises stress and the depth profile by reducing the element size (i.e., $< 30 \mu\text{m}$) was insignificant. The two meshes with mesh sizes 30 μm and 7 μm are shown in Fig. 6.3. Typical Von Mises stress variations along the axial and radial directions for the mesh with element size 30 μm and less are shown in Figs. 6.4 and

6.5, respectively. Typical depth profiles for these element sizes are shown in Fig. 6.6 which exhibited negligible difference in their profiles. With a view to reduce the computational time, the mesh size near the indenter-specimen contact region was optimized to $30\text{ }\mu\text{m}$ and in the region away from the indenter-specimen contact the mesh size was kept progressively coarser. The number of elements in the model was 2506.

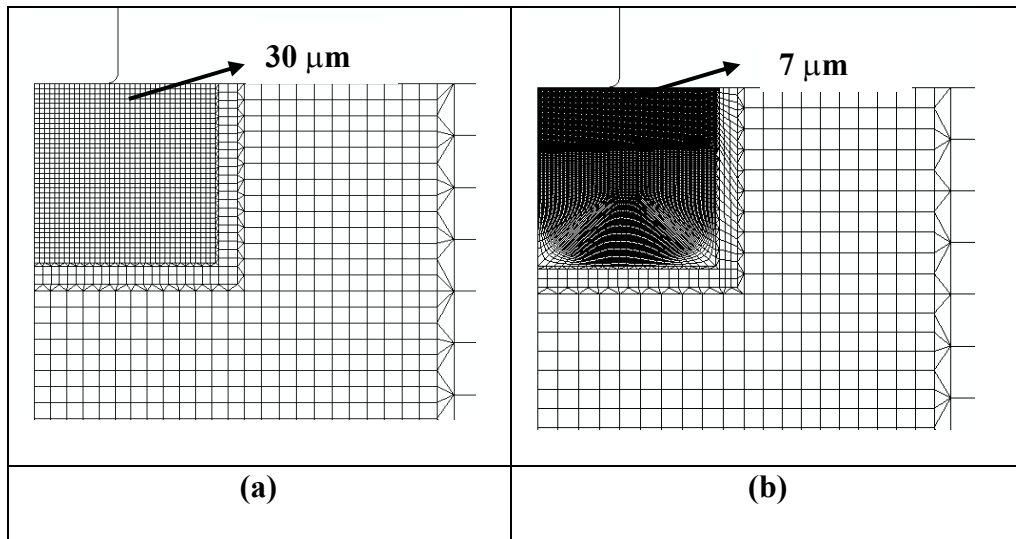


Fig. 6.3 The two different meshes with extreme mesh sizes, a) $30\text{ }\mu\text{m}$ and b) $7\text{ }\mu\text{m}$.

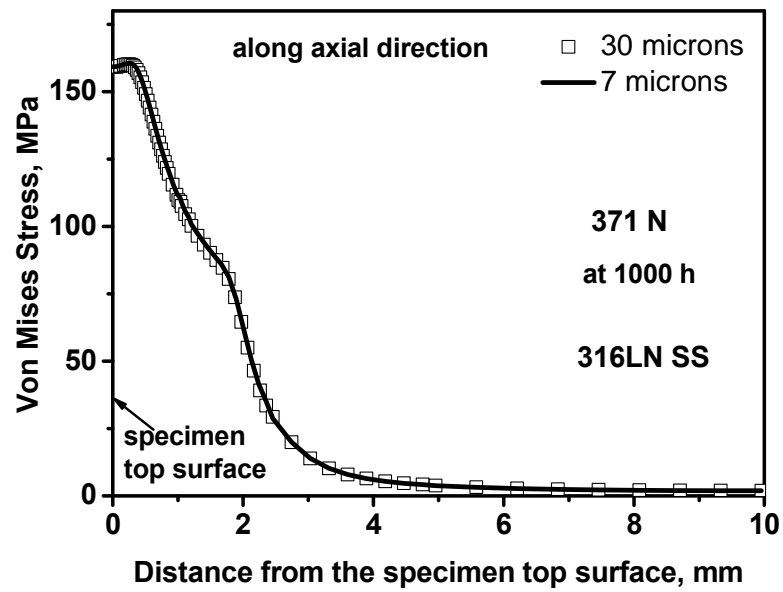


Fig. 6.4 The comparison of variation of the Von Mises stress along the axial direction for two different mesh sizes of 30 μm and 7 μm , tested for 316LN SS at a load of 371 N.

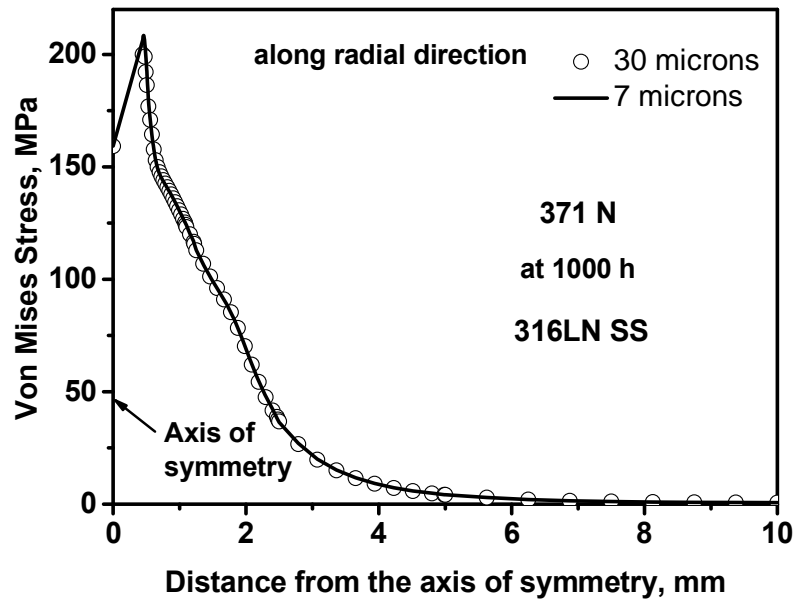


Fig. 6.5 The comparison of variation of the Von Mises stress along the radial direction for two different mesh sizes of 30 μm and 7 μm , tested for 316LN SS at load of 371 N.

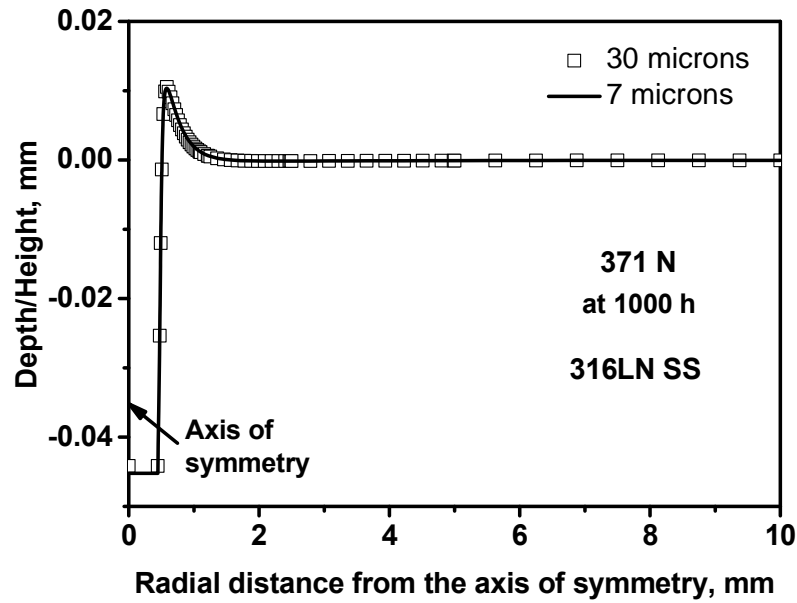


Fig. 6.6 The comparison of depth profiles for two different mesh sizes of 30 μm and 7 μm , tested for 316LN SS at load of 371 N.

6.3.2 Validation of the FE Model through Contact Stress Analysis

When two solid bodies are in contact, stresses arise at the interface between the contact. The type of contact stress or pressure distribution depends on the geometry of the contact surfaces. For an applied constant load, it is the contact stress distribution at their contact which governs the development of stress and deformation pattern in the specimen and hence study of contact stress distribution is of interest. In the case of contact between a flat specimen and indenter of different geometries, such as, sphere, cone, cylindrical flat punch, the contact pressure distribution is different for these different geometries of indenters [12]. For the cylindrical flat punch, the contact stress distribution beneath the punch is given by the relation [12],

$$\frac{\sigma_y}{P_m} = -\frac{1}{2} \left(1 - \frac{r^2}{a^2} \right)^{\frac{1}{2}} \quad \text{for } r \leq a \quad (6.5)$$

where, σ_y is the stress in the axial direction (y direction or loading direction), P_m is the mean contact pressure which is given by the indenter load divided by the contact area ($P_m = L/\pi a^2$), a is the radius of the indenter and r is the distance along the radial direction. The contact stress is minimum at the centre of the contact and reaches infinity at the edge. Outside the indenter ($r > a$), along the surface, $\sigma_y = 0$.

In order to validate of the finite element model and associated boundary conditions, the results for fully elastic case were analyzed and compared with the analytical solution for elastic stress field for cylindrical flat punch indentation (Eqn. 6.5). A typical normalized contact stress distribution for the cylindrical flat punch which is described by the Eqn. 6.5 can be seen in Fig 6.7 [12].

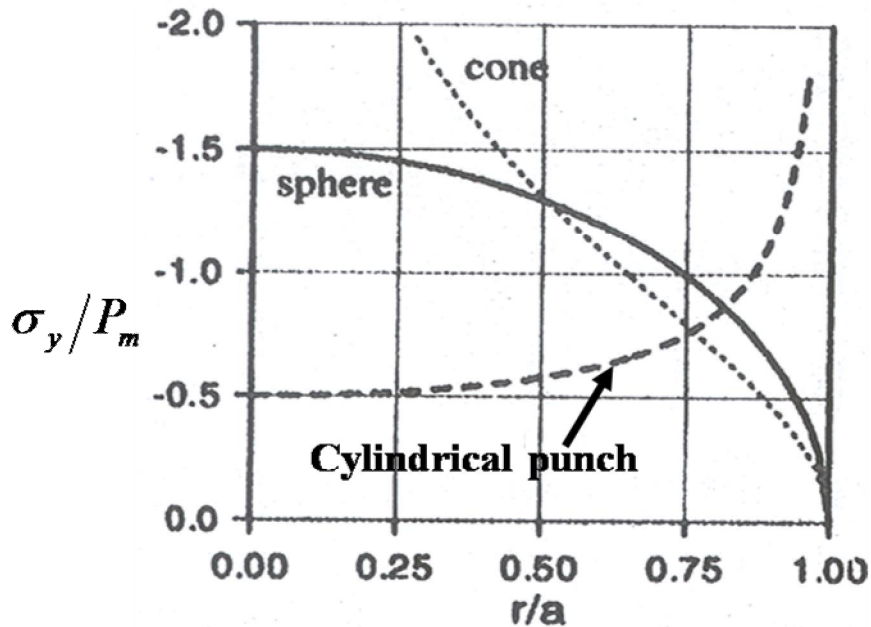


Fig.6.7 Normalized contact stress distribution σ_y/P_m for cylindrical flat punch after Fischer-Cripps [12].

In the present FE model, the contact stress distribution at the punch-specimen interface was analyzed. Figure 6.8 shows the normalized contact stress distribution σ_y/P_m in the specimen along the radial direction obtained from the FE model for the punch with 0.07 mm fillet radius and from the analytical solution (Eqn. 6.5) for the punch with no fillet (radius of the punch = 0.5 mm [12]).

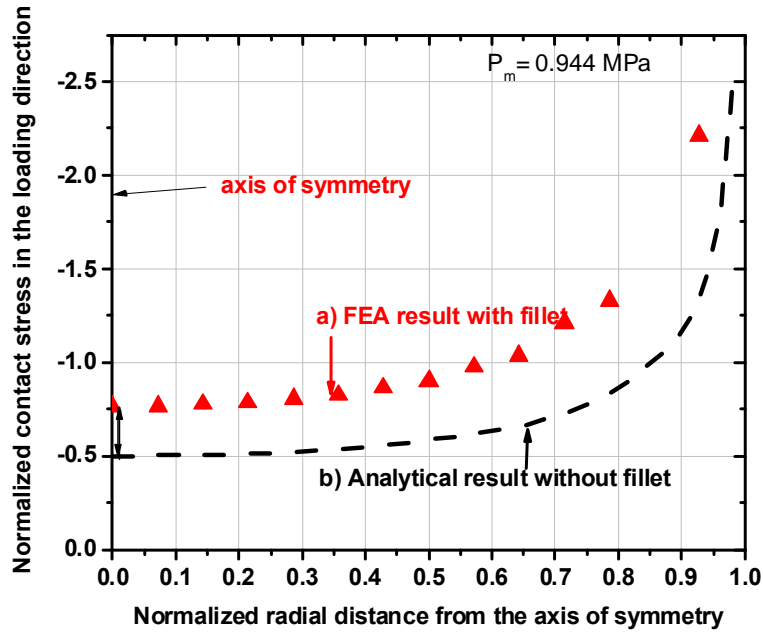


Fig.6.8 Normalized contact stress distribution σ_y/P_m for the cylindrical flat punch a) from the present FE model with fillet and b) from the analytical solution (Eqn. 6.5) which considered no fillet.

As can be seen from Fig. 6.8, there is a difference between the two curves. This is because, in the present model a fillet of radius 0.07 mm was introduced to the flat indenter and hence the actual contact radius is less than 0.5 mm. Therefore, to account for this, the actual contact radius was determined from the FE model and incorporated in the Eqn. 6.5 to calculate the contact stresses analytically. The analytical stresses calculated after incorporating the actual radius were compared with the stresses

computed from the FE analysis. Figure 6.9 shows the comparison of the contact stress distribution obtained from the FE model and the calculated analytical stresses using Eqn. 6.5. The stresses computed from FE model agree well with the analytical solution which proves the validity of the present FE model.

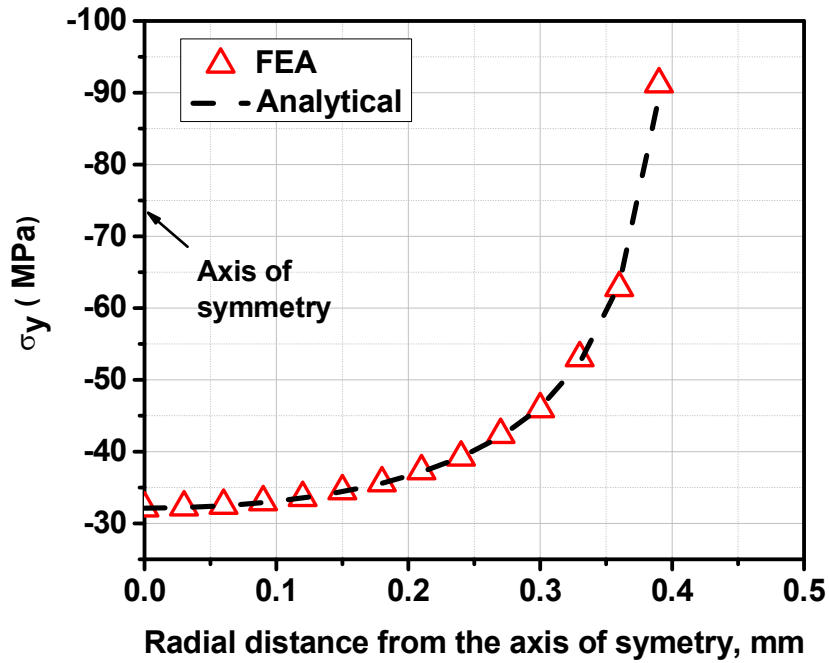


Fig.6.9 Comparison of FE results and the analytical results for the contact stress variation for the cylindrical punch. The Eqn 6.5 was used to calculate the analytical contact stresses.

6.3.3 Von Mises Stress Distribution in the Specimen beneath the Indentation

The Von Mises stress distribution in the specimen beneath the indenter was studied. The Von Mises stress is often used in determining whether a material will yield when it is subjected to complex loading conditions. This is accomplished by calculating the Von Mises stress and comparing it with the material's yield stress, which constitutes

the Von Mises yield criterion. If σ_1 , σ_2 and σ_3 are the principal stresses in three directions, the Von Mises stress can be expressed as,

$$\sigma_{Mises} = \frac{1}{\sqrt{2}} [(\sigma_1 - \sigma_2)^2 + (\sigma_2 - \sigma_3)^2 + (\sigma_3 - \sigma_1)^2]^{\frac{1}{2}} \quad (6.6)$$

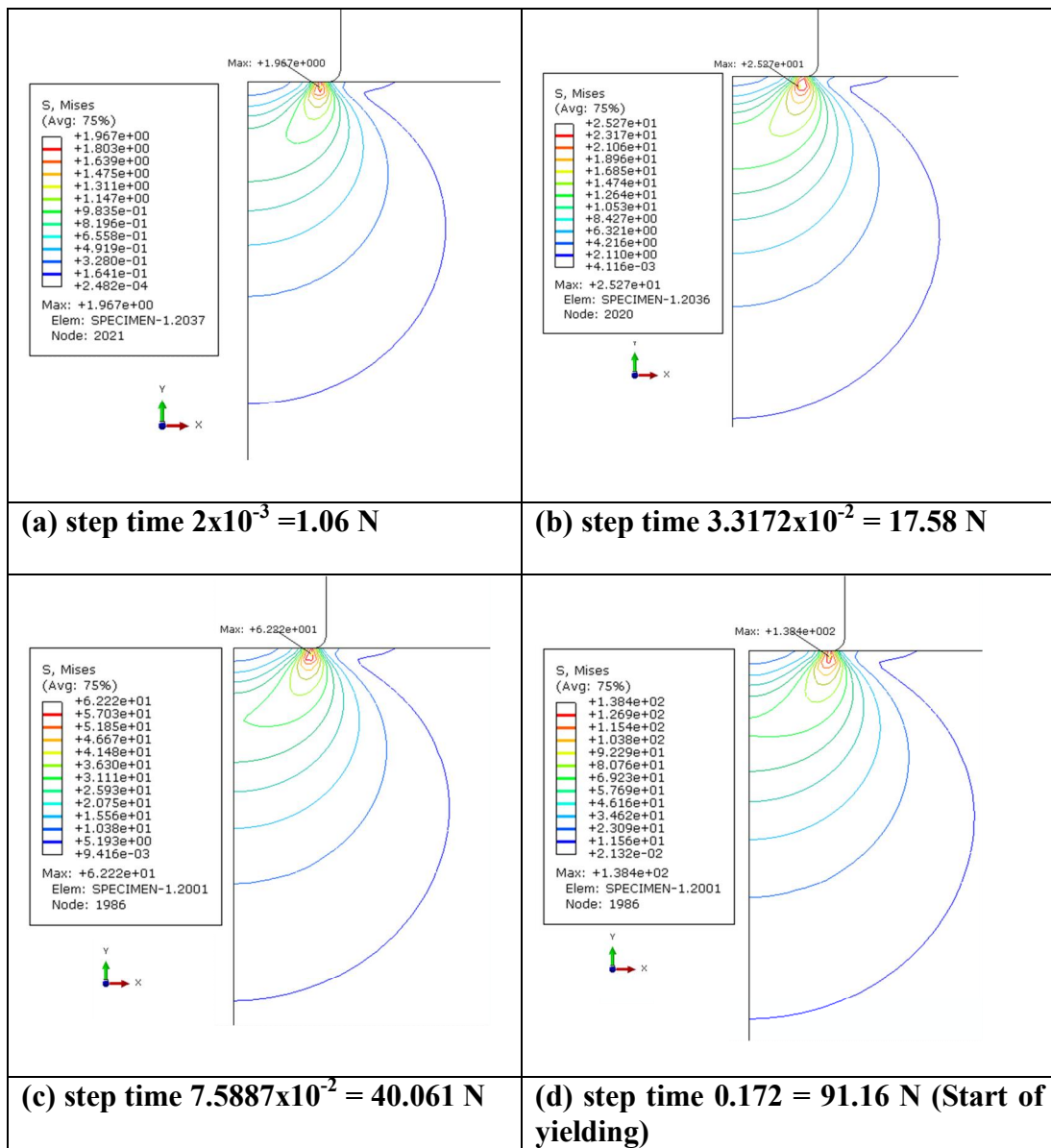
According to Von Mises yield criterion, the initiation of plastic deformation takes place when the von Mises stress developed becomes equal to the yield stress (σ_y) of the material. The material deforms plastically when the von Mises stress is greater than the yield stress of the material.

6.3.3.1 Evolution of the Von Mises Stress during Loading

Figures 6.10a-j illustrate the evolution of Von Mises stress within the specimen below the indenter during loading. The load was applied in increment steps with a step time equal to 1. The total load applied was 530 N. Graphical representation of the variation of Von Mises stress along the radial direction in the specimen with increasing load is given in Fig. 6.11.

After the application of initial load of 1.06 N, shown in Fig. 6.10a, it was observed that the maximum Von Mises stress was located at the edge of the indentation, even though the corner of the indenter is filleted. This maximum Von Mises stress increases with increasing load as can be seen from the Figs 6.10b-j. For the load of 91.16 N (Fig 6.10d), the Von Mises stress value at the edge of the indentation is 138.4 MPa which is close to the yield stress of the material (139 MPa). However, at this load, the Von Mises stress at the middle of the indentation was much less than the yield stress of the material (see Fig. 6.11). This indicates that the onset of plastic yielding of the specimen occurs at the edge of the indentation. With further increasing load, the plastically deformed zone spreads towards the middle of the indentation from the edge through a hemispherical zone (see Fig. 6.10e). This plastically deformed zone expands in both the

direction, towards the bottom of the punch and away from the punch, and evolving as a hemispherical zone surrounding the indentation as can be seen in Figs. 6.10 (f)-(j). The deformed zone under the indentation becomes fully plastic at a load equal to 311.5 N as can be seen from the Fig. 6.11. When the loading was completed (see Fig. 6.10j), the entire region in the vicinity of the indentation is fully plastic. In Fig 6.11, the initiation of yielding, development of fully plastic zone and the width of the plastic zone are indicated. The width of the plastic zone was found to be about 1.25 mm (Fig 6.11).



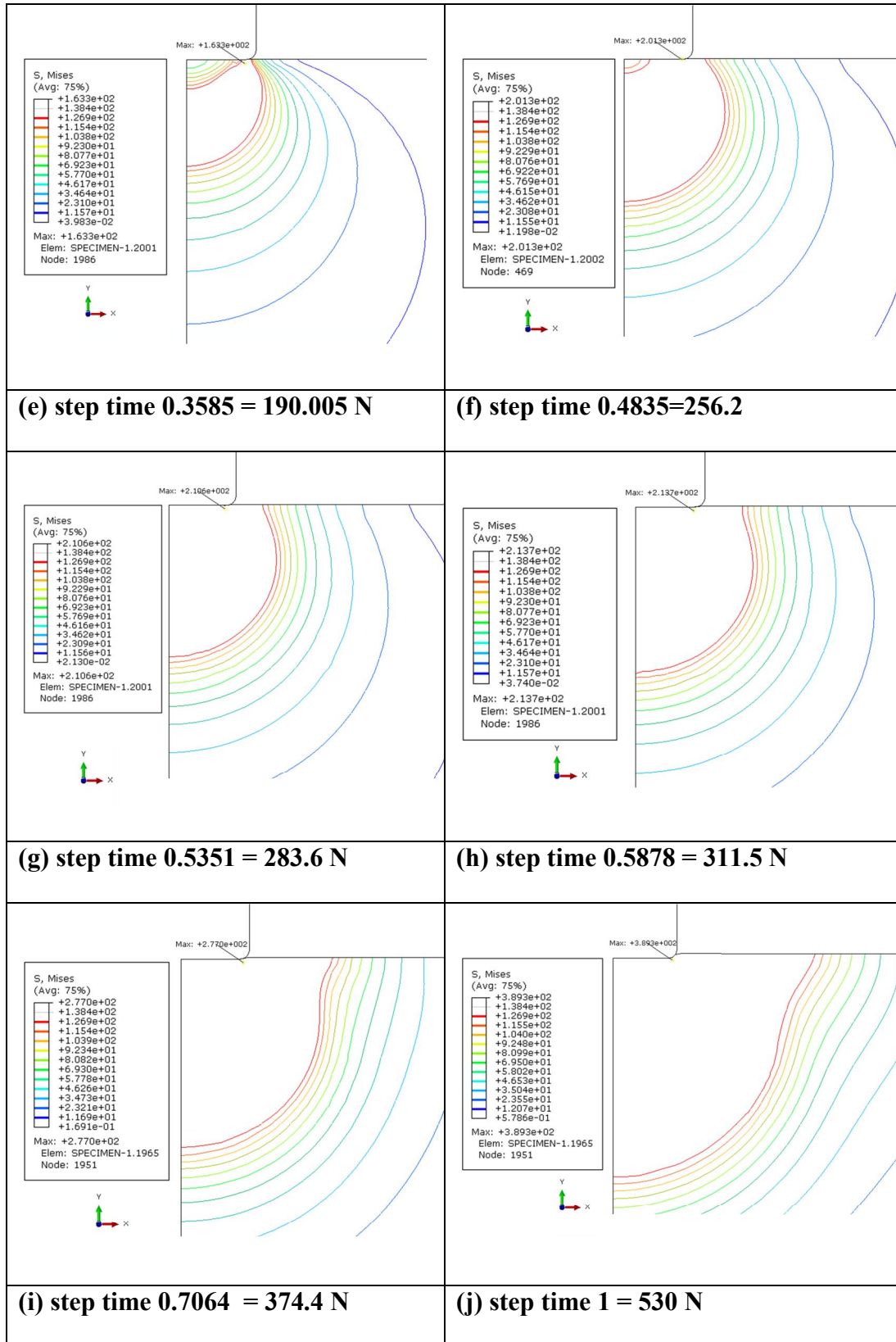


Fig. 6.10 (a)-(j) Contour plots of the Von Mises stress distribution in the specimen with time of loading. The total load applied was 530 N.

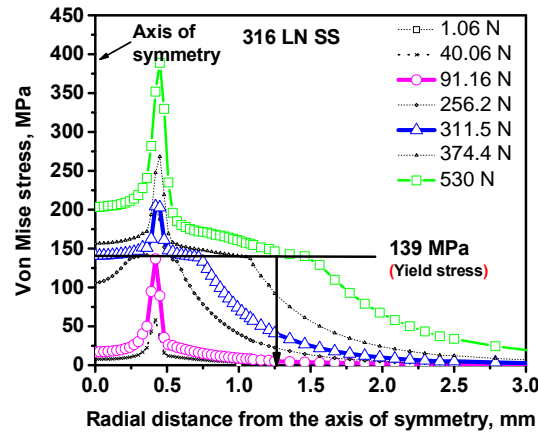


Fig. 6.11 Variation of the Von Mises stress along the radial direction with increasing load in the loading step.

At the load of 91.16 N, the contact radius was about 430 μm . The mean contact pressure P_m or the nominal stress at this load was estimated to be 156.9 MPa, which was about $1.12 \sigma_{yield}$, where σ_{yield} is the yield stress of the material. Thus, the onset of plastic deformation was found to commence at the circumference of the indentation at a nominal stress or mean contact pressure $P_m \approx 1.12 \sigma_{yield}$, although the rest of the material under the indentation deformed elastically at this stage. The region of plasticity at this stage was small and was only around the circumference of the indentation. As the load increased, the plastic zone grew and a permanent impression occurred with a fully developed region of plasticity around the whole indentation. The application of different yield criteria such as Haber-Mises, Tresca-Mohr for the onset of plastic deformation in the case of indentation by flat-ended cylindrical punch and spherical indenters were derived by several researchers [13, 14, 15]. It was found that in the case of flat-ended cylindrical punch and spherical indenters, the shear stresses at the sharp corner of cylindrical punch and the point of contact of spherical indenter increased and the plastic flow began at about $1.1 \sigma_{yield}$ [16, 17, 18]. This theoretically

predicted value was hence found to be in agreement with the value obtained from the present FE analysis. The reason for the high stress, i.e., $1.12 \sigma_{yield}$ at which yielding starts can be rationalized as follows. Impression creep test is essentially a compression test and the deformation is localized. When the plastic deformation begins at the circumference of the indentation, plastically deformed zone is confined within a large elastic region which offers a constraint to the plastic flow. Hence, the required stress to cause plastic deformation is higher than that in the case of uniaxial tensile creep test which generally does not experience any constraint for plastic flow.

6.3.3.2 Evolution of the Von Mises Stress during Creep

The evolution of Von Mises stress in the specimen during creep was analyzed for the above loading condition. The applied load (530 N) was held constant and the simulation was run for a sufficiently long time (up to 1000 h) in creep stage. Fig. 6.12 shows the Von Mises stress distribution in the specimen at the beginning of creep. The Von Mises stress at the edge and in the middle of the indentation was 389 MPa and 203 MPa respectively. The Von Mises stress at the edge of the indentation was found to be about 2.8 times the yield stress of the material (yield stress=139 MPa). Hence, on account of a high Von Mises stress at the edge of the indentation, the extent of plastic deformation was higher at the edge of the indentation than at the middle at beginning of creep. It should be noted here that it is this unique state of stress under the punch which governs the evolution of plastic zone with different microstructural changes in it as was observed in the previous chapters.

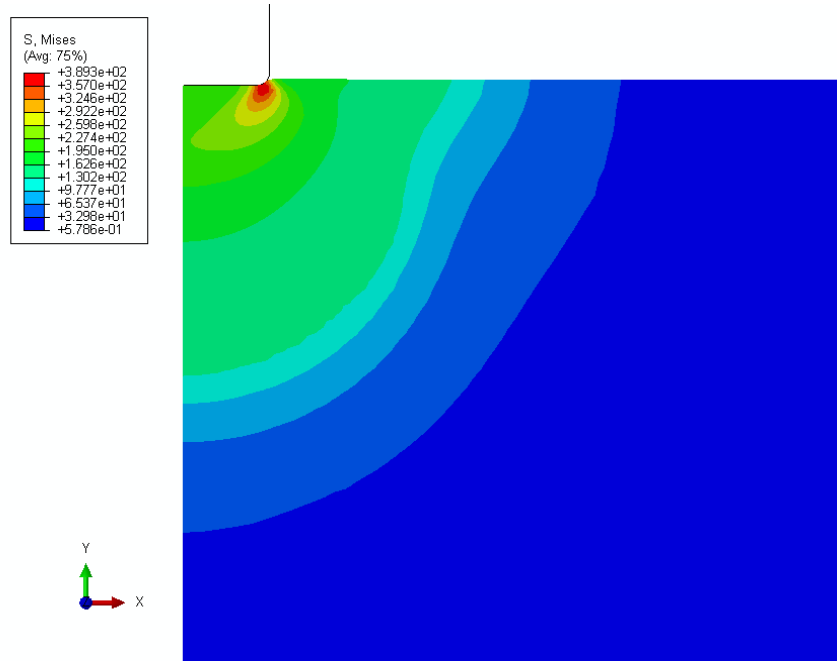
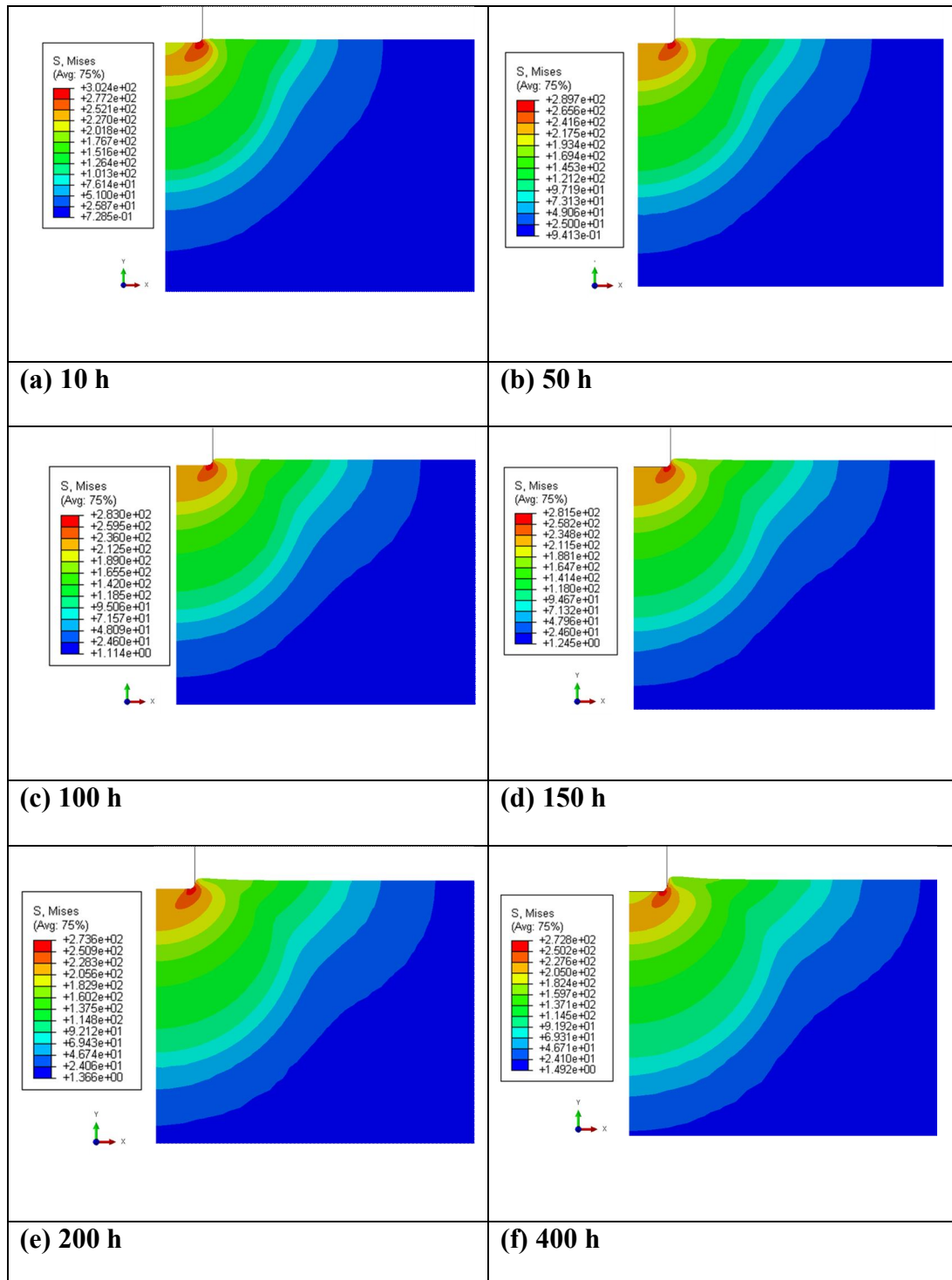


Fig.6.12 Von Mises stress distribution in the specimen after completion of loading;
Load= 530 N.

Figures 6.13a-h show the evolution Von Mises stress during creep. After 10 h of creep time, the Von Mises stress at the edge of indentation decreased from 389 MPa to 302 MPa. Subsequently, the Von Mises stress value at the indentation edge was further reduced to 289, 283, 281, 273, 272, 258 and 250 MPa after 50, 100, 150, 200, 400, 600 and 1000 h, respectively. Therefore, during creep, the stresses redistribute within the plastic zone under the punch. Similar observations of redistribution of stresses around the notch in creep specimens during creep exposure have been reported [19, 20, 21]. It was also observed that the size of the plastic zone remained roughly constant throughout the process which indicates the conservation of volume during plastic deformation. It is generally observed that during plastic deformation, in uniaxial test, volume is always conserved [22].



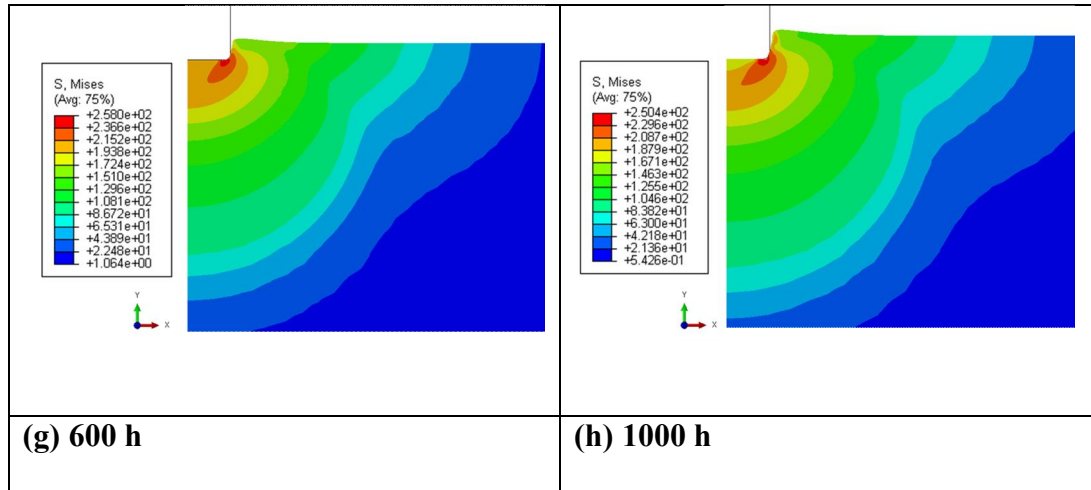


Fig. 6.13 (a)-(h) Contour plots of the Von Mises stress distribution in the specimen around indentation with increasing time of creep.

The variation of Von Mises stress along the axis of symmetry (axial direction) was analyzed during creep and is shown in Fig 6.14. The depth of the plastic zone was found to be about 1.25 mm. It was also found that the maximum Von Mises stress was found to occur at a distance below the punch approximately equal to the radius of the punch, consistent with the observation made by Chu and Li [23] from their finite element analysis on succinonitrile crystals. The occurrence of maximum deformation in a region which is located away from the indentation was also observed experimentally. To recall this, a microstructure of the deformed zone in this material tested at stress level of 675 MPa at 948 K, is shown in Fig. 6.15. The present FE analysis showed that the Von Mises stress in the region immediately under the punch was slightly above the yield stress of the material. But because of very high stress/strain concentration at the circumference of the indentation, the plastic deformation commences at the circumference of indentation, not near the middle of indentation. The Von Mises stress at the circumference of indentation was much higher than that acting in the region

immediately under the punch (near the middle of indentation) after completion of loading. As a result, plastic deformation occurs largely at the circumference of indentation and continues to spread from there through a hemispherically shaped zone (zone connecting the circumference) into the bulk of material, and thus few grains in the region immediately under the punch i.e., near the middle of indentation do not experience noticeable deformation/elongation (Fig. 6.15)[24].

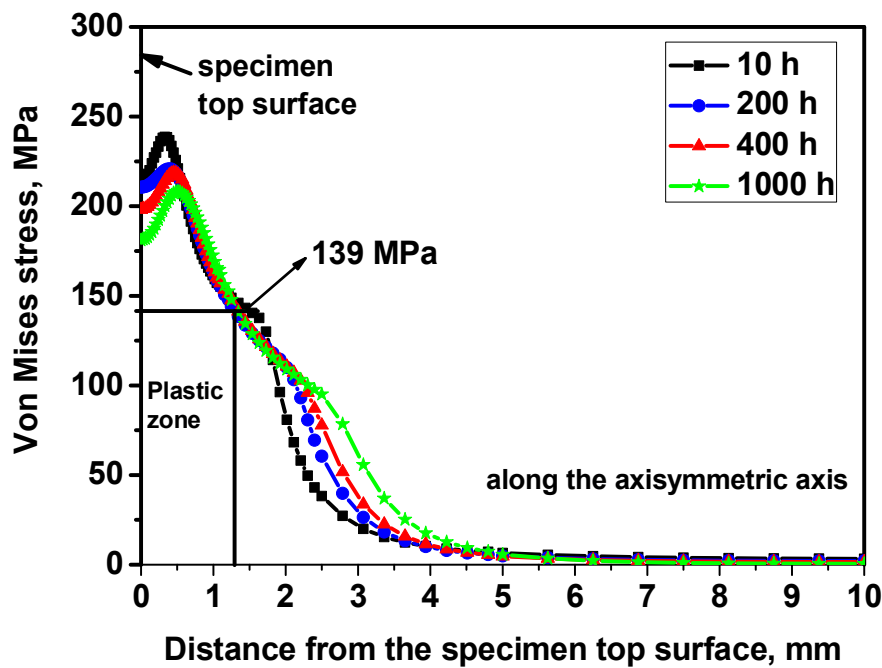


Fig. 6.14 Graphical representation of the evolution of the Von Mises stress within the specimen during creep deformation; the distribution is along the axis of symmetry.

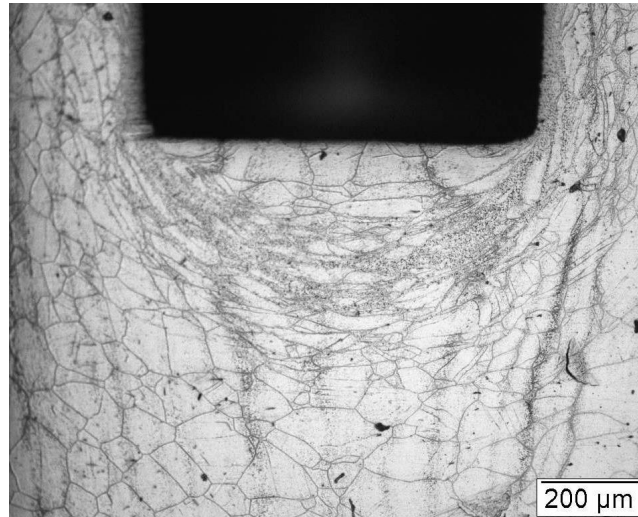


Fig. 6.15 Optical micrographs showing the deformation in the impression creep tested specimen in 316LN SS containing 0.14 wt. % nitrogen tested at 948 K, under the punching stress of 675 MPa.

6.3.4 Material Pile-up Mechanism in Impression Creep

As discussed in Chapter 4, in impression creep test, a prominent material pile-up on the specimen surface has been observed from the experimental investigation as shown in Fig. 6.16.

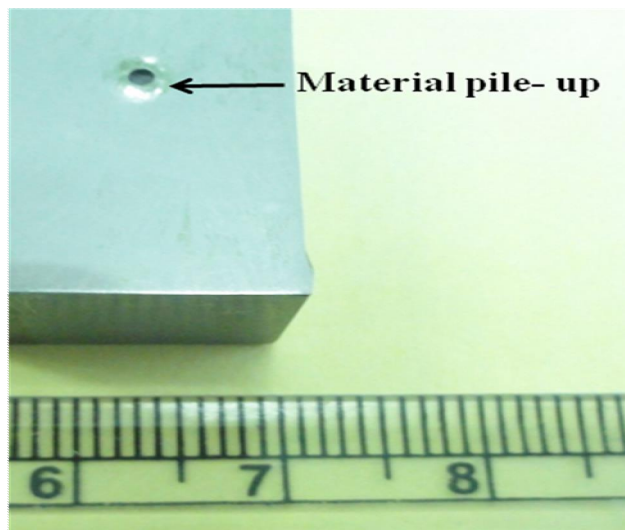


Fig.6.16 Typical indentation with material bulge/material pile-up around the indentation after impression creep test.

In order to understand the material displacement during indentation process and to gain insight into the understanding of material mechanics involved in the pile-up process, FE analysis on the pile-up behavior in 316LN SS have been carried out. Impression creep test was simulated at a constant load of 530 N. The displacements of the nodes in the specimen at different stages of loading and at different time of creep stages were analyzed.

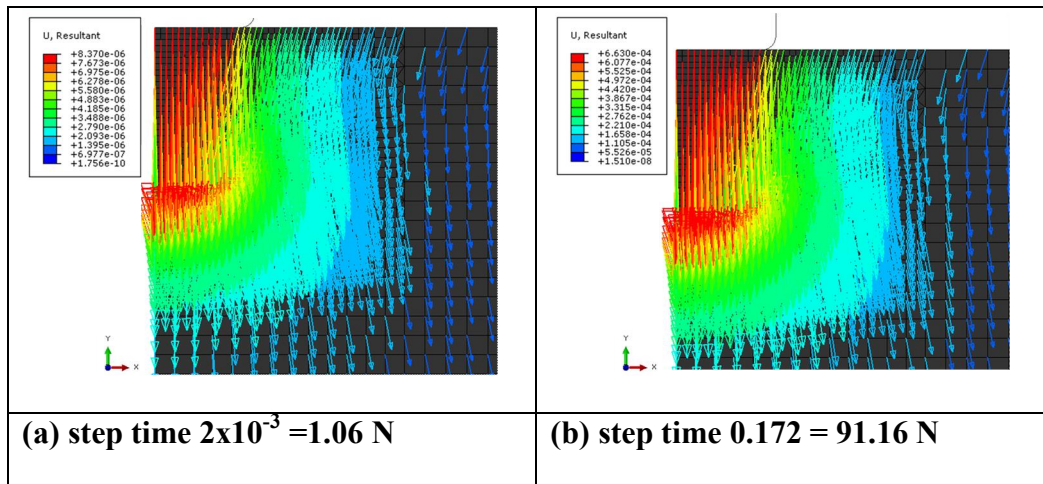
Figures 6.17a-h illustrate the displacement direction (resultant displacement) of nodes in the specimen in response to the indentation during loading. The load of 530 N was applied in the increment steps with a step time equal to 1, exactly in a similar manner which is described in the section 6.3.3.1. To explain the displacement behavior in the specimen more clearly, the deformed area under the punch is divided into two regions, namely, R1 and R2, as shown in the schematic diagram 6.18.

On application of the initial load, nodes in the specimen are displaced in the axial direction (y-axis) due to the compressive load as can be seen in Fig 6.17a. At this stage, there is no displacement of nodes in the direction opposite to the loading direction. Also, it can be observed that the nodes in R1 are displaced straight in the loading direction while nodes in R2, more so near the surface of the specimen are compressed towards the indenter. On increasing the load (91.16 N), the displacements continue to occur in the loading direction as shown in Fig. 6.17b. With further increasing load (see Fig. 6.17c-e), the direction of displacement in R2 deviates from the axial direction to radial direction which indicates that the materials displaced are pushed to the adjacent region R2. It should be noted that at this load the deformed zone under the punch is not fully plastic as discussed in the previous section. The region under the punch was found to become fully plastic after the application of load 311.5 N (see Fig. 6.11). Figure 6.17f shows the start of the displacement of the nodes in the direction opposite to the

direction of loading at which the region under the punch has become fully plastic (see Fig. 6.11). Hence, it can be concluded that the pile-up of material starts once the region under the punch becomes fully plastic. This observation is in agreement with the observation made by Pan and Dutta [25] from their finite element analysis in Sn-3.5Ag alloy which showed material pile-up on the sample surface after the plastic zone under the indenter was fully evolved.

This indicates that when the specimen is loaded the material in the vicinity of the indenter gets compressed in the loading direction and accommodated within the elastic-plastic zone in the specimen without material pile-up on the specimen surface. When the complete region surrounding the indentation becomes fully plastic, material starts flowing plastically. Since the plastic flow of material is confined in a large elastic/rigid volume of material, the flow is directed upwards and appears as pile-up on the surface of the specimen. Further increase of load causes more material to flow upwards as shown in Figs. 6.17g and 6.17h.

It is interesting to note that the material which caused pile-up are the material in region R2 which are pushed by the material under the punch in region R1. It should be noted that the size of the arrow and the arrow head indicates the magnitude of the displacement.



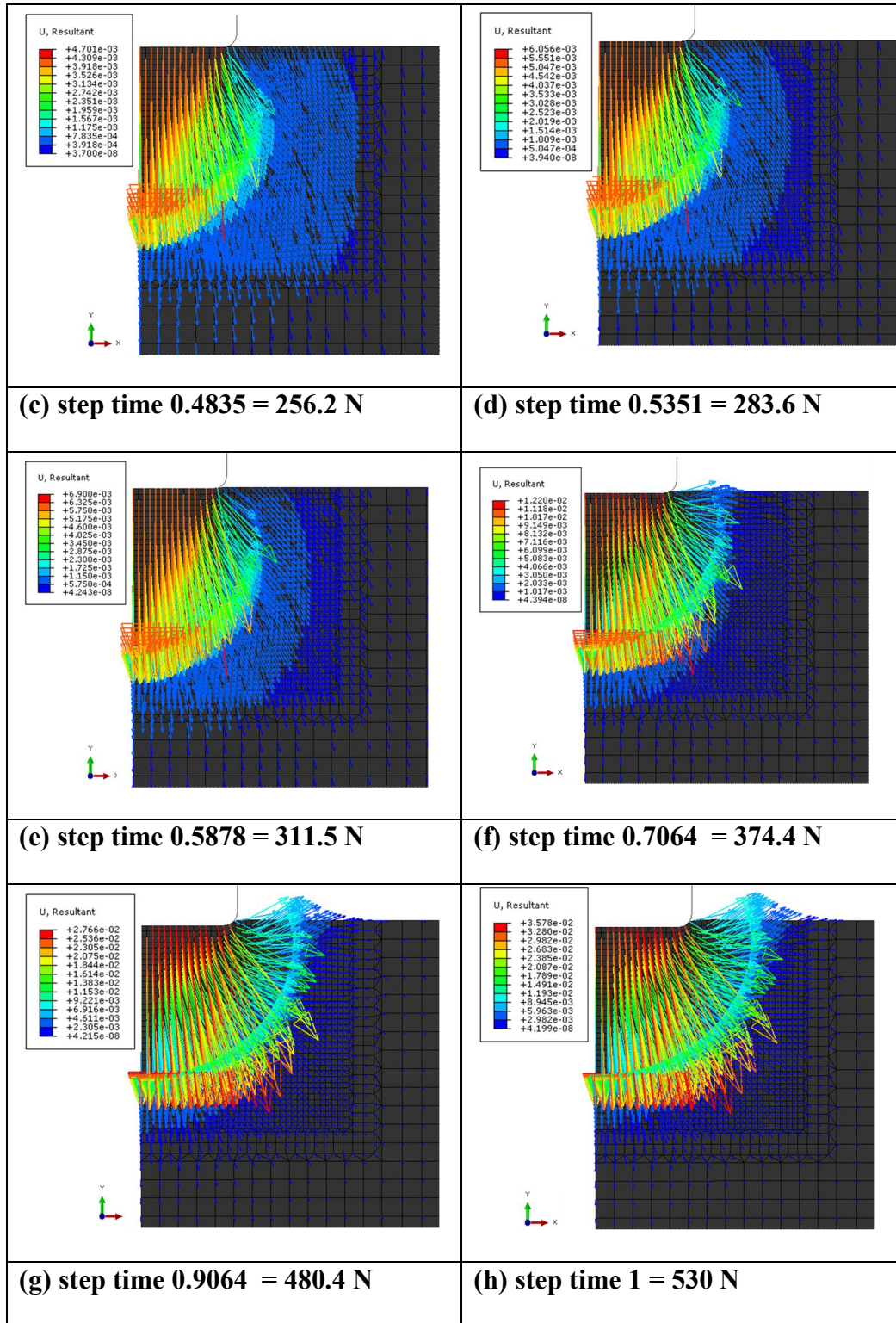


Fig. 6.17 (a)-(h) Symbol plots of resultant displacement of nodes during loading.

Figures illustrate how the material movement is directed during loading.

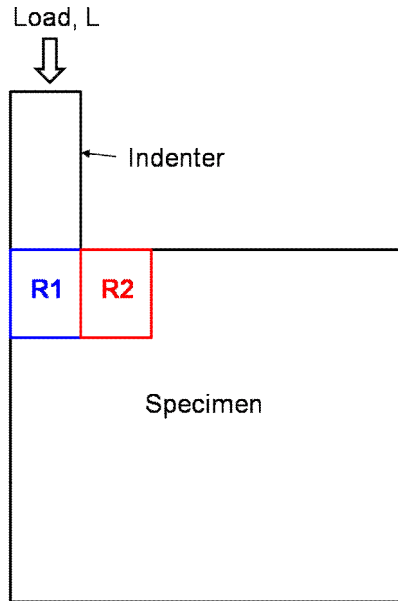
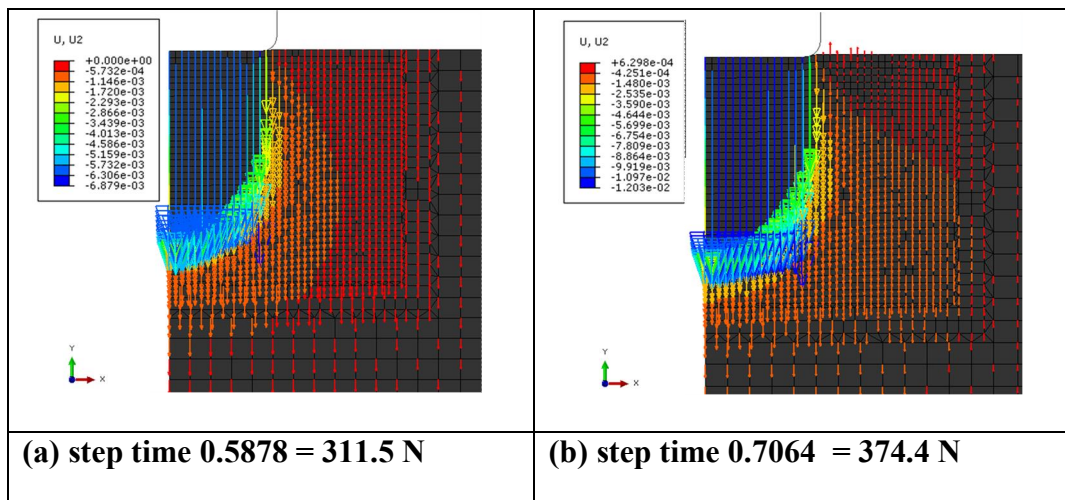


Fig. 6.18 Schematic showing the region R1 and R2 in the specimen.

Figure 6.19 shows the displacement of nodes in the axial direction. Figure 6.19 (a) corresponds to before pile-up which shows no displacement in upward direction even though there is a penetration of 7 μm . Figure 6.19 (b) corresponds to the start of the pile-up which shows a upward displacement of nodes of 0.6 μm . Figure 6.19 (c) corresponds to the end of the application of complete load which shows a pile-up of maximum 5 μm (displacement of one node).



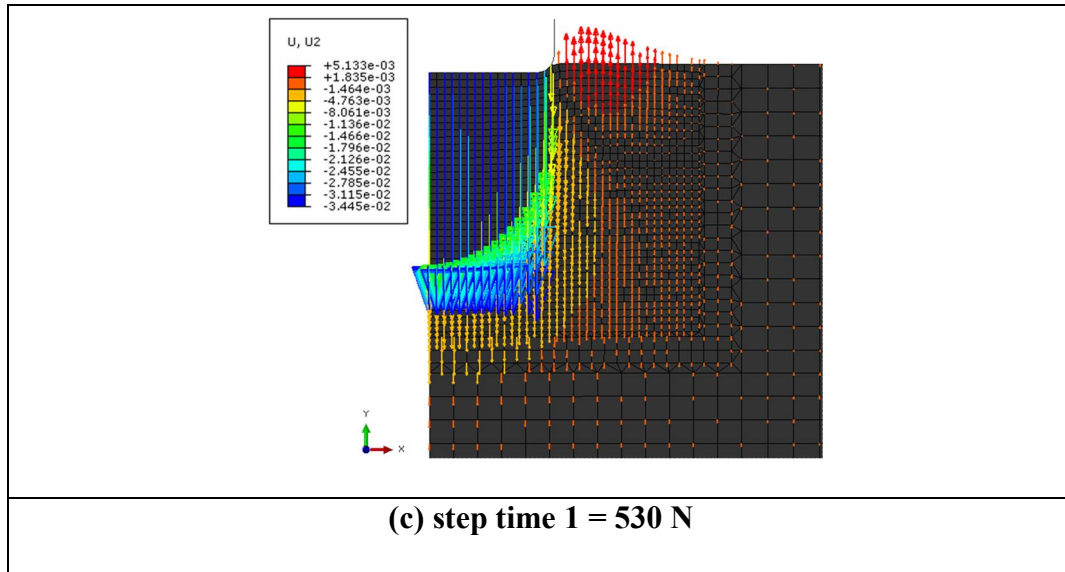
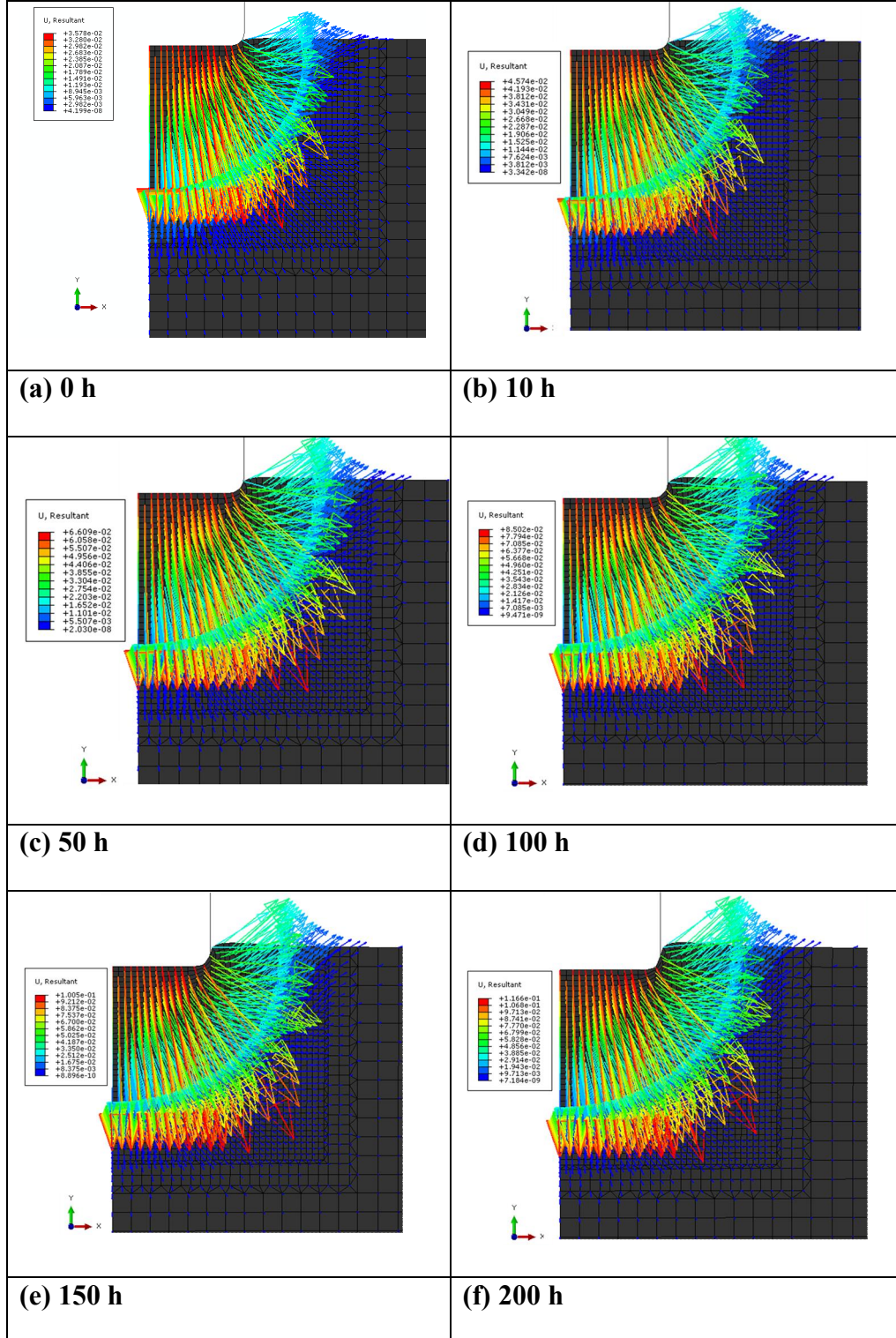
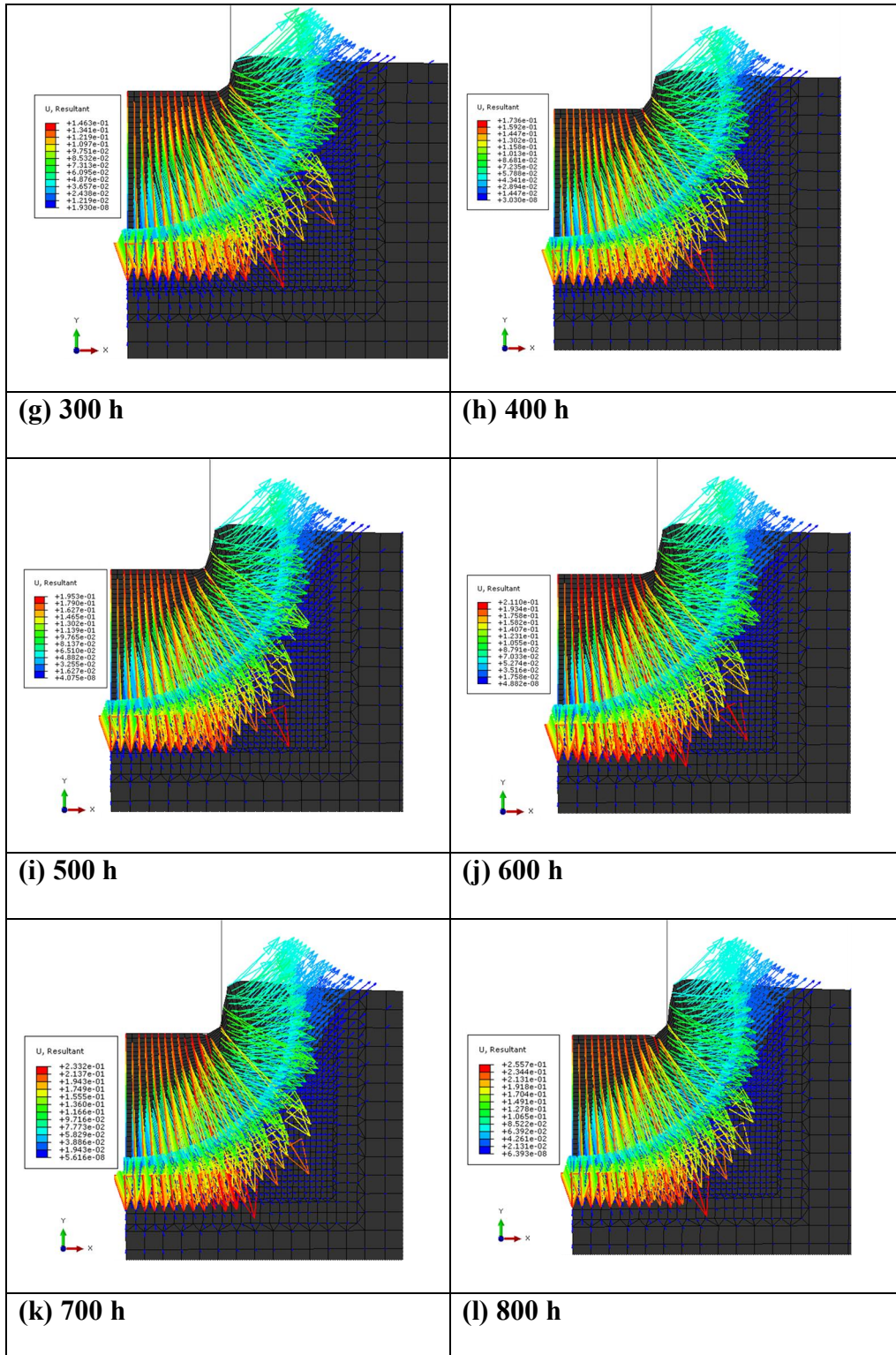


Fig. 6.19 (a)-(c) Symbol plots of displacement of nodes in the axial direction with loading. Figures illustrate start of the material displacement in the upward direction towards specimen surface.

After the application of the final load, during creep stage, the load was held constant and the creep analysis was run for sufficiently long time (up to 1000 h). The displacement of nodes in the specimen during creep was analyzed. Figures 6.20a-n are the symbol plots of displacement vectors (resultant displacement) at different time of creep from 0 to 1000 h. It can be observed that the direction of the resultant displacement of nodes continue to deviate from axial to radial direction. The displacement vectors adjacent to the indentation near the surface of the specimen (region R2, see Fig. 6.18) are directed upwards (almost positive y- direction). The pile-up height increases with increasing depth and time of creep. These observations indicate that as the indenter penetrates deeper into the specimen during creep, the material directly under the punch (region R1) experiences force in the loading direction and hence are displaced in the loading direction. But, material at distance slightly away from the indenter and at the corner of the indentation takes a curved path and pushes

the material adjacent to it in the outward direction. As a result, the material near the corner of the indenter and adjacent to it near the surface of the specimen (region R2) experiences upward flow and accumulates as pile-up on the surface of the specimen.





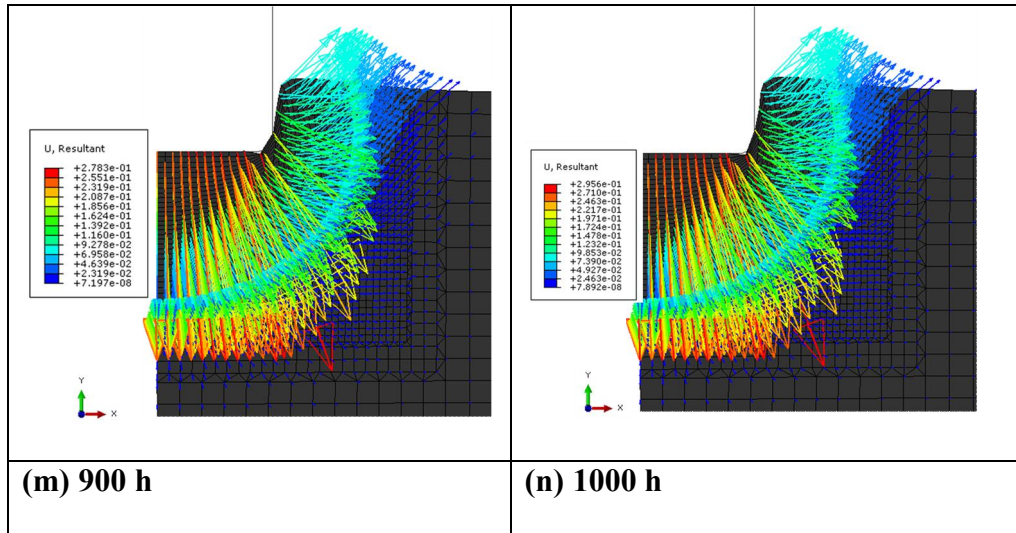


Fig. 6.20(a)-(n) Symbol plots of resultant displacement of nodes in the specimen in response to the indentation during different time of creep. The applied load was 530 N.

The evolution of the pile-up during creep deformation has been studied at different loads of 597, 530, 464 and 371 N, and is shown in Figs 6.21, 6.22, 6.23 and 6.24 respectively. The pile-up height was found to increase with increasing depth. The pile up height was also found to increase with increasing load.

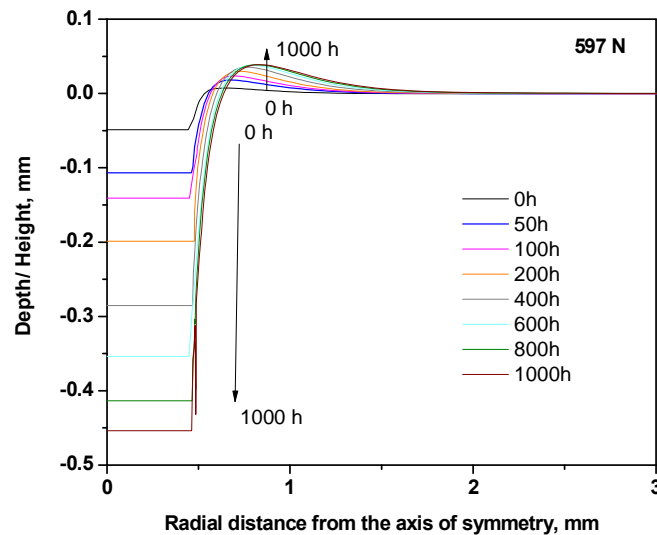


Fig. 6.21 The evolution of material pile-up on the surface of the specimen during creep at a load of 597 N.

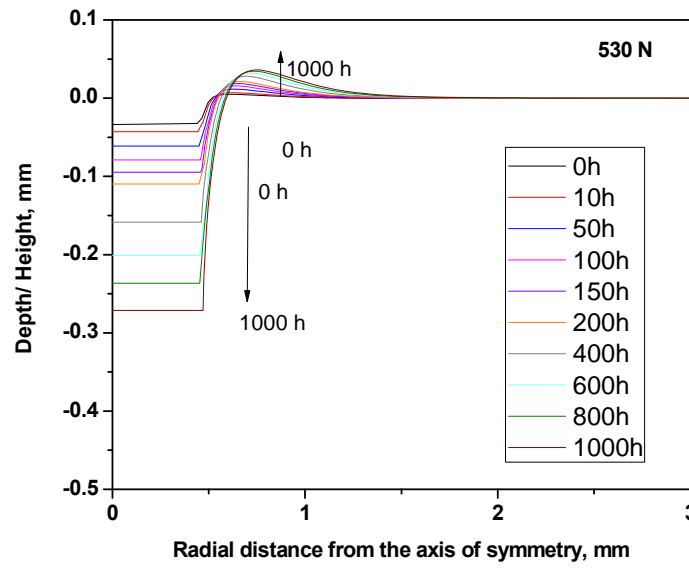


Fig. 6.22 The evolution of material pile-up on the surface of the specimen during creep at a load of 530 N.

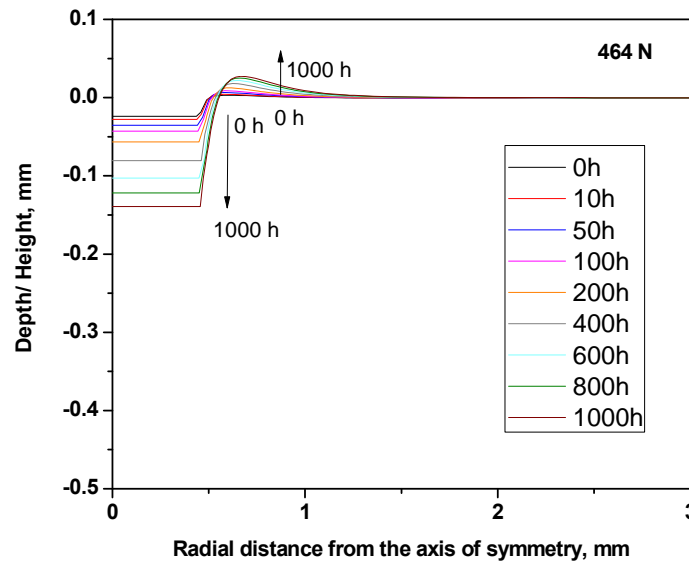


Fig. 6.23 The evolution of material pile-up on the surface of the specimen during creep at a load of 464 N.

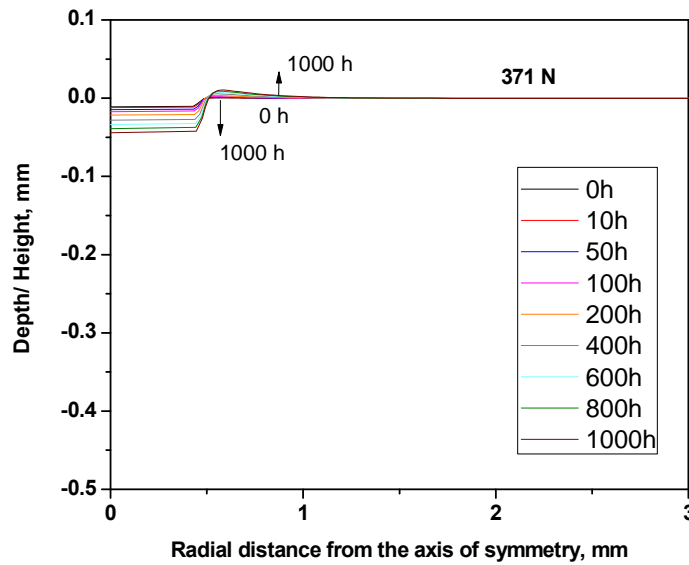


Fig. 6.24 The evolution of material pile-up on the surface of the specimen during creep at a load of 371 N.

It can be observed from Figs. 6.20, 6.21, 6.22, 6.23 and 6.24 that the material accumulated as pile-up on the specimen surface was less than that displaced below the indenter. This can be attributed to the high strain hardening exponent of 316LN stainless steel. The strain hardening exponent of materials strongly affects the extent of material pile-up. Researchers have found that the materials which exhibit high strain hardening exponent show less pile-up during indentation [26,24].

6.4 Conclusions

The main conclusions of this work can be summarized as follows.

- An axisymmetric finite element model of indenter-specimen system to understand the impression creep deformation has been developed using commercial ABAQUS finite element analysis software. FE simulation of

impression creep process has been carried out on 316LN SS under different loads.

- The stress analysis for fully elastic case in the present model agreed well with the analytical solution for elastic stress field for cylindrical flat punch indentation.
- The evolution of stress within the specimen under the punch at different stage of loading and subsequent creep deformation has been studied. The study revealed that the maximum Von Mises stress was located at the edge of the indentation, even though the corner of the indenter is filleted. However, introduction of the small fillet at the sharp corner of the indenter reduces the stress concentration at the edge of the indentation drastically and thus helps in achieving a converging solution.
- Plastic yielding of the specimen was found to commence at the circumference of the indentation at a nominal stress of about 1.12 times the yield stress of the material. The plastically deformed zone was found to spread out from the edge towards the middle of the indentation through a hemispherical zone.
- The size of the resulting plastic zone was approximately 1.25 mm. During creep exposure, the stresses redistribute within the plastic zone under the punch. The size of the plastic zone remained roughly constant during the creep deformation indicating the conservation of volume during plastic deformation.
- The Material pile-up mechanism in impression creep has been studied. It was found that the material pile-up starts when the deformed zone in the specimen under the indentation reached fully plastic.
- The evolution of pile-up studied at different load levels revealed that the pile-up height increases with increasing load and depth of penetration.

References

- [1] B. Storakers and Per-Lennart Larsson, *J. Mech. Phys. Solids.*, 42 (1994) 307-332.
- [2] J. L. Bucaille and E. Felder, *Philos. Mag.*, 82 (2012) 2003-2012.
- [3] Sneddon, *Int. J. Eng. Sci.*, 3 (1965) 47-57.
- [4] K. L Johnson. "Contact mechanics", Cambridge: Cambridge University Press; 1987.
- [5] D. A. Hills, D. Nowell and A. Sackfield, "Mechanics of elastic contacts", Oxford: Butterworth; 1993.
- [6] G. Feng, S. Qu, Y. Huang and W.D. Nix, *Acta Mater.*, 55 (2007) 2929-2938.
- [7] F. Yang, J.C.M. Li and C.W. Shih, *Mater. Sci. Eng. A.*, 201(1995) 50-57.
- [8] RCC-MR, 2007, Design and construction rules for mechanical components of nuclear installations, Section 2, Subsection Z.A3.3S.22.AFCEN, Paris.
- [9] V.Ganesan, M.D. Mathew and K. B. S. Rao, *Mater. Sci. Technol.*, 25 (2009) 614-618.
- [10] J. Ganesh Kumar, M. Chowdary, V. Ganesan, R.K. Paretkar, K. Bhanu Sankara Rao and M.D. Mathew, *Nucl. Eng. Design.*, 240 (2010) 1363-1370.
- [11] ABAQUS Inc., ABAQUS Theory Manual. Hibbitt, Karlson, and Sorensen, Inc., Pawtucket, USA.
- [12] A.C. Fischer-Cripps, *Introduction to Contact Mechanics* Springer, 2000.
- [13] R.T. Shield, *Proc. R. Soc.* 233 (1956) 267-287.
- [14] G. Eason, R.T. Shield and F. Angew, *Math. M. Phy.*, 11 (1960) 33-42.
- [15] J.W. Harding and L.N. Sneddon, *Proc. Cambridge Phil. Soc.*, 41 (1945) 16-26.
- [16] H.Y. Yu, M.A. Imam and B. B. Rath, *J. Mater. Sci.* 20 (1985) 636-642.
- [17] D. Tabor, *Proc. R. Soc. London. A.*, 192(1948)247-274.
- [18] Timoshenko, *Theory of Elasticity*. 1934, McGraw Hill, NewYork, p. 344.
- [19] D. R Hayhurst and J. T. Henderson. *Int. J. Mech. Sci.*, 19 (1977) 133-46.

- [20] G. Eggeler and C. Wiesner, *J. Strain Analysis*, 28 (1993) 13-22.
- [21] S. Goyal, K. Laha, C.R. Das, S. Panneerselvi and M.D. Mathew, *Int. J. Mech. Sci.*, 75(2013)233-243.
- [22] R.W.K. Honeycombe, "Plastic Deformation of Metals", Butter and Tanner Limited, Great Britain, 1984.
- [23] S. N. Chu and J. C. M. Li, *J. Mater. Sci.*, 12 (1977) 2200-2208.
- [24] Naveena, J. Ganesh Kumar and M.D. Mathew, *J. Mater. Eng. Perform.*, (2014) in print.
- [25] D. Pan and I. Dutta, *Mater. Sci. Eng. A* 379 (2004) 154-163.
- [26] G. Das, S. Ghosh, S. Ghosh and R.N. Ghosh, *Mater. Sci. Eng. A*, 408(2005)158-164.

CHAPTER 7

Summary and Future Directions

7.1 Summary of the Thesis

This dissertation has been concerned with the development and establishment of impression creep testing facility at Indira Gandhi Centre for Atomic Research, for assisting in the development of new materials for fast reactor applications. In view of this, a systematic study has been undertaken to investigate the impression creep behavior of creep resistant austenitic stainless steel which has not been studied so far. The work carried out in this thesis and the results are summarized in this chapter.

A unique impression creep testing facility has been established at Indira Gandhi Centre for Atomic Research. The technique has been validated using 316LN stainless steel. Impression creep experiments were carried out on 316LN SS under different stress levels in the range 472-760 MPa, at different temperatures in the range of 898-973 K, using specimens of dimension 20 mm x 20 mm x 10 mm, under vacuum of 10^{-6} mbar. Cylindrical indenters with flat-end, made of tungsten carbide, were used and the diameter of the indenter was 1 mm. Impression creep curves exhibited two characteristic creep stages, namely, a primary creep stage and a secondary creep stage. The tertiary stage that appears in conventional creep curves was absent.

Correlation between the impression creep parameters (σ_{imp} , $\dot{\epsilon}_{imp}$) and conventional uniaxial creep (σ_{uni} , $\dot{\epsilon}_{uni}$) parameters has been established based on the laws of mechanics for time dependent plasticity of materials. The correlation factors $\alpha=0.33$ (1/3) and $\beta=1$ to relate the creep data from impression and conventional

tensile creep tests were evaluated. The equivalent steady state creep rates calculated from steady state impression velocities were found to be in close agreement with the steady state creep rates obtained from conventional uniaxial creep tests.

Stress dependence of steady state impression velocity was investigated. The Norton power law relationship between the steady state impression velocity and the punching stress was found to be obeyed. The power law exponent n varied between 3.3 and 8.2 depending upon the nitrogen content in the heat, in agreement with the uniaxial creep test results.

The temperature dependence of steady state impression velocity was investigated and the Arrhenius-type rate equation was found to be obeyed between the steady state impression velocity and the test temperature. The apparent activation energy Q_c estimated was 504 kJmol⁻¹. This apparent activation energy value is in general agreement with the apparent activation energy value reported for 316 stainless steel obtained from the uniaxial creep tests. Based on the n and Q_c values, it is concluded that the rate controlling mechanism is dislocation creep.

The influence of nitrogen on the creep deformation behavior of 316LN SS was investigated at 923 K under different stress levels. Tests were conducted at 923 K on four different heats of 316LN SS containing 0.07, 0.11, 0.14 and 0.22 wt. % nitrogen, under different punching stress levels. The steady state impression velocity was found to decrease with increasing nitrogen content at all the punching stress levels. Impression creep testing technique was found to be sensitive to capture the variation in creep rate due to the small change in nitrogen content in the steel.

Impression creep technique was employed to characterize creep behavior of different microstructural zones of 316LN SS weld joint. The tests were carried out at 923 K on three distinct microstructural regions, namely, the weld metal, the heat-

affected zone and the base metal of a 316LN SS weld joint, at punching stress levels of 760 and 675 MPa. The three distinct microstructural zones of the weld joint showed difference in creep behavior. The weld metal exhibited higher steady state impression velocity which is indicative of higher creep rate and relatively lower creep strength. The heat-affected zone was found to have the lowest steady state impression velocity compared to the base metal and the weld metal. Differences in creep behavior of various zones could be attributed to the difference in the microstructure and morphology exhibited by the individual zone. The steady state creep rates obtained from impression creep tests were compared with the steady state creep rates obtained from uniaxial creep tests for the weld metal and base metal. A good correlation between impression and conventional uniaxial creep data for the weld metal and the base metal was established. Impression creep technique was proved to be uniquely suitable to characterize creep deformation behavior of narrow microstructural zones of weld joints.

A detailed analysis of the characteristics of plastic zone developed in impression creep tests was carried out using various experimental techniques. The microstructural evolution of the plastic zone, shape and size of the plastic zone, the extent of deformation, pile-up of the material on the specimen surface in the vicinity of the impression etc were studied by optical microscopy, scanning electron microscopy, EBSD analysis, TEM analysis, microhardness and surface profilometry. The microstructural analysis revealed that the maximum deformation in the vicinity of the impression occurs near the corner of the impression which extends into the bulk of specimen through a hemispherical zone. This zone was found to experience maximum shear deformation which was characterized by elongated grains. A small region immediately under the punch showed no significant grain shape change. The plastic

zones between two adjacent indentations were studied using microhardness and profilometry. The size of the plastic zone was about 1 mm. Hence, $\beta = 1$ (depth of the plastic zone), determined from the microstructure and microhardness measurements, can be used to convert the steady state impression velocity to an equivalent uniaxial steady state creep rate. Based on the analysis of the width of the pile-up on the surface of the specimen and the size of the plastic zone determined from the microhardness measurement, the minimum distance that should be maintained between the adjacent impressions was optimized to be at least 5 times the diameter of the indenter.

Finite Element Analysis of impression creep deformation was carried out to understand the elastic-plastic-creep deformation behavior of the specimen in response to the indentation process. An axisymmetric Finite Element Model of indenter-specimen system has been developed using ABAQUS finite element analysis software. Detailed analyses of the stress distribution under the punch and its variation during creep deformation were studied. The size and shape of the resulting plastic zone was analysed. The size of the plastic zone was found to be approximately 1.25 mm. The mechanics involved in the material flow in response to the indentation and mechanism of material pile-up on the specimen surface has been studied.

A good correspondence between the impression creep test and the conventional creep test results on engineering alloys demonstrated that impression creep could be used to characterize creep behavior of materials. It can be concluded that the impression creep technique is capable of yielding much of the information that can be obtained from conventional uniaxial creep testing and the technique is very attractive for alloy development programme where the material available for testing is small and a rapid screening of several heats are essential. Impression creep technique was

uniquely suitable for determining creep deformation characteristics of narrow microstructural zones in 316 SS weld joints.

7.2 Future Directions

Impression creep technique has been established for evaluation of creep properties of both base materials and narrow microstructural regions of weld joints. The experimental investigation and the finite element analysis of impression creep deformation gave insights into better understanding of the deformation mechanisms. The directions for further research in these areas are outlined below.

- The present work was restricted to the use of indenter of diameter 1 mm to facilitate comparison of the test results on different heats of materials over the range of stresses and temperatures. The effect of punch diameter on the steady state impression velocity for a constant stress and temperature can be evaluated.
- The effect of surface roughness of the specimen on the impression creep test results can be assessed in view of optimizing the surface finish of the specimen.
- In the study of the plastic zone under the punch using EBSD, it was observed that different regions under the punch experienced deformations to different extent. As another step in this line, studies can be further extended to analyze the deformation under the indentation along the surface perpendicular to the direction of loading. This study is relevant in view of understanding the plastic deformation.
- The analysis of plastic zone can be further extended to study creep damage evolution at different regions within the plastic zone. The Focused Ion Beam (FIB) technique can be employed to extract the specimens from these different regions.

- The present FE model is focused on understanding the material mechanics involved in impression creep. In this line, to extend the idea of plastic flow of material during indentation process, the correlation or the analogy with the slip-line field theory of the flat punch could be studied. The machine compliance of the system can be determined. The strain and strain rate results from experiments and FE simulation can be correlated. The effect of fillet radius and the effect of friction between the indenter and the specimen on the stress distribution can be studied.